KARLSRUHE INSTITUTE OF TECHNOLOGY

INSTITUTE FOR NUCLEAR WASTE DISPOSAL

The fate of Eu(III)/Cm(III) during the nucleation and growth of celestite ($SrSO_4$) and strontianite ($SrCO_3$)

Zur Erlangung des akademischen Grades eines

DOKTORS DER NATURWISSENSCHAFTEN

(Dr. rer. nat.)

Fakultät für Chemie und Biowissenschaften

Karlsruher Institut für Technologie (KIT)

genehmigte

DISSERTATION

von

Dipl.-Chem. Louis Geraldin TEMGOUA

aus

Bafou, KAMERUN

KIT-Dekan:	Prof. Dr. Willem Klopper
Hauptreferent:	Prof. Dr. Horst Geckeis
Korreferent:	Prof. Dr. Thorsten Schäfer
Tag der mündlichen Prüfung:	18. 12 2015

Karlsruhe 2015

Erklärung /Declaration of Originality

Hiermit versichere ich, dass ich die vorliegende Arbeit selbständig verfasst und keine anderen als die angegebenen Quellen und Hilfsmittel verwendet habe. Darüber hinaus versichere ich, dass alle Stellen der Arbeit, die wörtlich oder sinngemäß aus anderen Quellen übernommen wurden, als solche kenntlich gemacht sind und dass die Arbeit in gleicher oder ähnlicher Form noch keiner Prüfungsbehörde vorgelegt wurde.

Karlsruhe, den 02.11.2015

Ort, Datum Unterschrift

Acknowledgments

The present thesis was performed at the Institute for Nuclear Waste Disposal (INE) of the Karlsruhe Institute of Technology (KIT) under the supervision of Prof. Dr. Horst Geckeis. I would like to dearly thank him for giving me this opportunity to do my PhD in his institute.

I especially would also like to thank my direct supervisor, Prof. Dr. Thorsten Schäfer, head of the Geochemistry division at KIT-INE, for his constant support, help and engagement in this work. I am very grateful to him for the knowledge and experience that I have got during the weekly discussions and for the always positive and friendly attitude.

I greatly thank Dr. Frank Heberling and Dr. Thomas Rabung who kindly agreed to review this thesis. The support they provided during the evaluation of the experimental data and their hospitality are gratefully acknowledged.

I would also like to thank Stephanie Heck; Kerstin Bender; Stefanie Hilpp; Robert Götz; Tanya Kisely; Eva Soballa; Dr. Tadahiro Yokosawa; Dr. Nicolas Finck; Dr. Vanessa Montoya Garcia; Dr. Carmen Garcia-Perez and Dr. Wolfgang Hauser for the analytic support and the material supply in the laboratory.

I am very thankful to all my colleagues from INE for the friendly atmosphere during the work.

Finally, to the very special people in my life: my parents, my sisters and brothers, and my large family. *Thank you for everything.*

Abstract

The present PhD thesis addresses the (i) homogeneous and (ii) heterogeneous nucleation and growth of celestite ($SrSO_4$) and strontianite ($SrCO_3$) as well as (iii) the fate of trivalent curium and europium during sorption or incorporation in celestite or strontianite. Celestite and strontianite were chosen as model minerals to investigate the kinetics of formation of secondary phase minerals susceptible to affect long-term safety of deep geological repositories for high-level radioactive waste. The formation of secondary phase minerals at the interface between engineered (e.g. bentonite) and geological (e.g. clayrock) barriers can lead to a porosity clogging, thus allowing an accumulation of gases generated in the repository. For example, the accumulation of hydrogen, which is generated by anaerobic corrosion of the waste canisters, could cause an increase of the pressure beyond some limits, leading possibly to failure of barriers [1]. Model-based descriptions are often not able to accurately predict the formation of secondary phase minerals [2], and should be tested using the model minerals celestite and strontianite. The determined kinetic parameters for their nucleation and growth are important input data for the modelling of reactive transport.

In comparison with other secondary mineral phases with higher relevance for nuclear waste disposal (e.g. Calcium Silicate Hydrate (CSH) phases), the well-known crystallography of celestite and strontianite as well their occurrence in a single one modification make them more suitable as model minerals for kinetics studies. Celestite and strontianite are two isostructural minerals sharing the same metal cation (Sr^{2+}), and crystallizing both in the orthorhombic dipyramidal crystal system. Celestite has been reported to be a minor secondary phase in clay rocks [3]. The dissolution/precipitation of celestite strongly impacts the concentration of exchangeable sulfate ions in the pore water of certain clay formations (e.g. COx-argillite) [4]. A recent study on the effect of pore clogging on anion migration in compacted clay (Illite) could show that celestite secondary phase formation may even block the anion migration completely [5]. It was therefore of high importance to investigate the kinetics of celestite growth and subsequently, in a comparative study, the kinetics of strontianite growth in order to decouple the effect of the crystal structure on the fate of trivalent curium and europium from the effect of the anionic ligand.

The nucleation of celestite and strontianite was studied as a function of solution supersaturation ratio (S), temperature (T), ionic strength (I) and additives used as catalyst (glass beads) or inhibitor (dissolved silica). Laser induced breakdown detection (LIBD) was used for the determination of induction times (t_{Ind}), which could be determined directly by time resolved breakdown probability (BDP) measurements. Both the celestite and the strontianite undergo homogeneous nucleation at

supersaturation ratios of $S_{celestite} \geq 6.31$ and $S_{strontianite} \geq 12.59$, respectively. Above these supersaturations, induction times [min] are related to the solution supersaturation ratio by:

$$\ln t_{Ind}\,[min] = 0.49 + 16.92\,(\ln S)^{-2} \qquad \text{for celestite}$$

$$\ln t_{Ind}\,[min] = 0.56 + 32.05\,(\ln S)^{-2} \qquad \text{for strontianite}$$

From the above relationships, the interfacial tensions, γ, of the two mineral phases are derived. They are 22.6 ± 0.4 mJ·m^{-2} and 31.5 ± 0.5 mJ·m^{-2} for celestite and strontianite, respectively. At lower supersaturation ratios ($S_{celestite} \leq 6.31$; $S_{strontianite} \leq 12.59$), the nucleation seems to be heterogeneous, occurring preferentially on the surface of impurities (dust particles, vessel walls…) present in the solution. Induction times decrease with increasing supersaturation (e.g. from 1305 min at $S_{celestite}$ = 2.51 to 5 min at $S_{celestite}$ = 31.63), temperature (e.g. for $S_{celestite}$ = 10.72, t_{Ind} = 26 and 560 min at 317 and 279 K, respectively) ionic strength (e.g. at $S_{celestite}$ = 10, t_{ind} = 5 and 100 min for I = 1 mol·kg^{-1} NaCl and 10^{-3} mol·kg^{-1} NaCl, respectively) and in the presence of glass beads. At constant solute concentration, the induction time increases with increasing concentration of dissolved silica (e.g. at $S_{celestite}$ = 12.59, t_{Ind} = 25 and 1500 min for [Si] = 0 and 7.67 ppm, respectively). The critical saturation index (Ω_{crit}) is defined in this thesis as the maximum supersaturation established without a detectable nucleation within 48 hours; it was determined to be 0.3 and 0.8 for celestite and strontianite, respectively. Experiments using transmission electron microscopy (TEM) clearly show that the early stage nuclei (ESN) during the crystallization of celestite are well crystalline. ESN of strontianite seem to be unstable with respect to nucleation quenching (addition of 0.1 mol·l^{-1} NaCl into a solution containing ESN of strontianite). Therefore, the observation of the ESN of strontianite using TEM was not possible.

The growth kinetics of celestite and strontianite as a function of solution supersaturation, seed crystals specific surface area, temperature, and ionic strength were studied in mixed flow reactor (MFR) experiments in the presence of seed crystals of the growing mineral phase. The rate of crystal growth was found to depend linearly on the supersaturation at supersaturations S ≤ 50, and rates constants k_r of 1.27 ± 0.12·10^{-9} mol·m^{-2}·s^{-1} and 9.24 ± 0.75·10^{-8} mol·m^{-2}·s^{-1} were determined for strontianite and celestite, respectively.

At constant supersaturation ratio ($S_{celestite}$ = 8.91), the non-surface normalized rates of crystal growth were found to increase with increasing specific surface area (SSA) of the seed crystals (R_G = 1.31·10^{-8} mol·s^{-1} and 3.15·10^{-8} mol·s^{-1} for SSA = 0.13 m²·L and 2.87 m²·L, respectively). Keeping the solute concentration constant (5.25·10^{-3} mol·l^{-1}), an increase of temperature from 278 to 338 K was found

to cause an increase of growth rates by factor 3; similar observations were made with increasing the ionic strength of the solutions.

In order to assess the effect of ligand strength, symmetry, and coordination number on solid solution formation of trivalent actinides and lanthanides in carbonate and sulfate minerals [6], the sorption/incorporation of Cm^{3+} and Eu^{3+} into celestite or strontianite during homogeneous nucleation as well as during the growth in the presence of seed crystals was investigated. The complex formation of trivalent actinides and lanthanides with celestite and strontianite was determined by time resolved laser induced fluorescence spectroscopy (TRLFS). Cm^{3+} and Eu^{3+} are chosen as the representatives for trivalent actinides and trivalent lanthanides, respectively. Cm^{3+} was used at very low concentrations (0.85 - $53 \cdot 10^{-9}$ $mol \cdot l^{-1}$). Attempts to quantify the Cm(III) uptake into the mineral phases by ICP-MS revealed that the amount of Cm(III) remaining in the solution is less than 1 ppb; therefore experiments with Cm(III) were used for spectroscopic investigation in order to learn about the molecular processes. Eu^{3+} has lower fluorescence yields, and a higher concentration ($125 \cdot 10^{-9}$ $mol \cdot l^{-1}$ in MFR experiments) was required for TRLFS measurements. This high concentration allowed a quantification of the Eu(III) uptake into the mineral phase: 30 – 40 % Eu^{3+} uptake by celestite while the uptake by strontianite is almost 100 %.

Dedicated to

„My parents“

Maurice Kenfack and Jacqueline Kenfack

Zusammenfassung

Die vorliegende Dissertation befasst sich mit der homogenen und heterogenen Keimbildung, und mit dem Kristallwachstum von Coelestin und Strontianit. Weiterhin wurden Sorption und Einbau dreiwertigen Curiums und Europiums in Coelestin und Strontianit untersucht. Coelestin und Strontianit wurden als Modell Minerale für die Untersuchung der Bildungskinetik von sekundären Mineralphasen ausgewählt. In einem Endlager im Tonstein könnte die Bildung von sekundären Mineralphasen an der Tonstein/Beton Grenzfläche zum Verschluss von Poren führen. Führt diese Abdichtung zur Gasundurchlässigkeit, könnte der Aufbau eines hohen Wasserstoffüberdrucks im Nahfeld zum Problem werden (Wasserstoff entsteht durch die Korrosion der Kanister, in welchen hoch-radioaktiven Abfällen verpackt sind). Die modellmäßige Beschreibung von Sekundärphasenbildung stellt nach wie vor ein Problem dar und soll mit dem Modellsystem Coelestin/Strontianit getestet werden. Die in dieser Dissertation ermittelten kinetischen Parameter für die Keimbildung und das Kristallwachstum von Coelestin und Strontianit stehen als wichtige Eingangsdaten für die Reaktive-Transport-Modellierung zur Verfügung.

Aufgrund ihrer wohlbekannte Kristallstruktur sowie ihr Vorkommen in einer einzigen Modifikation sind Coelestin und Strontianit für kinetische Untersuchungen gut geeignet. Coelestin und Strontianit sind zwei isostrukturelle Minerale, die sich dasselbe Metallkation (Sr^{2+}) teilen. Sie kristallisieren im orthorhombisch-dipyramidalen Kristallsystem (Raumgruppe Pnma). Coelestin kommt in kleinen Mengen in Tongesteinen vor [3]. Die Konzentration an Sulfat-Ionen in Porenwässern bestimmter Tonformationen (z.B. Callovo-Oxfordian Tonformation (Malm)) hängt stark von der Strontiumkonzentration und somit von der Coelestinlöslichkeit ab [4]. Eine aktuelle Studie zeigt, dass die Bildung von sekundärem Coelestin zu einer Verstopfung der Porenräume in verdichtetem Ton (Illit) führen kann. In diesen Experimenten konnte eine teilweise oder totale Blockierung der Anionen-Migration beobachtet werden [5].

Die Keimbildung von Coelestin und Strontianit wurde als Funktion verschiedener Reaktionsvariablen untersucht, unter anderen: Übersättigungsgrad, Ionenstärke, Temperatur und Einfluss von Wachstumshemmern oder -beschleunigern (Kristallisationskeimen). Die Induktionszeiten wurden mit Hilfe der Laser induzierten Breakdown Detektion bestimmt. Sowohl Coelestin als auch Strontianit kristallisieren bei erhöhten Übersättigungen ($S_{Coelestin} \geq 6{,}3$; $S_{Strontianit} \geq 12{,}6$) durch homogene Keimbildung. Folgender Zusammenhang zwischen Induktionszeiten und Übersättigungsgrad konnte für die homogene Keimbildung hergeleitet werden:

$$\ln t_{Ind}\,[\text{min}] = 0{,}49 + 16{,}92\,(\ln S)^{-2} \qquad \text{für Coelestin}$$

$$\ln t_{Ind}\,[\text{min}] = 0{,}56 + 32{,}05\,(\ln S)^{-2} \qquad \text{für Strontianit}$$

Aus den obigen Gleichungen lassen sich die Grenzflächenspannungen, γ, zwischen den gebildeten Keimen und der Lösung berechnen. Diese sind 22,6 ± 0,4 $mJ \cdot m^{-2}$ für Coelestin und 31,5 ± 0,5 $mJ \cdot m^{-2}$ für Strontianit. Bei niedrigeren Übersättigungen ($S_{Coelestin} \leq 6{,}3$; $S_{Strontianit} \leq 12{,}6$) erfolgt die Keimbildung heterogen, auf der Oberfläche von Verunreinigungen oder an Gefäßwänden. Allgemein wird eine Abnahme der Induktionszeiten beobachtet, wenn Übersättigung, Temperatur oder Ionenstärke erhöht werden, oder wenn Glas Kügelchen als „Kristallisationskeime“ zu den Lösungen gegeben werden. Die Zugabe von gelöstem Silikat führte hingegen zu einer Verlängerung der Induktionszeiten. In dieser Arbeit ist der kritische Sättigungsindex (Ω_{crit}) definiert als die maximale Übersättigung, bei der nach 48 Stunden keine Keimbildung nachzuweisen war. Er betrug 0,3 für Coelestin und 0,8 für Strontianit.

„Early stage nuclei“ (ESN) sind jene Nanopartikeln, die sich in den übersättigten Lösungen bilden, lange bevor wirkliche Keimbildung, die anschließend Kristallwachstum nach sich zieht, auftritt. In LIBD Experimenten wurden ESN unmittelbar mit der Einstellung der Übersättigung beobachtet. Transmissionselektronenmikroskopie (TEM) Aufnahmen konnten zeigen, dass die ESN im Fall von Coelestin kristallin sind. Die ESN von Strontianit scheinen weniger stabil zu sein, denn sie lösten sich während der Präparation der TEM Proben wieder auf.

Der Einfluss von Übersättigungsgrad, spezifischer Oberfläche von Saatkristallen, Temperatur und Ionenstärke auf die Wachstumsrate von Coelestin und Strontianit wurde in Durchflussreaktor- (MFR) Experimenten untersucht. Für Lösungsübersättigungen $S \leq 50$ konnte ein linearer Zusammenhang zwischen Kristallwachstumsraten und Lösungsübersättigung festgestellt werden. Die zugehörige Ratenkonstante (k_r) beträgt $(1{,}27 \pm 0{,}12)\cdot 10^{-9}$ $mol \cdot m^{-2} \cdot s^{-1}$ für Strontianit und $(9{,}24 \pm 0{,}75)\cdot 10^{-8}$ $mol \cdot m^{-2} \cdot s^{-1}$ für Coelestin. Der Einfluss der spezifischen Oberfläche der Saatkristalle auf das Kristallwachstum wurde untersucht, indem die Lösungsübersättigung konstant gehalten wurde (S = 8.9) und die Menge an Saatkristallen nach und nach von $8.0\cdot 10^{-2}$ $m^2 \cdot L^{-1}$ auf $9.7\cdot 10^{-1}$ $m^2 \cdot L^{-1}$ erhöht wurde. Dabei wurde eine Zunahme der nicht oberflächen-normierten Wachstumsrate festgestellt. Bei konstanter Lösungskonzentration ($5{,}25\cdot 10^{-3}$ $mol \cdot l^{-1}$) bewirkte eine Temperaturerhöhung von 278 auf 338 K eine Zunahme der Wachstumsrate um das Dreifache. Ähnliche Ergebnisse wurden mit der Erhöhung der Ionenstärke erzielt.

Der Einbau von dreiwertigen Actinoiden und Lanthanoiden während der Keimbildung und dem Kristallwachstum von Coelestin und Strontianit wurde mittels zeitaufgelöster Laser

Fluoreszenzspektroskopie (TRLFS) charakterisiert. Cm(III) und Eu(III) wurden dabei stellvertretend für die Actinoiden und Lanthanoiden ausgewählt. Aufgrund der Ähnlichkeit der Kristallstrukturen sowie dem Metallkation von Coelestin und Strontianit konnte gezielt der Einfluss der anionischen Liganden auf den Einbau der dreiwertigen Spurenelemente untersucht werden. Die Quantifizierung der Eu(III)-Konzentration vor und nach dem MFR ergab dass etwa 30 bis 40 % Eu(III) in Coelestin eingebaut werden. In Strontianit betrug der Einbau annähernd 100 %.

Table of contents

1 Introduction

Many different concepts for the disposal of radioactive wastes have been proposed, among others the disposal into space, in the polar icecaps and on or beneath the seabed. The disposal into space can only be applied to small quantities due to the relatively high transport costs. The transport itself by rocket involves incalculable risks [1, 7]. Uncertainties related to the geophysical and geochemical properties of the polar icecaps, as well as the impact of the global climate change on their behavior are factors limiting their suitability for the disposal of radioactive waste [1, 7]. Disposal on the seabed has been investigated [8] and is now prohibited by international agreement [9]. The majority of effort in most countries is now focused on deep geological disposal [10]. In all concepts of nuclear waste disposal in deep geological formations of the continental earth's crust, the key parameter is to avoid the release of contaminants into the biosphere. Geological repositories for nuclear waste generally rely on a multi-barrier system consisting of an engineered barrier and of a natural geological barrier. The engineered barrier system represents the man-made, engineered materials placed within a repository. The geological barrier includes the repository host rock and its surrounding subsurface environment.

The search for suitable host rocks for deep geological repositories has concentrated on four principal rock types: crystalline basement rocks; extrusive volcanic rocks (e.g. lavas and pyroclastic); thick or diapiric evaporite (salt) deposits and clays rocks. Characteristics of each of these different rock types are briefly given in the paragraphs below.

Crystalline rocks are very hard but tend to be brittle concerning deformation; therefore, they usually show faults and factures. The critical feature of crystalline rocks is advective groundwater flow, and thus potential radionuclide transport concentrated in their fracture networks, with essentially no advection occurring in the intact matrix of the rock, which can act to retain radionuclides by the process of matrix diffusion depending on the matrix porosity. The detection and measurement of transport properties representative for a geological formation is difficult, and sufficient process understanding on the formation scale can only be obtained through the linkage of hydrogeological measurements and both geochemical and structural modelling studies [10, 11].

Extrusive volcanic rocks are formed by the cooling and solidification of volcanic lavas and ash deposits. In some cases, the ash deposition occurs at very high temperatures which lead to a sintering of the individual particles and to the development of a massive rock formation known as welded tuff. These rocks tend to have low matrix porosity and can have physical characteristics (e.g. bulk composition) similar to crystalline rocks, although their mineral grain size tends to be much smaller.

Geologically old volcanic rocks may be located below the surface under more recent sediments layers and form potentially suitable repository host rocks [10].

Evaporite deposits tend to be located in sedimentary basins, since they form when closed water bodies evaporate, leaving behind an accumulation of salts. Thick beds of evaporates may remain in horizontal formation, or they may become unstable in terms of density and plasticity, if covered by large thicknesses of denser sediments, rising upwards to form salt domes. Both bedded evaporates and salt domes appear to provide some of the most suitable environments for deep geological disposal due to the ductile behavior of salt perfectly encapsulating the radioactive waste. Additionally, the higher thermal conductivity of saline rocks in comparison to crystalline or argillaceous rocks, reduces the thermal load/temperature peak in the formation [10].

Clays are formed by the accumulation and sedimentation of suspended material in marine or freshwater environments. Especially marine depositional environments have a good lateral predictability, whereas terrestrial sediments are heterogeneous showing frequently sandstone intercalations and their horizontal and lateral predictability is critical. Thick layer clay dominated sequences are potentially suitable for deep geological disposal due to their low permeability, diffusion dominated transport processes. The presence of swelling clays allows self-sealing or healing of potential discontinuities. Stable isotopes and chloride pore water studies from clay formations (e.g. Opalinus clay) have clearly shown that vertical transport processes out of the formation were purely diffusion driven over the last approximately 10 Ma [12] and therefore transit time will be extremely long and contaminant release will be slow. Several countries are considering clay-rich geological formations for deep geological repositories, including Switzerland, Belgium, and France [10].

During the lifespan of a geological repository, the performance of the engineered barrier system will be affected by several processes, such as heat release due to radionuclide decay, gas release due to the corrosion of the canisters, chemical reactions, and to some extent, waste dissolution followed by diffusive transport of radionuclides. Chemical reactions and radionuclide migration only play a role in the presence of groundwater. As a consequence of these processes radionuclides may be released from the waste container, pass through the engineered barrier, and migrate through the host rock formation. On their way through the multi barrier system, radionuclides will interact with available mineral surfaces and could be re-immobilized. This can occur via several retention processes including sorption or co-precipitation/solid-solution formation with secondary phases [13]. Therefore, the suitability of the natural barrier system with respect to the retention of radionuclides during transport processes is of high importance in the concept of radioactive waste disposal.

In order to assess the radiological hazards arising from deep geological repositories, the chemical processes leading to the release and immobilization of radioisotope must be quantified. The interface between the waste matrix and intruding groundwater has a particular importance. Secondary mineral formation may be a significant process in controlling radionuclide release during spent fuel dissolution by water in case of a broken canister [13]. A key challenge in the safety assessment for geological repositories is associated with the long periods of time over which radioactive wastes disposed therein remain hazardous. Processes occurring within timescales of several thousands of years can only be assessed using natural analogue studies, or estimated using computational methods (CrunchFlow, PhreeqC, ComSol…). This assumes the availability of experimental data for deducing the kinetics of repository relevant phenomena based on that observed in the laboratory [14].

The present thesis is devoted to the determination of kinetics parameters for i) the nucleation and ii) growth of celestite ($SrSO_4$) and strontianite ($SrCO_3$) from supersaturated aqueous solution, and iii) the comparison of the two isostructural strontium minerals (celestite, strontianite), with the only difference being the nature of the anionic ligand, with regard to solid solution formation with trivalent actinides and lanthanides. Celestite and strontianite are not the most relevant secondary phase minerals, but they are suitable model minerals for the investigation of secondary phase minerals formation. In this thesis, the determined kinetic parameters were the induction time for the nucleation (chapter 4.1) of celestite and strontianite, and their growth rates during crystal growth (chapter 4.2) experiments, respectively. The reaction variables in this study were the solution supersaturation, temperature, ionic strength, nucleation catalysts and inhibitors. The determined kinetic parameters are foreseen to be implemented in a code for the modelling of reactive transport of radio-contaminants through the Callovo-Oxfordian (COx) argillite formation. In the following paragraphs, a short introduction to the use of clay minerals as host rock for nuclear waste repository will be given (chapter 1.1). Chapter 1.2 will be dedicated to the isostructural minerals celestite and strontianite, which can form secondary phase minerals in the pores of the clay rock formation and hence contribute to the clogging of porosities and hinder the diffusion of gases. A recent study on the effect of pore clogging on anion migration in compacted clay (Illite) could show that celestite secondary phase formation may even block the anion migration completely [5]. Chapter 1.3 gives a brief overview of the use of kinetic parameters in the modelling of reactive transport phenomena. Even though studies on clays minerals and modelling of reactive transport were not part of this thesis, a brief overview is given in the next sections in order to describe the interrelation of these topics (clay minerals, reactive transport modelling) with the aims of the present work[15].

1.1 Claystone as potential host rock for radioactive waste storage

Claystones exhibit some advantages with respect to radioactive waste disposal, namely their significant capacity for surface complexation and for ion exchange; both processes are considered to significantly retard the migration of dangerous components in consolidated porous clay systems. Several countries have focused their research for a high level radioactive waste repository on claystone formations. At present, many European clayrock formations have been characterized in very detail, among other the Boom Clay formation in Mol (Belgium), the Callovo-Oxfordian (COx) argillite formation in Bure (France), the Opalinus Clay in Mont Terri and the Benken borehole (Switzerland) [16]. Some basic properties of these clays are summarized in Table 1. In general, each rock type contains considerable proportions of clays [17]. However, these formations exhibit significant differences in other properties. The differences in their ages, their maximal temperatures experienced during burial history, their pore water composition and content, attest for the unique history of formation for each of them [18].

Table 1. Selected characteristic data of clayrock types considered as deep geological host rock formations for high level radioactive waste

Clayrock	age 10^6 y	depth m	$T_{(max)}$ K	pore water wt. %	Organic matter wt. %	Clay fraction wt. %
Boom clay	30 - 36	200	289	25	2 - 3	35 - 65
COx-argillite	155	500	313	7	~1	~40
Opalinus clay	180	500	358	7	~1.5	45 - 60

In the COx argillite, most of the connected pores are associated with clay minerals and have dimensions in the range of 2 - 50 nm [19]. The mineralogy of the argillites can be subdivided into three groups of minerals: the *tectosilicate group* composed mainly of quartz and some feldspar, the *carbonate group* composed mainly of calcite and some dolomite, and the *phyllosilicate group* composed of mixed layers of illite-smectite and of non-swelling minerals such as kaolinite, mica and chlorite. Smectite has the highest specific surface area among all these minerals and therefore, the chemical reactions controlling the exchange of ions will be principally those involving this mineral [20]. Clay stones contain water in several forms. The water may be held in pores or adsorbed on the surface of the clay mineral structure. The aqueous solution that fills the pore spaces of solid particles within sediments of a water body will be referred to in this thesis as “pore water”. A selection of water composition obtained from a range of different clay-rocks and clay sediments is presented in

Table 2. Looking at the composition of the pore water in different clay formations suggests that mineral dissolution and growth will play an important role for natural trace metal partitioning [21], which in turn can influence the retention of radioisotopes.

Table 2. Examples of composition of water extracted from clay-rocks and clay sediments [22]

Clay formation	Opalinus clay	COx clay	Boom clay
In situ temperature K	286	298	289
pH at 293 K	7.7	7.4	8.4
[Na][1]	235	45.7	7.1
[K][1]	1.4	0.6	0.11
[Ca][1]	16.8	5.05	0.11
[Mg][1]	22.2	4.3	0.03
[Sr][1]	0.5	0.2	-
[Cl][1]	276	35.0	0.56
[S(6)][1]	17.4	12.5	0.44
[C(4)][1]	-	4.2	5.79
Alkalinity[2]	1.8	3.5	5.79
Ionic strength[3] (calc.)	0.37	0.09	0.01

The exchange reaction of SO_4^{2-} ions of celestite with CO_3^{2-} has been the subject of many investigations over the last century [23, 24]. In the COx-argillite, celestite is observed throughout all the clay formation as disseminated microcrystalline grains up to centimeter-sized euhedral crystals infilling late vugs. The strontium content in the COx-argillite varies between 222 and 470 ppm [25, 26]. Aqueous solution containing celestite particles in contact with the atmosphere can transform to strontianite ($SrCO_3$), because carbon dioxide can dissolve in aqueous solutions to form carbonate ions (CO_3^{2-}) which then react with the strontium in the crystal lattice. Therefore, when celestite is present in a geological formation, one should always keep in mind the probability of the occurrence of strontianite. The choice of celestite and strontianite as model minerals for the formation of secondary phase minerals in this thesis was motivated on the one hand side by their isostructurallity to barite and aragonite, which are much more abundant in geological host rocks relevant for nuclear

[1] concentration 10^{-3} mol·l^{-1}
[2] mM equivalent HCO_3^- per litre
[3] mol·kg^{-1}

waste disposal and on the other hand side by their fast growth kinetics. Chapter 1.2 will give a brief insight into their mineralogy.

1.2 Secondary phases formation: the model minerals celestite and strontianite

The composition of the mobile, bulk pore water in geological formations is an important factor to be taken into account in the safety assessment of nuclear waste repositories. Knowledge of the porosities accessible to the different contaminants is a prerequisite for the development of transport models. The chemistry of the pore water determines (a) dissolved and sorbed radionuclides speciation and, therefore, radionuclides mobility, and (b) the reactions that will take place with the material used in the engineered barrier and influence their evolution over time [4]. In groundwater for example, carbonate concentrations of up to 10^{-2} mol·l^{-1} can be found due to the increased CO_2 partial pressure, which is higher compared to the atmospheric partial pressure and is a function of the formation depth; these relatively high carbonate concentrations impact the geochemical milieu, the radionuclide speciation and the formation of secondary carbonate minerals. The pore water composition is controlled by the primary minerals in the altered zones of the early stages of weathering; therefore several secondary phases are generally formed. Mineral dissolution could increase rock permeability and promote gases diffusion, or the formation of secondary mineral phases could block flow paths and have the opposite effect. The formation of secondary phases will also have an impact on the nature of the surfaces the radionuclides interact with, e.g. any increased sorption capacity of secondary phases could retard contaminants migration. Main secondary phase minerals forming from the interaction of cement pore fluids with bentonite are calcium silicate hydrates, carbonates, some sheet silicates and polymorphs of silica [27]. During high pH rock alteration, the release of carbonate into solution can be observed [3]. For example, the breakdown of dolomite ($CaMg(CO_3)_2$) can be promoted by cement pore water. Celestite has been reported to be a minor secondary phase in clay rocks, occurring in trace amounts as euhedral, tabular, lath shaped crystals, 50-100 microns in size, with pitted surfaces [3]. The concentration of exchangeable sulfate ions in the COx-argillite is considerably impacted by the dissolution/growth of celestite [4].

The element strontium was first detected in the mineral strontianite found in lead mine at Strontian. Strontian is a village in Sunart, an area located in the council of Highland in Scotland. In 1790, referring to the observation that the Strontian ores exhibited different properties to those normally seen with other “heavy spars”, the physician Adam Crawford concluded that Strontian is a new species of earth which has not hitherto been sufficiently examined [28]. The new mineral was named strontites in 1793 by Thomas Charles Hope [29, 30]. The element was eventually isolated in 1808 by Sir Humpry Davy by the electrolysis of a mixture containing strontium chloride and mercury oxide. In

keeping with the naming of the other alkaline earths, he changed the name to strontium [31-33]. Strontium is a silvery white metal and the 15th most abundant element on earth, estimated to average 360 ppm in the earth crust. Strontium has at least 16 artificial radioactive isotopes [25]. Strontium occurs in nature as celestite ($SrSO_4$) and strontianite ($SrCO_3$), the former being the more abundant and the main source of strontium. Although there are some applications for celestite in its natural form, a large proportion of the world production is dedicated to the production of strontium chemicals, in particular the carbonate, nitrate and hydroxide of strontium. The most important of these chemical, the carbonate, was formerly used in the fabrication of cathode ray tubes for color monitors. Currently, strontium carbonate are being used in pyrotechnics as color-producing components (strontium produces a crimson red flame) [34].

Table 3. Crystallographic data of celestite and strontianite[4] [35]

		celestite	strontianite
Chemical formula		$SrSO_4$	$SrCO_3$
Space group		Pbnm	Pbnm
Cell parameters	a	8.359	8.414
	b	5.352	5.107
	c	6.866	6.029
Crystal system		orthorhombic dipyramidal	orthorhombic dipyramidal
Volume of growth unit		$7.68 \cdot 10^{-29}$ m^3	$6.48 \cdot 10^{-29}$ m^3

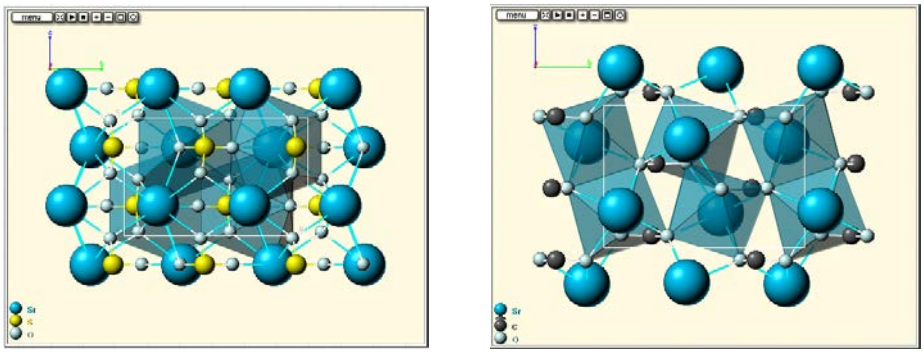

Figure 1. Three dimensional crystal structures of celestite (left) and strontianite (right) [4]

Celestite occurs as accessory diagenetic mineral in marine sediments. Celestite is usually formed by selective removal of strontium ions from groundwater by reaction with deposits of calcium sulfate.

[4] celestite and strontianite mineral data, eHistory. June 3, 2015. www.webmineral.com

Water containing a large amount of calcium ions and a small amount of strontium ions most commonly exists where limestone deposits occur in proximity. Celestite beds of appreciable thickness can thus be formed, in particular at the upper or lower boundaries of anhydrite or gypsum deposits. Such diagenic formation of celestite becomes more favored with the increase of the groundwater flow. Continuing diagenesis in a bicarbonate-rich environment may convert celestite to calciostrontianite. Small-scale occurrence of celestite may be produced following a similar mechanism where gypsum veins have penetrated into limestone [36]. A comparison of the crystallographic data and of the three dimensional crystals structures of celestite and strontianite is shown is Table 3 and Figure 1, respectively. Celestite and strontianite are isostructural minerals with almost identical lattice parameters. Therefore, using this couple of minerals in solid solution formation experiments, one can easily differentiate between reactivity related to the crystal structure and reactivity related to the nature of the anion [6]. This consideration was the motivation for the experiments on uptake of trivalent actinides and lanthanides as carried out in this thesis.

1.3 Reactive transport modelling

The development of reactive transport codes to model water-rock interactions has maintained a continuous interest in the kinetics of mineral crystallization and/or dissolution, with the ultimate need for the formulation of “kinetic rate laws” that could be implemented in codes for reactive transport modelling. The importance of reactive transport modelling has been proved for a considerable range of geochemical concerns. Nevertheless, discrepancies sometimes found between laboratory- and field derived weathering rates cause doubt on the reliability and relevance of numerical simulation outputs. The reasons for such discrepancies are manifold. For example the classical derivation of empirical rate laws based on the dissolution of freshly crushed powders may be misleading [37, 38]. In a numerical reactive transport simulation, three different phenomena have to be taken into account: (1) the geochemical reactions; (2) the kinetics of the reactions, and (3) the hydrodynamic transport rate compared to the reaction kinetics. The reaction rate is usually linked to the transport phenomena using the Damköhler number Da [39], in order to differentiate between kinetically controlled and thermodynamically controlled systems. Thus, the numerical model of the process is a system of differential equations that describe the flow, the kinetics and the thermodynamic equilibria. The major difficulty relies on the determination of the coefficients and functions for specific conditions relevant for the waste repositories. Therefore, it is important to simplify the dependencies between functions to solve the problem. The coefficients describing the reaction kinetics and thermodynamics need to be determined by laboratory experiments [40]. Required kinetic data for reactive transport modelling are among others, the reference-state mineral dissolution and crystal growth rate constants, activations energies, and reactive surface areas. These parameters are in general markedly less certain

than the related thermodynamic data. Particularly important for the celestite/strontianite systems are current gaps in the kinetics rate law for mineral growth (e.g. representation of various nucleation processes) and uncertainties in the relevant parameters (e.g. growth rate constant, activation energies, supersaturation threshold) [41]. Most of the kinetic parameters used in the literature for the modelling of the growth of celestite and strontianite are deduced from dissolution experiments; and it is known that dissolution and precipitation of the same mineral phase under similar conditions can follow totally different kinetics. Hence, it was crucial to experimentally investigate the nucleation and crystallization of the model minerals celestite and strontianite to have a set of more exact crystal growth kinetics data for reactive transport modelling and possibly explain the current inability to model diffusion experiments in a consistent way[42].

2 State of knowledge

2.1 Terminology of supersaturation and nucleation

Supersaturation is a state of a solution that contains more of the dissolved solute molecules than could be dissolved by the solvent under standard conditions (temperature, pressure). Supersaturation is an essential requirement for all crystallization processes and can be expressed in term of supersaturation ratio, S [-], a quantity sometimes referred to as the relative supersaturation, σ [-], or in terms of saturation index, Ω [-], according to the equations below:

$$S = \frac{IAP}{K_{SP}} \quad (1)$$

$$\sigma = \frac{IAP - K_{SP}}{K_{SP}} = S - 1 \quad (2)$$

$$\Omega = \log_{10}\left(\frac{IAP}{K_{SP}}\right) \quad (3)$$

where IAP is the ion activity product and K_{SP} the solubility product of the mineral phase of interest at a given temperature [43]. Let us consider the crystal growth/dissolution of celestite as model reaction to explain the equations above:

$$SrSO_4\,(s) \leftrightarrow Sr^{2+} + SO_4^{2-} \quad (4)$$

The equilibrium constant in terms of activities (a) of reactants and products at equilibrium is expressed as:

$$K_{SP} = (a_{Sr^{2+}})_{equil} * \left(a_{SO_4^{2-}}\right)_{equil} \quad (5)$$

whereas the activity of the solid phase is set by convention to a = 1.

However, for a solution not in equilibrium, the equilibrium constant is replaced by the ionic activity product, which has the same form as the equilibrium constant, but involves the actual (measured) activities:

$$IAP = (a_{Sr^{2+}})_{actual} * \left(a_{SO_4^{2-}}\right)_{actual} \quad (6)$$

The saturation index is a useful quantity to determine the saturation level of a solution with respect to the given mineral:

- Undersaturated $IAP < K_{SP}$ → $S < 1$ $\Omega < 0$
- Saturated (in equilibrium) $IAP = K_{SP}$ → $S = 1$ $\Omega = 0$
- Supersaturated $IAP > K_{SP}$ → $S > 1$ $\Omega > 0$

To avoid confusion, the terminology of nucleation processes used in this thesis, adopted from Mullin (2001) [43] is shown in Figure 2. The term primary nucleation will be used to qualify all nucleation

processes in systems that do not contain crystalline matter of the nucleating mineral, and the term secondary nucleation is reserved for nucleation on a crystal seed of the same chemical nature as the nucleating mineral. One can further distinguish between primary homogeneous nucleation and primary heterogeneous nucleation. Former takes place in the absence of any crystalline body in the system, which is hard to achieve in reality due to the ubiquity of colloids/nanoparticles in solution. The latter can occur when particles of foreign nature (with respect to the nucleating mineral) are present in the system.

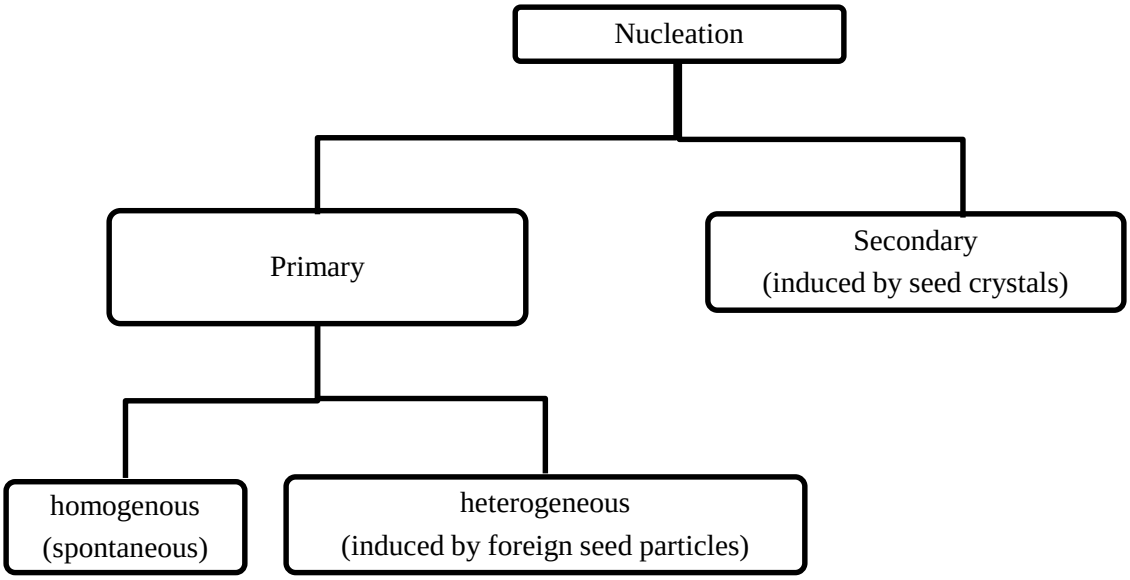

Figure 2. Nomenclature of nucleation processes according to Mullin [43].

The *induction period* or *induction time* is the period of time that usually elapses between the achievement of supersaturation and the appearance of crystals. In some systems, particularly at low supersaturation, another time lag called *latent period* may be observed. The *latent period* is defined as the period between the achievement of supersaturation and the onset of a significant change in the system, e.g. the occurrence of massive nucleation or some clear evidence of substantial solution desupersaturation [43].

2.2 Crystallization

Crystallization is a process in which an unordered state is transformed into an ordered phase. There are two main conditions where crystallization can be evaluated: i) under conditions where the host phase is at quasi-equilibrium with the nuclei, and ii) under conditions where the nuclei are very far from saturation. The former case is the basis for the Classical Nucleation Theory (CNT) [44-46], which includes treatment of nucleation from a purely statistical mechanics or thermodynamics formalism, or via the

so-called kinetic theories. The latter are in general better suited to handle dynamic phenomena, such as rate of nucleation, and allow some problematic aspects of pure thermodynamics based CNT (e.g. existence of an induction time, see chapter 2.4.3) to be overcome [47, 48]. The solubility of compounds in a solvent is in general limited by their solubility product. However, it is possible to prepare solutions containing more dissolved solute molecules than could be in solution under equilibrium conditions. Such solutions are said to be supersaturated. The terms “labile” (unstable) and “metastable” supersaturation was introduced by Ostwald to classify supersaturated solutions in which spontaneous primary nucleation would or would not occur [49]. A graphical representation of the metastable zone on a solubility-supersolubility diagram (Figure 3) originates from the work of Miers and Isaac [50, 51] on the relationship between supersaturation and spontaneous crystallization. The term supersolubility is the counterpart of solubility in supersaturated solutions.

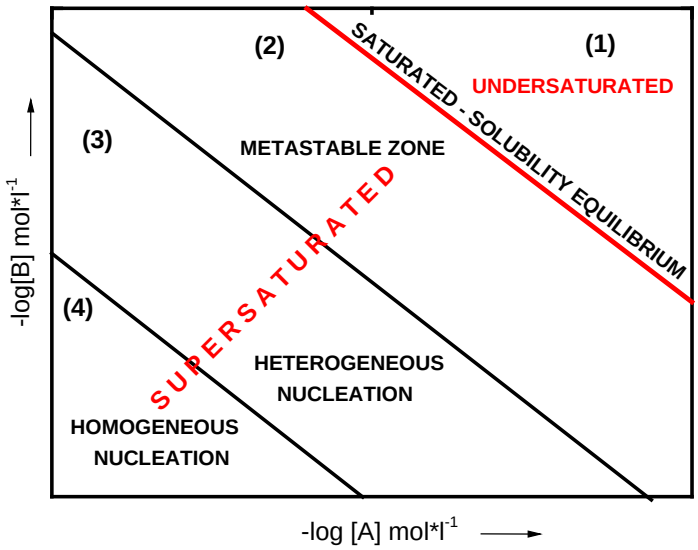

Figure 3. Stability areas for a binary electrolyte A_aB_b as a function of concentration in logarithmic scale.

In Figure 3, the areas being separated by the straight lines correspond to constant values of the ionic product $[A]^a \cdot B^b$ and their slopes correspond to –a/b. The undersaturated zone (1), where dissolution takes place, is separated from the supersaturated zone by the red line. The supersaturated zone is subdivided into three regions: if crystal seeds were placed in the metastable zone (2), growth would occur on it, but homogeneous nucleation is so slow that it is practically irrelevant; at higher supersaturation (lower left corner in Figure 3) follows the unstable zone: First a region where heterogeneous nucleation on foreign particles and growth may occur (3); and a region (4) where homogeneous nucleation is predominant. The supersaturation increases from (1) to (4). The theories

of nucleation and growth described here are related exclusively to crystallization processes from supersaturated aqueous solution at constant temperature; phenomena like condensation of a supersaturated vapor to a liquid phase or liquid-to-solid nucleation resulting from cooling of melts are not taken into considerations [52].

2.2.1 Classical crystallization

The CNT was originally derived for the condensation of a vapor into a liquid droplet [44-46], and has been analogized to explain growth of crystals from supersaturated solutions and melts [53-55].

2.2.1.1 Primary homogeneous nucleation from a supersaturated solution

The thermodynamic description of nucleation was developed in the frame of the CNT at the end of the 19th century by Gibbs [56], who defined the free energy change required for cluster formation, ΔG [kJ·mol^{-1}], as the sum of the volume excess free energy, ΔG_V, (i.e. the excess free energy between a very large particle with radius r -lim $r \rightarrow \infty$- and the solute in solution) and the surface energy free excess ,ΔG_S [kJ·mol^{-1}], (i.e. the excess free energy between the surface of the particle and the bulk of the particle). In case of crystallization from supersaturated solutions, the first term describes the spontaneous tendency of a supersaturated solution to undergo precipitation. During crystallization from a liquid phase, ΔG_V takes a negative sign and thus decreases the Gibbs free energy of the system. On the other hand, the appearance of an interface (between the feed solution and the formed nucleus) increases the free energy by an amount proportional to the surface area of the cluster. As a result, the growth of clusters is controlled by the competition between a decrease of ΔG_V, which favors growth, and an increase of ΔG_S, which favors dissolution (Figure 4).

In the CNT, the formation of the initial aggregates is reversible as long as their size remains under a specific size characterized by the critical radius, r_c (in m). The positive surface energy ΔG_S dominates at radii smaller than r_c, which causes an increase in the total free energy change upon growth. Thus the smallest clusters in solution typically redissolve. As the cluster size increases further, the total free energy passes a maximum (r_c), above which the total free energy continuously decreases and growth becomes energetically favorable, resulting in the formation of crystals [57].

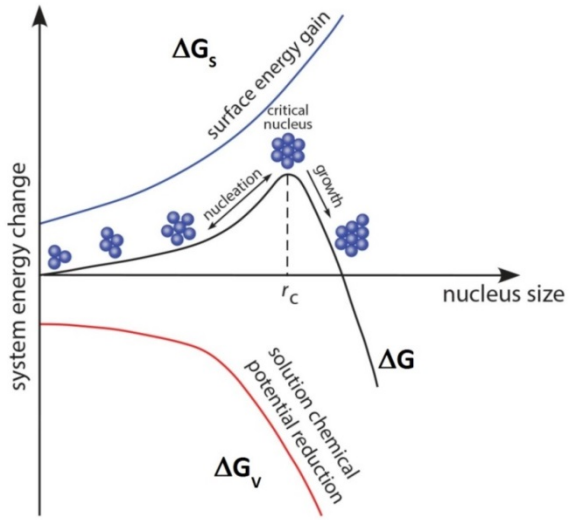

Figure 4. Schematic illustration of the size dependency of the energetics of nanoscopic nuclei within the framework of CNT [58].

Mathematically, the change of free energy associated with the process of homogeneous nucleation for spherical particles may be described as follows:

$$\Delta G = \Delta G_S + v\Delta G_V = 4\pi r^2\gamma + \frac{4}{3}\pi r^3 \Delta G_V \quad (7)$$

where $\gamma > 0$ represents the free energy per unit area of the nucleus-water interface (interfacial tension), v the volume of the nucleus. The two terms on the right hand side of equation (7) have an opposite effect on the system and depend with different potency (r^2 vs. r^3) on the radius r of the nucleus. Consequently, the free energy of formation ΔG passes through a maximum corresponding to the critical nucleus size (r_c). Figure 4 shows that the surface energy gain, ΔG_S, is a positive quantity, proportional to r^2. The reduction of the chemical potential of the system, ΔG_V (volume excess free energy), is a negative quantity proportional to r^3. The critical size for a spherical nucleus can be obtained from the first derivative of equation (7) as follow:

$$\frac{d\Delta G}{dr} = 8\pi r\gamma + 4\pi\gamma^2\Delta G_V = 0 \quad (8)$$

or

$$r_c = \frac{-2\gamma}{\Delta G_V} \quad (9)$$

The critical radius represents the smallest size of a stable nucleus. Generally, the smaller this critical radius, the easier nucleation can occur [59-61].

The energy barrier in primary heterogeneous nucleation is reduced compared to that in primary homogeneous nucleation according to:

$$\Delta G^*_{het} = S(\theta) * \Delta G^*_{hom} \quad (10)$$

where ΔG^*_{het} and ΔG^*_{hom} represent the energy barrier for heterogeneous and homogeneous nucleation, respectively. The shape factor $S(\theta)$ is given by

$$S(\theta) = \frac{(2 + \cos\theta)(1 - \cos\theta)^2}{4} \leq 1 \quad (11)$$

and it increases monotonically with the contact angle θ from 0 at 0° (wetting, when the energy barrier vanishes completely) to 1 at 180° (non-wetting, equivalent to homogeneous nucleation). In general, due to the larger surface energy of crystals compared to liquids and the usually large interfacial free energy between two solids, the effective shape factor is larger for a solid than for a liquid [62].

2.2.1.2 Nucleation on seed particles

Nucleation is often influenced by the presence of seed crystals from the same nature as the precipitating mineral (secondary nucleation), or by the presence of foreign bodies, such as the wall of the solution vessel and/or atmospheric dust particles (primary heterogeneous nucleation). Impurities can play the role of growth inhibitor or promote growth by acting as nuclei, depending on their nature and on the composition of the solution. Many reported cases of homogeneous nucleation are found on careful examination to have been induced by the presence of impurities. Indeed, it is widely accepted that true homogeneous nucleation is a rare event [63]. Accidental seeding can be caused by atmospheric dust which may contain nucleation accelerators, and it is nearly impossible to prepare a solution completely free of foreign bodies. For example, colloids are ubiquitous in natural groundwater and play an important role in the control and fate of nutrients and pollutants [64]. Nanoparticles are especially important because they have a large specific surface area, which facilitates sorption of significant quantities of substances [65-68]. For a given number of growing particles, the surface area increases continuously with ongoing growth. For nucleation from aqueous solution onto the surface of a foreign particle, the analogous situation is removal of the interface between the solution and the surface of the foreign particle. Intuitively, nucleation in such cases is identical to homogeneous nucleation, with the exception that it includes removal of the interface between foreign-particle and solution, and creation of two new interfaces (foreign-particle/crystal and crystal/solution). Thus the energy of the system in this case is lowered more than in a homogeneous nucleation event [47]. In fact, heterogeneous nucleation normally occurs at lower supersaturations compared to homogeneous nucleation. Therefore, the free energy for heterogeneous nucleation should be lower than that of homogeneous nucleation (see equation (10).

2.2.2 Non-classical crystallization

A new perspective has emerged in the last decade of the 20th century for the understanding of nucleation and growth processes that do not fit into the classical model. It emerged when the existence of alternative crystallization processes was indicated by an increasing body of evidence, accumulated primarily from experiments in the field of bio-mineralization and nanoscience. Contrary to classical crystallization pathways, non-classical crystallization occurs via colloidal intermediates, also referred to as "prenucleation clusters", and mesoscale transformation, in which crystalline structures are built and/or transformed from larger units instead of single solute ions/molecules [69-72]. An obvious example where the CNT will have limited applicability is in cases where the new and the old phases differ by more than two order parameters, e.g. density and structure [73, 74]. Unlike the constraints of CNT, nucleation and growth are no longer distinguishable steps according to non-classical crystallization. Investigating the nucleation of calcium carbonate in solution, Gebauer et al. [75] found evidence of very long lived clusters with size around 2 nm that play an important role in nucleation. The clusters present in both undersaturated and supersaturated solutions have also been found by others [76, 77] and indicate that the nucleus does not grow by single ion/molecule attachment, but by the coalescence of clusters of many ions, which is qualitatively different from the classical nucleation pathway [78].

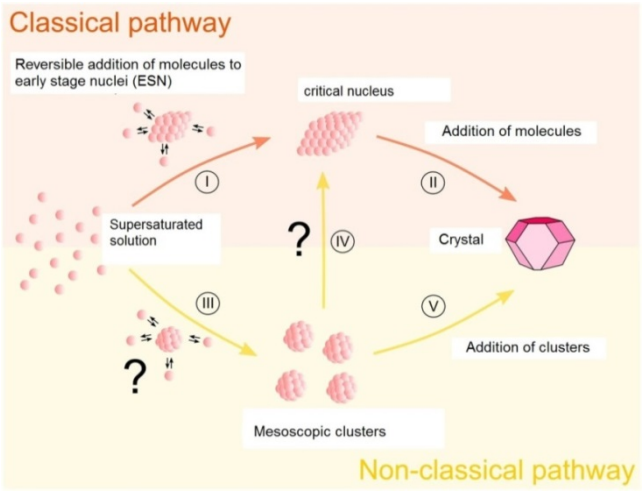

Figure 5. Comparison of classical (steps I and II) and non-classical (steps III, IV and V) nucleation pathways from the bulk solution to a crystalline phase. (Modified after Sleutel et al.[74]).

High resolution transmission electron microscopy (HRTEM) revealed that a crystallizing system can lower its energy state by an oriented attachment mechanism entailing a spontaneous self-organization of nanoparticles by which they re-orient themselves so that they are aligned in a common crystallographic direction; this is followed by aggregation and the formation of a new secondary

structure made of a few or up to hundreds of the primary structure. In this way, the system eliminates the interface between individual nanocrystals and reduces the total energy [58, 79]. The assemblage of nanoparticles that result from this reorientation is no longer a multigrain aggregate but rather a single crystalline structure. Figure 5 displays a schematic representation of classical versus non-classical crystallization pathways. The classical route (Figure 5, I and II) starts from primary building blocks like atoms, ions or molecules, forming clusters, which may grow via ion-by-ion attachment and unit cell replication, or re-dissolve again, depending on their size. For clusters with sizes greater than the critical size, the free energy of the system will become negative upon further particle growth, because the increase in surface energy will be overcompensated by the lattice energy (Figure 4). Contrary to the classical pathway, non-classical crystallization (routes III, IV and V) are always particle mediated and involve a mesoscopic transformation process [80].

2.3 Interpretation of induction periods for nucleation

It is well known that some time, referred to as induction time t_{Ind}, must elapse between the creation of supersaturation and the detection of a new solid phase in the system. The induction time is a function of the initial supersaturation and temperature; the presence of additives used as inhibitor or catalyst also has a significant influence. Additional factors influencing the induction time are the state of agitation, the presence of impurities and seeds, the viscosity of the solvent etc.[81-83] . The term "new phase detection" is open to a variety of interpretations, such as the onset of a change of solution properties, the first appearance of crystals of detectable size, etc. The measurable induction time is then thought to be a mixture of several components, namely a relaxation time (t_r) required for the system to achieve a quasi-steady-state distribution of molecular clusters, a time for the formation of a stable nucleus (t_n) and a time necessary for the subsequent growth of the nuclei to attain a detectable size (t_g) [43].

$$t_{Ind} = t_r + t_n + t_g \qquad (12)$$

t_g can be estimated, at least in principle, from a kinetic expression describing crystal growth by a particular mechanism. For the determination of t_n, one can assume that supersaturation remains virtually constant throughout the induction period. Once the relaxation time t_r has elapsed and supersaturation established, the size distribution of the nuclei, already present or newly formed, start to change until a steady-state distribution is achieved. This, incidentally, introduces another assumption, i.e. that the rate of nucleation is not extremely slow or fast, otherwise the achievement of the steady-state would be impossible. The relaxation time is usually in the order of 10^{-7}s for sparingly soluble inorganic electrolytes in aqueous solutions [84], therefore its contribution to the induction time is negligible. The ability of the LIBD method used in the present thesis to detect very small particles (~

20 nm) allows a detection of minor changes in the average nucleus size and hence minimizes the contribution of the time of growth to the induction time.

For homogeneous nucleation and considering the nucleation time to be much greater than the growth time, the induction time is given by

$$t_{ind} = A_1 \exp\left(\frac{\gamma^3 \vartheta_m^2}{k_B{}^3 T^3 \ln^2 S}\right) \quad (13)$$

and is dominated by the time needed for the formation of a critical nucleus in the system. The parameters A_1, γ (kJ·m^{-2}), ϑ_m (m^3), k_B (J·K^{-1}), T (K) and S are pre-exponential factor, interfacial tension between crystal and its surrounding supersaturated fluid, the volume of the growth unit, Boltzmann constant, absolute temperature and supersaturation ratio, respectively[85]. The induction time, according to the CNT, is inversely proportional to the nucleation rate J_S :

$$t_{Ind} \propto J_S^{-1} \quad (14)$$

The nucleation rate is then given by:

$$J_S = A \exp\left[\frac{-\Delta G}{k_B T}\right] = A \exp\left[\frac{-\beta \vartheta_m^2 \gamma_S^3 f(\theta)}{(k_B T)^3 \ln^2 S}\right] \quad (15)$$

where β is the shape factor related to the geometry of the nuclei (e.g. for a spherical nucleus, $\beta = \frac{16\pi}{3}$). For homogeneous nucleation, $f(\theta) = 1$ and the pre-exponential factor is $A = A_{hom}$. For heterogeneous nucleation, $f(\theta) < 1$, and $A = A_{het}$. Combination of equations (14) and (15) and rearrangement gives

$$\ln(t_{Ind}) = -C + \frac{B}{T^3 \ln^2 S} \quad (16)$$

where B and C are constants and can be expressed by the equations (17) and (18).

$$B = \frac{\beta \gamma_S^3 \vartheta_m^2 f(\theta)}{k_B^3} \quad (17)$$

and

$$C = \ln A \quad (18)$$

According to Söhnel and Mullin [86], the plot of $\ln t_{Ind}$ against $\ln S^{-2}$ over a wide range of supersaturation should give two slopes representing each a particular nucleation mechanism. The steeper slope represents the predominance area of homogeneous nucleation while the lower slope represents the area of heterogeneous nucleation. An intermediate corresponding to a smooth transition between the two nucleation mechanisms zone exists between the two slopes. For a limited supersaturation range and at constant temperature, no change is expected in the nucleation mechanism

and the relation between the induction time and the saturation ratio can be written in a linear expression as follow [87, 88]:

$$\ln(t_{Ind}) = k^* - n \ln(S) \quad (19)$$

with k^* being a constant with no physical meaning and n being the reaction order [89, 90].

2.4 Crystal growth kinetics

As soon as a critical nucleus is formed in a supersaturated solution, it begins to grow to a crystal. Several theories have been proposed to describe the rate and mechanisms of crystal growth. Advances in the kinetics of crystal growth from solution have been summarized by Ohara and Reid [91] and Söhnel and Garside [92]. Generally, two main processes that commonly occur in sequence are surface reactions at the interface between minerals and aqueous solutions, and diffusion of reactive species in the aqueous phase to and from the interface. The extent to which diffusion (Chapter 2.4.1) or surface reactions (Chapter 2.4.2) control the rate of mass transfer at the mineral surface depends on the degree of disequilibrium at the mineral-solution interface and in the bulk solution, on the mineral geometry, mineral structure and hydrodynamics of the system as well as on the magnitudes of the diffusion and surface reaction coefficients [93, 94].

2.4.1 Diffusion controlled growth

The diffusion theory dates back to the end of the 19th century, when Noyes and Whitney [95] considered the deposition of solids on the face of a growing crystal to be essentially controlled by diffusion processes. Diffusion theory is based on the assumption that there is a thin stagnant film of liquid adjacent to the growing crystal face through which molecules transport is limited by diffusion. Stirring results in homogenization of the bulk solution keeping the concentration close to the interface constant. The drop of concentration to that of bulk saturated solution takes place solely in this thin stagnant layer. The thickness of the stagnant liquid film depends on the relative velocity between solid and liquid, i.e. on the degree of agitation of the system. In stagnant aqueous solutions, film thicknesses of hundred micrometers have been measured, but values rapidly decrease when solution is stirred and drop to virtually zero in vigorously agitated systems [96]. Rates of growth are determined by both the diffusion coefficient D of the ions in solution, and the length of the diffusion path δ according to equation (20).

$$\frac{dm}{dt} = \frac{D}{\delta} \cdot A_{crystal} \cdot (c - c^*) \quad (20)$$

where m is the mass of solid deposited in time t over an area A(in m²) of the crystal surface; c is the concentration of the solute in the supersaturated solution and c^* the equilibrium saturation concentration [97]. As equation (20) would imply an almost infinite rate of growth in agitated systems with diminutive small diffusion path lengths, it is obvious that the concept of film diffusion alone is

not sufficient to describe the rates of crystal growth. The diffusion theory of crystal growth was modified by Berthoud [98] and Valeton [99], who suggested that the mass deposition on a growing crystal face was a two steps process: a diffusion process whereby solute molecules are transported through the bulk solution to the solid surface, followed by the integration of the solute molecules into the crystal lattice in a first order reaction. These two steps are driven by a concentration gradient and can be represented by the equations

$$\frac{\mathrm{dm}}{\mathrm{dt}} = \mathrm{k_d} \cdot A_{crystal} \cdot (\mathrm{c} - \mathrm{c_i}) \qquad \text{(Diffusion)} \qquad (21)$$

and

$$\frac{\mathrm{dm}}{\mathrm{dt}} = \mathrm{k_r} \cdot A_{crystal} \cdot (\mathrm{c_i} - \mathrm{c}^*) \qquad \text{(Integration)} \qquad (22)$$

with $\mathrm{c_i}$ as the solute concentration at the liquid-solid interface, $\mathrm{k_d}$ and $\mathrm{k_r}$ as coefficient of mass transfer by diffusion, and rate constant for the surface integration process, respectively. The diffusional process (equation (21) is in general considered to depend linearly on the concentration driving force. In practice, the interfacial concentrations are difficult to measure, it is therefore more convenient to eliminate the term $\mathrm{c_i}$ in the above equations by considering an overall concentration driving force, $\mathrm{c} - \mathrm{c}^*$, which can easily be measured. Relying on this simplification, equations (21) and (22) can be written as

$$\frac{\mathrm{dm}}{\mathrm{dt}} = \mathrm{K_G} \cdot A_{crystal} \cdot (\mathrm{c} - \mathrm{c}^*)^{\mathrm{g}} \qquad (23)$$

with $\mathrm{K_G}$ being the overall crystal growth coefficient and the exponent g the apparent order of the overall crystal growth process. Here, it is important to mention that the exponent g is not referred to the reaction order conventionally used in chemical kinetics [100]. Empirical data show that many salts crystallizing from aqueous solution give an overall growth rate order, g, in the range of 1 to 2, where $\mathrm{g} \neq 1$ suggests that the surface integration step is dependent on the concentration driving force in a non-linear manner.

It is obvious that the growth process is much more complex to be described alone by the two processes mentioned above. For an electrolyte crystallizing from aqueous solution, the following processes may all be taking place simultaneously [100]:

1. Bulk diffusion of the hydrated solute ions through the diffusion boundary layer
2. Bulk diffusion of the hydrated solute ions through the adsorption layer
3. Diffusion of hydrated or dehydrated solute ions along the crystal surface
4. Partial or total loss of the hydration sphere
5. Integration of ions into the crystal lattice

6. Counter-diffusion of released water through the adsorption layer
7. Counter-diffusion of water through the boundary layer.

2.4.2 Surface integration controlled growth

Surface integration is the process by which the growth units of a crystallizing mineral are incorporated into the crystal lattice after being transported to the surface of the crystal. The interpretation of the rates of dissolution and growth reactions at mineral surfaces is made possible by transition state theory (TST) and irreversible thermodynamics [101-103]. Two general mechanisms of surface reaction controlled growth are described here [85].

2.4.2.1 Two dimensional nucleation (2D nucleation)

The 2D nucleation mechanism implies that planar crystal faces are energetically unfavorable for crystal growth. A prerequisite for the initiation of crystal growth on a perfectly flat surface is the creation of a 2D nucleus, which provides incorporation sites (steps and kinks) for the attachment of further growth units. Several models have been proposed for crystal growth by means of 2D nucleation: the mononuclear model, the poly-nuclear model and the "birth-and-spread" model. These theories use different expressions of the rate at which the growth units spread across the crystal surface compared with the time taken to form a new nucleus for a new layer [91]. The rate limiting step in the mononuclear model is the formation of a nucleus, since the subsequent spreading across the crystal surface is assumed to be infinitely rapid. For the poly-nuclear model, the velocity of spreading is taken as zero and the crystal surface can solely be covered by the accumulation of a sufficient number of nuclei. Contrary to the two models described above representing two extreme cases almost never observed in experiments, the "birth-and-spread" model assumes the formation of nuclei and their subsequent growth to occur at a finite rate. In this case, new nuclei can form on top of an uncompleted layer.

2.4.2.2 Growth at screw dislocations

The energetics of layer growth predicts crystal growth to occur only at relatively high supersaturation (needed to overcome the energy barrier associated with 2D-nucleation). Nevertheless, crystal growth at supersaturations lower than predicted has been observed [104]. In order to explain this, a growth model based on dislocation theory has been proposed by Frank [105]. A screw dislocation can give rise to a spiral-like step, which does not disappear during growth. Hence, the formation of a 2D nucleus at the crystal surface is not a requirement to sustain growth. A schematic diagram of the formation and development of spiral growth is shown in Figure 6. In the first stage the dislocation creates a step (Figure 6 a). The attachment of growth units to the steps leads to its advancement and thus generating a second step (Figure 6 b). This second step will not advance as long as its length does not exceed $2r_{2D^*}$;

because any growth of steps with a smaller size is thermodynamically hindered. Once the second step starts advancing, it will generate a third step, the advancement of which will in turn be governed by the same thermodynamic restrictions (Figure 6 c). A fourth step will appear Figure 6 d) and so on.

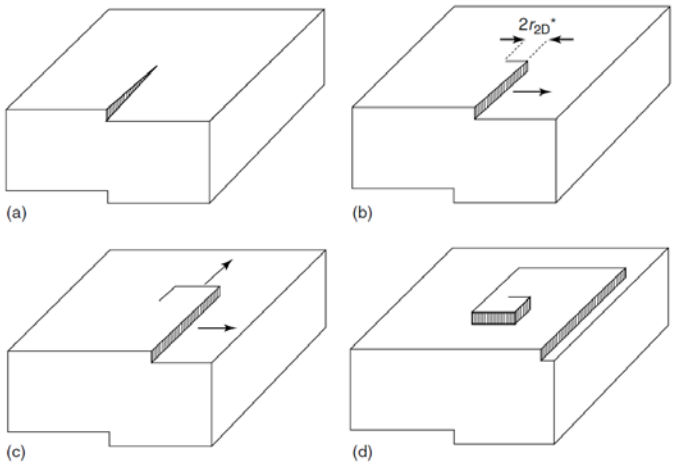

Figure 6. Development of a polygonal spiral (source Cubillas et al. [106])

This will generate a spiral pattern around the core of the dislocation, and a self-perpetuating source of steps where growth requires lower supersaturation. The theory of crystal growth at screw dislocation has further been refined by Burton, Cabrera and Frank, giving rise to the well-known BCF theory [106, 107]. In the BCF theory, the growth of the spiral is considered to be limited by the diffusion of adsorbed growth units across the crystal surface and the growth rate is given by:

$$R_G \propto \frac{\sigma^2}{\epsilon_C} \tanh\left(\frac{\epsilon_C}{\sigma}\right) \qquad (24)$$

where the supersaturation parameter σ is defined by equation (2) and ϵ_C is a complex temperature-dependent constant which includes parameters depending on step spacing. At low supersaturations, equation (24) approximates to $R_G \propto \sigma^2$, and at high supersaturations to $R_G \propto \sigma$ [94].

2.4.3 Determination of crystal growth rates

The general growth rate laws, based on physical models of surface-controlled crystallization limited by adsorption, spiral growth at screw dislocation, or by two-dimensional nucleation on crystal surfaces, have been summarized by Nielsen [108]. In the framework of the transition state theory[101], the net rate of adsorption onto a crystal surface per unit area can be described as:

$$R_{ads}^{net} = k_{ads}(S^m - 1)^n \qquad (25)$$

where S and k_{ads} are the supersaturation ratio and the rate constant, respectively, m and n are empiric parameters. An equation such as (25) has been used to successfully model quartz

precipitation/dissolution suggesting an adsorption mechanism for precipitation with silica as the adsorbed species, and a simple desorption mechanism for the reverse reaction [109, 110]. The description of the variation of rate constant k with temperature, according to an Arrhenius-type equation, is given by:

$$k = A \cdot \exp\left[\frac{-E_a}{RT}\right] \quad (26)$$

where A represents a pre-exponential factor, R stands for the gas constant, E_a represents an activation energy and T the absolute temperature [111].

Crystal growth rates from mixed flow reactor experiments can be determined using the mass balance equation:

$$R_{input} = R_{out} + R_G A_{crystal} \quad (27)$$

where R_{input} and R_{output} (mol·s^{-1}) are the rates of flow of the solute molecules into and out the reactor, respectively. R_G is the rate of crystal growth within the system in moles·m^{-2}·s^{-1}, and $A_{crystal}$ is the surface of seed crystal in m^2. Equation (27) can be rewritten as follows:

$$R_G = \frac{(C_{input} - C_{output})Q}{A_{crystal,\ initial}} \quad (28)$$

where C_{input} and C_{output} [mol·l^{-1}] are the concentration of the influent and effluent solutions, respectively, Q [l·s^{-1}] is the flow rate, and $A_{crystal,\ initial}$ [m²] is the surface area of the seed crystals before the experiment [112]. Using the initial surface area of the seed crystals presupposes the increase of crystal size during growth to be proportional to the decreases of its specific surface area, resulting in a constant surface area during the crystal growth. According to the physical models of surface controlled crystallization, a plot of the growth rates against S-1 shows a linear dependency for adsorption controlled rate law (continuous growth model), a parabolic dependency for growth at screw dislocation and an exponential dependency for surface nucleation limited rate law. The growth at screw dislocation and surface nucleation models operate under low and moderate supersaturation levels, respectively [113]

2.5 Co-precipitation

Co-precipitation occurs when foreign solutes are incorporated in the body of a mineral of stoichiometric composition. For example, crystallization of celestite from a solution containing only sulfate, strontium and water, will result in pure celestite. If other cations (e.g Ba^{2+}) are added to the solution, a fraction of them may co-precipitate with celestite. The mineral formula will then be $(Sr_xBa_y)SO_4$. The indices x and y represent the mole fraction of strontium and barium, respectively.

The incorporation mechanisms playing a role in co-precipitation reactions can be summarized as follow [114, 115]:

- *Isomorphous replacement*: the dopant ion (trace element) can be fixed at lattice sites usually occupied by regular ions of the host mineral (e.g. Sr^{2+} occupies a Ba^{2+} in barite). The chemical affinity between the substituted and the dopant ion (similar charges and ionic radii, analogous electronic configuration) favors this mechanism [115].
- *Incorporation in crystal defects*: the dopant ion can occupy sites of vacancy or dislocation in the host crystal [115].
- *Non-uniform incorporation*: trace components can be incorporated into a host mineral through physisorption of discrete particles from the solution. For example, the sticking of colloidal particles on the surface of a growing mineral can be follow by their entrapment in the bulk crystal, when additional layer of the precipitating host solid are deposited on them [115].

One can further differentiate between solid solution co-precipitation, adsorption co-precipitation and occlusion co-precipitation [114]. Solid solution co-precipitation occurs when the dopant ion actually enters the crystal lattice of host mineral. Small crystals have very large surface area. In solution, the ions on the surface area attract ions of the opposite charge, causing co-precipitation by adsorption. Occlusion co-precipitation occurs via the entrapment of ionic impurities within the crystals. Co-precipitation can be accompanied by deformations in the crystal structure of the host mineral due to differences in ionic radii, and by the creation of a charge deficit/excess, e.g. the replacement of a bivalent Sr^{2+} ion by a trivalent Cm^{3+} or Eu^{3+} leads to an excess of positive charge in the near field of the substituted ion, which must be compensated. Several mechanisms for the charge compensation have been proposed [116]:

- The *coupled ion substitution* mechanism, which can be exemplified by the substitution of two adjacent Sr^{2+} ions by one trivalent ion and one Na^{+} ion (background electrolyte) in the lattice.
- The *ion substitution adjacent to a vacant site* mechanism can be illustrated by the substitution of three contiguous Sr^{2+} ions by two trivalent ions, whereas the third cation site is left vacant.
- The *coordinate rearrangement* mechanism calls for a lattice deformation and changes in the local coordination environment of the substituted ion, so that charge is balanced on a local scale

The preceding considerations show that there is no obvious solution to the problem of predicting the correct stoichiometry and structure for a minor end-member in the case of heterovalent substitution. This causes the thermodynamic modeling of such solid solutions to be a complicated issue [116, 117]. Thermodynamics alone is usually insufficient to predict growth-rate dependencies of trace element

partitioning into host mineral solid solutions, and therefore, kinetic models have been proposed in order to obtain additional information about the mechanistic understanding of solid solution formation [118]. Two uptake kinetic models that have been proposed by Thien et al. [118] are the growth surface entrapment model and the surface reaction kinetic model:

- The *growth surface entrapment model* [119] stipules that the surface of a crystal in equilibrium with solute bearing fluid generally has a composition that differs from that of the bulk crystal. For a growing crystal, the surface composition may be "trapped" by the newly formed lattice to a degree that depends upon the growth rate and the mobility of atoms in the near-surface region: this growth entrapment is promoted when growth is rapid, while a high mobility of atoms in the near-surface region works against it [119].
- *The surface reaction kinetic model* [120] is based on the requirements for dynamic precipitation-dissolution close to equilibrium. For conditions where ionic transport to the growing surface is not rate limiting, the proximity to equilibrium conditions is determined by the ratio of the net precipitation rate to the gross forward precipitation rate [120].

2.6 Time-resolved laser fluorescence spectroscopy (TRLFS)

Time-resolved laser fluorescence spectroscopy (TRLFS) is a highly sensitive spectroscopic technique, based on the spontaneous emission of light, a phenomenon also called luminescence. Luminescence describes the process of radiative decay where an excited substance emits electromagnetic radiation upon de-excitation. When such de-excitation occurs between electronic states of different spin multiplicities due the spin exchange in a process referred to as *inter system crossing* ($\Delta S \neq 0$), the luminescence process is referred to as phosphorescence. In the case of transition between levels of same spin multiplicities ($\Delta S = 0$), the term fluorescence is used instead [121-123]. Generally, the relaxation time of phosphorophores is longer than that of fluorophores. Some f-elements in aqueous solution/suspension or solid solution relax through intensive luminescence emission. Examples of actinide and lanthanide luminophores are Cm(III) and Eu(III), respectively. The characteristic optical spectra of these inner transition elements originate from f-f transitions, occurring between the partly filled 4f (lanthanides) or 5f (actinides) energy levels [121, 124]. The sensibility of f-f transitions to changes occuring in the ligand field is a feature that makes TRLFS an extremely useful tool to account for the complexation/speciation of f-elements [123].

2.6.1 Spectroscopy of Cm(III)

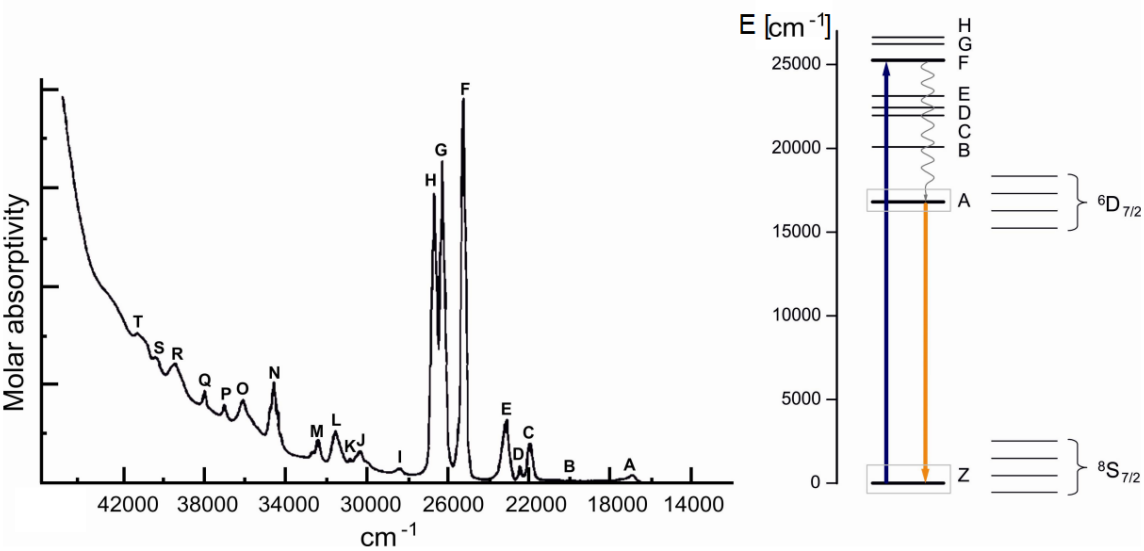

Figure 7: Left: the absorption spectrum of Cm(III) (0.06 mol·l^{-1}) in $HClO_4$ (1 mol·l^{-1}) is characterized by three particularly intense transitions F, G and H. Right: energy levels of Cm(III) in the energy range from 0 to 27000 cm^{-1}. The ground state is represented by Z. Figures adapted from Huittinen[123] and Carnall[125].

The most stable oxidation state for curium ions in solution is +III [126]. The trivalent Cm(III) has the electronic configuration [Rn]5f^7, which assumes a $^8S_{7/2}$ ground state in accordance to the Hund's rule. In such systems where the ground state is made mainly of electrons with s-character, the splitting of the emission bands in the crystal field is not expected. This trend is well fulfilled for Gd(III), which is the 4f analogue of Cm(III). However, the ground state of Cm(III) has approximately 19% of p-character due the spin-orbit interactions. Accordingly, the behavior of Cm(III) is clearly different from that of electronic states with pure s-character [127, 128]. The curium absorption spectrum (Figure 7, left) shows a multitude of f-f transitions, with the most intensive ones being the F, G and H transitions at 25214 cm^{-1}, 26240 cm^{-1} and 26638 cm^{-1}, respectively.

The plot on the right side of Figure 7 shows the energy levels of a free Cm(III) ion after excitation by UV light (25214 cm^{-1}). Cm(III) is excited from the ground state to the F-level, followed by non-radiative relaxation to the excited state A ($^6D_{7/2}$) with the lowest energy (16840 cm^{-1}). The energy levels of the $^8S_{7/2}$ state undergo a relatively small crystal field splitting (~ 7.5 cm^{-1}) and can be assumed to be degenerated in the aquo ion. Relaxation from the $^6D_{7/2}$ state (which is separated in four crystal field levels) to the ground state is accompanied by fluorescence emission. The spectrum of this emission at room temperature (293 – 298 K) shows a broad peak with a maximum at 593.8 nm as emission occurs

at least from the two lowest energy levels of $^6D_{7/2}$. Cm(III) TRLFS is based on the analysis of this fluorescence, which allows a monitoring of Cm(III) speciation [129]. A variation in the first coordination sphere due to complexation, sorption, incorporation etc. results in a stronger crystal field splitting of the $^6D_{7/2}$ level compared to the aquo ion. This leads to a decrease of the lower $^6D_{7/2}$ sub-levels. As a consequence the corresponding fluorescence peak is shifted to lower energy, i.e. higher wavelength (bathochromic shift), in comparison with the aquo ion. This peak shift generally increases with the "strength" of complexation and the number of coordinated ligands [130].

Both the ground state (Z) as well as the first excited state (A) are four-fold split into the so-called *Kramer-doublets*: Z_{1-4} and A_{1-4}. Reported values of the ground state splitting range from 2 to 61 cm^{-1} [6, 127, 128, 131-134]. The size of the splitting is a function of the ligand, the binding character, and the metal-ligand distance [128]. Contrary, the splitting of the A-level is relatively high (300 cm^{-1}) and comparable to the thermal energy at room temperature kT = 210 cm^{-1}. Thus, emission at room temperature occurs not only from the lowest crystal field level. Only at sufficiently low temperature, emission of these called "*hot bands*" is suppressed resulting in sharper fluorescence peaks. It is therefore important for the interpretation of the emission spectra of Cm(III), to differentiate between peaks of individual species and A_2-bands. The emission spectrum of the Cm(III) aquo ion is shown in Figure 8 [123, 124].

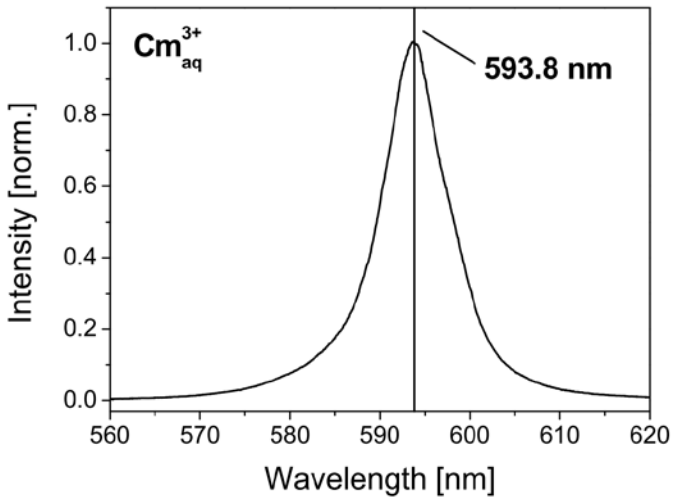

Figure 8. Fluorescence spectrum of Cm(III) in $HClO_4$ (0.1 $mol \cdot l^{-1}$) at 298 K [135]

Strictly speaking, the transition from the $^6D_{7/2}$ to the $^8S_{7/2}$ involves a spin exchange, causing the curium ion to relax through phosphorescence emission. However, this process is referred to in the most cases as fluorescence. We will acknowledge this convention in the present work, and thus, curium relaxation by emission of electromagnetic radiation will be referred to as fluorescence in the following text.

2.6.2 Spectroscopy of Eu(III)

In the UV spectral range, the 4f-elements generally show broad and intensive absorption bands resulting from the parity-allowed f → d transitions. Contrary, the parity-forbidden f →f transitions give rise to sharp, less intensive transitions, which are located in the VIS spectral range [136, 137]. The 4f-electrons are strongly shielded by the (n+2)s and p shells, and hence their interaction with the ligand field is relatively low. The resulting ligand field effect is weak and accordingly, the shift of the emission peaks upon variations in the ligand field is relatively small. Contrary, the symmetry of the ligand field has a significant influence on the splitting of the individual bands of the spectrum.

Europium was chosen in this thesis as surrogate for trivalent actinides. The electronic configuration of the Eu(III) ion is [Xe]$4f^6$, leading to a $^7F_0$ ground state according to the Hund's rule. In Eu(III) TRLFS the luminescence emission between f-states of higher energy to the ground level is monitored. The energy levels of Eu(III) in the VIS spectral range are shown in Figure 9.

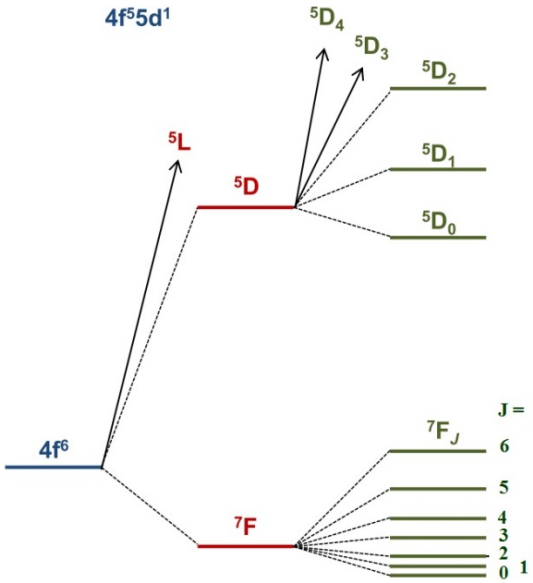

Figure 9. Energy levels of Eu^{3+} in the visible spectral range, adapted from Schmidt [137] and Ruff [138].

Fluorescence occurs in Eu(III) almost exclusively from the first excited state $^5D_0$. The observed bands in the fluorescence emission spectrum correspond to the transitions to the sub-levels of the ground state $^7F_{0\text{-}6}$. Each sub-level in turn can be split in (2J+1) levels. The first three transitions ($^5D_0 \rightarrow {}^7F_0$, $^5D_0 \rightarrow {}^7F_1$, and $^5D_0 \rightarrow {}^7F_2$) are of particular interest regarding the identification, structural characterization, and speciation of Eu(III) complexes.

The $^5D_0 \rightarrow {}^7F_0$ transition shows no additional splitting (J=0 → J=0) and always gives a single emission band for each excited Eu(III) species [139]. In case of high spectral resolution, the number of Eu(III) species can be determined from the excitation or emission spectra. Further, the intensity of the $^7F_0$-transition correlates with the symmetry of the complex, and therefore, can be used as indicator to track changes in the symmetry of the complex. The $^7F_0$-transition is forbidden in complexes with an inversion center (e.g. Eu^{3+} aquo ion) [137, 140], and relatively weak in the presence of other symmetry elements, so that his intensity can be used for symmetry assessments.

Contrary to the $^5D_0 \rightarrow {}^7F_0$ transition, the $^5D_0 \rightarrow {}^7F_1$ transition is a parity-allowed transition and its intensity is accordingly high. This intensity is insignificantly influenced by the chemical environment of Eu(III) and can be used therefore as an internal intensity standard. The hypersensitive $^5D_0 \rightarrow {}^7F_2$ transition is highly sensitive to changes in the inner coordination sphere. The intensity ratio of the two bands can provide important information regarding the structure of the Eu(III)-complexes [121, 141-143].

Another essential aspect of the Eu(III) TRLFS is the interpretation of the splitting patterns of the emission bands with $J \neq 0$, which are determined by the center of symmetry present in the complexes, and can be described qualitatively using the group theory. A sufficient resolution of the single crystal field transitions can usually be achieved only at low temperatures and on solid samples. Using Table 4, conclusions about the local symmetry of Eu(III) can be drawn from the splitting patterns [121]. However, polarization dependent measurements are necessary for an exact determination of the point group of a complex.

Table 4. Splitting of the $^5D_0 \rightarrow {}^7F_J$- transitions of Eu(III) at different center of symmetry

	Splitting					
Symmetry	$^7F_0$	$^7F_1$	$^7F_2$	$^7F_3$	$^7F_4$	Point group
Icosahedron	1	1	1	2	2	
Cubic	1	1	2	3	4	O_h, O, T_d, T_h, T
Hexagonal	1	2	3	5	6	D_{6h}, D_6, C_{6v}, D_{3h}, C_{3h}, D_{3d}, D_3, C_{3v}, C_{3i}, C_3
Pentagonal	1	2	3	4	5	D_{5h}, C_{5h}, C_{5v}, C_5, D_5
Tetragonal	1	2	4	5	7	D_{4h}, D_4, C_{4v}, C_4, D_{2d}, S_4
Low	1	3	5	7	9	D_{2h}, D_2, C_{2h}, C_s, C_1, C_i

2.6.3 Fluorescence lifetimes

The average amount of time that the molecules of a substance remain in the excited state prior to return to the ground state is called fluorescence lifetime [122]. The fluorescence lifetime can yield information

about the molecular environment of a fluorescent molecule [144]. Generally, the fluorescence lifetime of a fluorophore can be influenced by factors such as ionic strength, hydrophobicity, binding to ligands, and the proximity of molecules that can deplete the excited state by resonance energy transfer [145]. For the measurement of the fluorescence lifetime, the delay time (time between the laser pulse and the detection by the camera) is increased step by step and the fluorescence emission is detected after each step. The recorded emission spectra at different delay times are then integrated for a constant time window to obtain a decay plot which follows exponential fluorescence decay, depending on the fluorescence decay rate (k_{obs}) in relation to the ligand exchange rate and the number of species present. If the fluorescence decay rate of the excited species is slow compared with the ligand exchange rate, an average lifetime of the species and a mono-exponential decay is expected. If more than one species are present and the fluorescence decay rate is fast in comparison to the ligand exchange rate, multi-exponential decay is expected [123, 146, 147]

The fluorescence decay rates (k_{obs}) of the Cm aquo ion and Eu aquo ion are approximately 15 ms^{-1} and 9 ms^{-1} respectively, corresponding to a fluorescence lifetime (τ) of 68 µs and 110 µs, respectively. The relation between fluorescence lifetime and the number of water molecules (nH_2O) in the first coordination sphere of Cm(III) is given by the empirical Kimura equation (29) [148]. Accordingly, a similar relation, known as the Horrocks' equation (30) has been derived for the Eu(III) ion [149]:

Cm(III) $nH_2O = 0.65\ k_{obs} - 0.88$ (29)

Eu(III) $nH_2O = 1.07\ k_{obs} - 0.62$ (30)

with $k_{obs} = \tau^{-1}$; k_{obs} in ms^{-1}

The equations above assume that only OH-vibrations are involved in fluorescence quenching processes. Using the above given fluorescence decay rates for the Cm aquo and Eu aquo ions in the equations (29) and (30) yields the number of water molecules surrounding the ions, namely approximately nine for both curium and europium.

2.7 The $SrCl_2 – Na_2SO_4 – H_2O$ and $SrCl_2 – Na_2CO_3 – H_2O$ systems

In an aqueous suspension of celestite or strontianite particles, the cation Sr^{2+} and the anions (SO_4^{2-}, CO_3^{2-}) that dissolve from the mineral surface interact with the solvent according to the following equilibria [150-155]:

Celestite aqueous solution			log K (298 K)
$SrSO_{4(S)}$	⇌	$Sr^{2+} + SO_4^{2-}$	6.613
$SrSO_{4(aq)}$	⇌	$Sr^{2+} + SO_4^{2-}$	2.29

$SrOH^+$	+	H^+	⇌	Sr^{2+}	+	H_2O	13.29
SO_4^{2-}	+	H^+	⇌	HSO_4			-1.91

Strontianite aqueous solution							log K (298 K)
$SrCO_3(s)$			⇌	$Sr^{2+} + CO_3^{2-}$			9.27
Sr^{2+}	+	CO_3^{2-}	⇌	$SrCO_3(aq)$			-2.81
$CO_{2(aq)}$			⇌	H^+	+	HCO_3^-	6.35
HCO_3^-			⇌	H^+	+	CO_3^{2-}	10.33

The solubility of each mineral is affected by the hydrolysis of its cations. Due to the participation of protons (H^+) in these processes, the pH of the suspension affects the mineral solubility. Figure 10 shows the distribution of the major aquatic species of strontium sulfate and strontium carbonate as a function of pH and the stability field of the crystalline phases $SrSO_4(c)$ and $SrCO_3(c)$.

The exchange reaction of SO_4^{2-} ions of celestite with CO_3^{2-} has been the subject of many investigations over the last century [23, 24]. In suspension of celestite particles in contact with the atmosphere, a transformation of celestite to strontianite may be observed. Prerequisite for this transformation is the dissolution of the atmospheric carbon dioxide in the aqueous solution to form carbonate ions (CO_3^{2-}). These may react with the strontium ions in celestite. This "carbonation" reaction depends on pH and on the concentration of carbonate ions; which in turn depends also on pH, temperature and CO_2 partial pressure. At atmospheric CO_2 partial pressure, a solution with sulfate ions concentration of $8.6 \cdot 10^{-4}$ $mol \cdot l^{-1}$ (given by the stoichiometric solubility of celestite) will form preferentially celestite in acidic solutions while for pH higher than about 7.75, the stable compound would be strontianite. Accordingly, when celestite is in solution of pH ≥ 7.75, its surface will transform to strontianite and the pH of the system will naturally decrease to reach the equilibrium pH at which both celestite and strontianite coexist ($pH_{equilibrium} = 7.75$) [152].

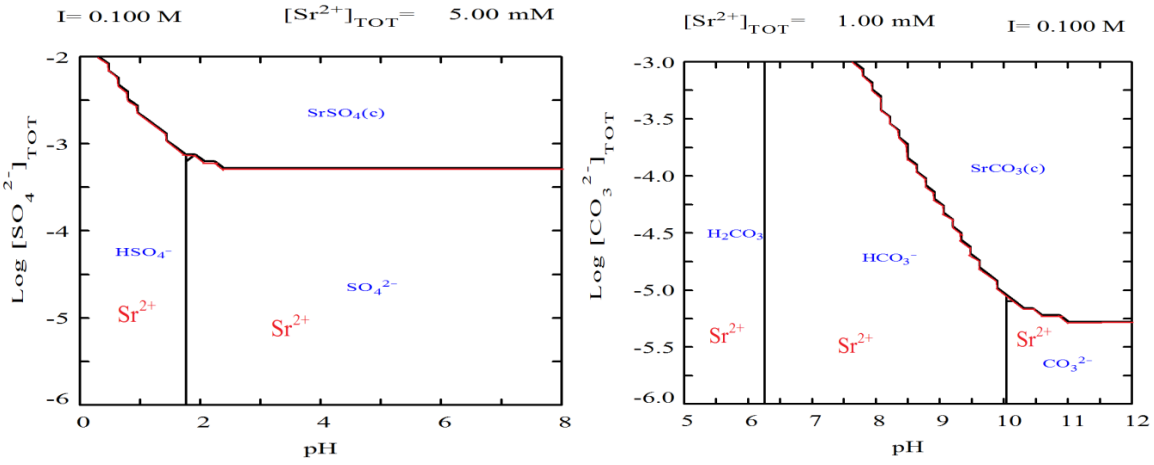

Figure 10. Predominance area for strontium sulfate (left) and strontium carbonate (right) in aqueous solution at 298 K, ionic strength of 0.1 M. The total strontium concentration is $1 \cdot 10^{-3}$ and $5 \cdot 10^{-3}$ $mol \cdot l^{-1}$ for the strontium carbonate and strontium sulfate solutions, respectively.

2.8 Previous studies on celestite and strontianite crystallization

Nucleation and growth of celestite and strontianite from supersaturated solution have been investigated by many authors under different experimental conditions. The key parameters determined in these publications are summarized in Table 5. Campbell and Nancollas [156] studied the kinetics of crystallization and dissolution of strontium sulfate by following the change in conductivity which occurs when supersaturated or under-saturated solutions are inoculated with seed crystals. They made the observation that the growth and dissolution of strontium sulfate crystals follow an equation in which the rate is proportional to the square of the relative supersaturation or under-saturation in the solution. Experiments of Sühnel et al. [157] dealing with the crystallization of unseeded aqueous solutions of $SrSO_4$ at supersaturations ratio $S < 16$ showed that the nucleation in aqueous solution is controlled by the heterogeneous nucleation mechanism, and that growth at low supersaturation is controlled by the surface reaction mechanism. In batch experiments, Yeboah et al. [158] have determined the growth rate constants for the spontaneous precipitation of strontium sulfate at temperatures of 303 to 398 K, pressure from standard to 13.8 MPa, and ionic strengths of 0.02 to 4.5 molal. Once again, they found the precipitation to obey a first-order rate equation at very low supersaturations, and a second-order rate equation at moderate and small supersaturations. Malollari et al [159] studied the spontaneous precipitation of strontium sulfate from equimolar aqueous solutions under conditions of constant supersaturation, using sodium nitrate as an inert background electrolyte for the adjustment of the ionic strength of the solution. They reported that i) at supersaturation ratio $S \geq 8$, the precipitation was homogeneous and a value of 88 $mJ \cdot m^{-2}$ was calculated for the crystal-solution interfacial tension; ii) the rates of crystal growth showed a first order dependency on the relative solution supersaturation,

which was interpreted as a surface-controlled growth mechanism. At supersaturation ration $S \geq 8$ however, the reaction order increased to 4 suggesting a predominance of nucleation processes. Investigations on the influence of additives such as poly-phosphonates [160, 161] and silica [162] on the crystallization of strontium sulfate from aqueous solutions have been reported.

A number of studies are present in the literature for strontianite. In 1965, Helz [163] studied the solubility of natural strontianite in aqueous solutions in equilibrium with a vapor phase containing CO_2 at temperatures between 323 and 473 K and pressures up to 50 atm. At each temperature, the author found the strontium concentration in solution to be proportional to the cube root of the fugacity of CO_2 in the vapor phase and inversely proportional to the mean activity coefficient of $Sr(HCO_3)_2$. Further, the solubility of strontianite was found to decrease with increasing temperature [163]. Two decades later, Busenberg proposed an equation describing the temperature dependency of the equilibrium constant for the strontianite solubility between 275 and 368 K:

$$\log K_{SP} = 155.0305 - \frac{7239.594}{T} - 56.58638 \cdot \log T \qquad (31)$$

where T is the absolute temperature in Kelvin. The log K_{SP}-value (solubility product), Gibbs energy, enthalpy and entropy of the strontianite dissolution at 298 K were found to be -9.27 ± 0.02, 52.92 ± 0.08 kJ·mol^{-1}, -1.67 ± 1.30 kJ·mol^{-1} and -183.1 ± 4.0 J·mol^{-1}·K^{-1}, respectively [164]. Investigating the kinetics of crystallization of strontianite from strontium bicarbonate solutions, Zeppenfeld et al. [165] have reported homogeneous primary nucleation to be dominant at high supersaturation, whereas heterogeneous primary nucleation prevails at low supersaturations. The crystal growth rate increases with increasing supersaturation and is mostly diffusion-controlled at high supersaturation. At lower supersaturation the rate of crystal growth is mainly governed by the integration of ions into the crystal structure.

None of the studies cited above deals with the direct homogeneous nucleation of strontium carbonate from supersaturated solutions, nor were any studies conducted under experimental conditions potentially relevant for nuclear waste disposal. For this reason, one aim of the present work was to determine kinetic parameters for the crystallization of celestite and strontianite that could be implemented in reactive transport codes at low supersaturations.

Table 5. Previous studies on the crystallization of celestite from supersaturated solutions

T [K]	Ω	I[5] [mmol·kg^{-1}]	Bg.E.[6]	t_{Ind} [min]	R	reference
298	2.2 - 2.8	n.a.[7]	n.a.	0.07 - 0.93		Pina et al. [162]
298	0.48 - 0.51	n.a.	n.a.	n.a.	0.70 - 4.72[8]	Pina et al. [162]
298	0.2 - 0.62	700	NaCl		0.67 - 7.16[9]	Hamdona [160]
298	0.82 - 1.56	2.4 - 8.6	$NaNO_3$	8 - 240	0.9 - 22.9[10]	Mallolari [159]
30 - 125	0 - 0.60	20 - 4500	NaCl		0.42 - 130[11]	Yeboah [158]
25	< 1.20	n.a	n.a	0.74 - 42		Sühnel [157]
25 – 90	0.95 – 2.95	0 - 6	NaCl	0 - 333		He [161]

[5] Ionic strength
[6] Background electrolyte
[7] Data not provided in the corresponding literature
[8] Growth rate in nm·s^{-1}
[9] Growth rate in 10^{-6} mol·m^{-2}·s^{-1}
[10] Growth rate in 10^{-3} mol·min^{-1}
[11] Growth rate in mol·min^{-1}

3 Materials and methods

3.1 Materials

Sodium chloride (NaCl), sodium sulfate (Na_2SO_4), sodium carbonate (Na_2CO_3) and strontium chloride hexahydrate ($SrCl_2 \cdot 6H_2O$) were analytical grade chemicals purchased from Merck (Merck chemicals, Germany). Strontium sulfate ($SrSO_4$) and strontium carbonate ($SrCO_3$) (puratronic®, 99.9965% metal basis) were purchased from Alfa Aesar (Alfa Aesar GmbH & Co KG, Germany). Glass beads (Type S Microglass. Silibeads®, Sigmund Lindner GmbH 400 -500 µm) were used as seed material for the heterogeneous nucleation of celestite and strontianite. Similarly to sand, glass beads are mainly composed of silicon dioxide and can therefore be used as an analogue for natural sand at the laboratory scale. The major advantage of glass beads over natural sand is the almost perfect spherical shape allowing a precise determination of its specific surface area. Knowledge of the latter is in turn necessary for the normalization of nucleation kinetics to the reactive surface area. The composition of glass beads is follow: 72.50% SiO_2, 13.00% Na_2O, 9.06% CaO, 4.22% MgO and 0.58% Al_2O_3. For use as heterogeneous seeding material, the beads were washed with a 2 % nitric acid solution, rinsed with Milli-Q water to neutral pH, and dried at 313 K for a minimum of 8 hours before use. For the preparation of the dissolved silica solution used in this thesis, a suspension of the glass beads in water was kept at 343 K for 24 h to dissolve silica from the beads. The supernatant was then filtered twice through a 0.1 µm cut-off filter. The filtrate was ultra-centrifuged for 2 h at 90000 rpm and 278 K. After ultra-centrifugation, the clear solution was separated again from the eventually decanted residues and analyzed via ICP-OES. The curium solution used in TRLFS experiments was isotopically composed of 89.7 % ^{248}Cm, 9.4 % ^{246}Cm, 0.4 % ^{243}Cm, 0.3 % ^{244}Cm and respectively 0.1 % ^{245}Cm and ^{247}Cm. Accordingly, the europium solution contained only the naturally occurring isotopes ^{151}Eu and ^{153}Eu.

3.2 Methods

3.2.1 The atmospheric CO_2 issue

With the exception of a couple of experiments carried out in the glove box under an argon atmosphere, the majority of experiments in this thesis were carried out at air. To avoid intrusion of carbon dioxide, each 100 ml of stock solutions containing NaCl (5 mol·l^{-1}), $SrCl_2$ (0.6 mol·l^{-1}), Na_2SO_4 (0.3 mol·l^{-1}) and Na_2CO_3 (0.2 mol·l^{-1}), respectively, were prepared under an argon atmosphere using Milli-Q water which was prior degassed by bubbling with argon. The stock solutions were then kept tightly closed for ageing. The corresponding solutions used in LIBD and TRLFS experiments were prepared by diluting an aliquot of the stock solution with fresh Milli-Q water. Even though this preventive

step could not assure total exclusion of CO_2, we will assume in the rest of this thesis the impact of atmospheric carbon dioxide on celestite samples ($5 < pH < 6$) to be negligible. For the strontianite samples, the difference between the pH calculated with PhreeqC assuming $pCO_2 = 0$ and the experimental measured pH values suggest an effective pCO_2 of 10^{-7} to 10^{-5}. This effective pCO_2 is smaller than its atmospheric value ($10^{-3.5}$), attesting that the solutions were not at equilibrium with atmospheric carbon dioxide. Due to the low pCO_2-values determined, the influence of atmospheric CO_2 on the solution speciation can be neglected.

3.2.2 Solution speciation

Supersaturated solutions were prepared by mixing equal volumes of equimolar solutions of Strontium chloride with sodium sulfate or sodium carbonate. The ionic strength was set using sodium chloride and is 0.1 mol·kg^{-1} in all experiments, unless stated differently. The supersaturation ratio (S) with respect to celestite and strontianite was calculated using the geochemical code PhreeqC [166] and the databases thermoddem.dat (for celestite) [154] and wateq4f.dat (for strontianite) [167], respectively, according to the equations (32) and (33):

$$S_{celestite} = \frac{a(Sr^{2+}) * a(SO_4^{2-})}{K_{sp,celestite}} \quad (32)$$

and

$$S_{strontianite} = \frac{a(Sr^{2+}) * a(CO_3^{2-})}{K_{sp,strontianite}} \quad (33)$$

where $K_{sp,celestite} = 10^{-6.63}$ and $K_{sp,strontianite} = 10^{-9.27}$ are the solubility products for celestite and strontianite respectively; $a(Sr^{2+})$, $a(SO_4^{2-})$ and $a(CO_3^{2-})$ are the activities of Sr^{2+}, SO_4^{2-} and CO_3^{2-} ions, respectively.

The speciation diagrams in chapter 4.3 are calculated using the geochemical program HYDRA MEDUSA [168] and the ThermoChimie database [169].

3.2.3 Laser induced breakdown detection (LIBD)

The measurement principle of LIBD is based on the generation of a di-electrical breakdown and counting of the plasma events when the triggered focused laser beam hits a nano-particle suspended in the liquid passing through the laser focal volume. The instrumental setup is represented schematically in Figure 11.

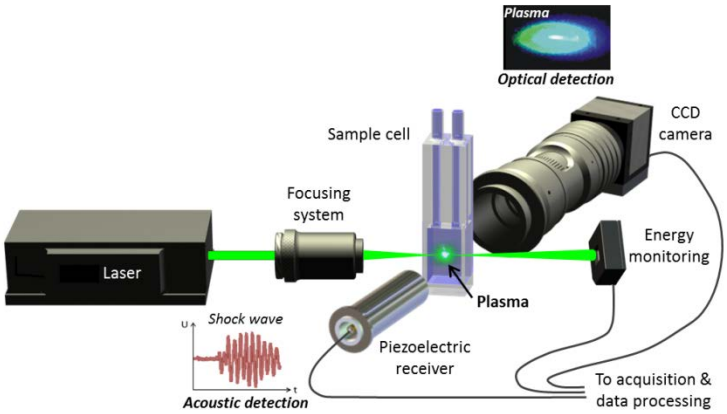

Figure 11. Schematic illustration of an LIBD instrumentation highlighting the different components of the device and the two detection modes. Adapted from: [Source: eHistory. September 9th, 2015. http://www.innovation.kit.edu/img/Setup_LIBD.png]

High energy densities, usually in the order of 10^8 W/cm^2, are required for the generation of a plasma on colloids [170]. The surface power densities and associated high field strengths are generated by focusing a pulsed laser beam in the focal volume of the measurement cuvette. When the laser pulse density exceeds a certain energy threshold, a di-electrical breakdown occurs and subsequently a plasma forms [171]. The breakdown and thus the formation of the plasma occur selectively on the solid particles as the laser power density needed to ignite plasma in solids is lower than in liquids or gases. Furthermore, the laser power density needed to ignite breakdown shows size dependency; smaller particles need a higher power density than larger particles of the same material [172, 173]. The rapid expansion of the plasma creates an acoustic signal that can be analyzed via a piezoelectric receiver in the acoustic mode. Furthermore, light irradiated in the visible wavelength during the plasma recombination can be used in the optical detection modus [174-176], as it was the case in the present thesis. The determination of the induction period using the LIBD method is based on the time resolved evolution of the breakdown probability (BDP), which is defined as the fraction of laser shots that resulted in plasma formation, i.e. the quotient of plasma events detected to total number of laser pulses [177]:

$$\mathrm{BDP} = \frac{(\text{plasma nb.})_i - (\text{plasma nb.})_{i-1}}{(\text{shot nb.})_i - (\text{shot nb.})_{i-1}} \qquad (34)$$

where plasma nb, shot nb and i represent the number of generated plasma, the number of laser pulses and the ith plasma or laser shot, respectively. The increase of the initial BDP with time correlates with the onset of the nucleation.

When the number of breakdown events is plotted against the laser beam axis, the full width at half maximum (w) can be determined by using a Gaussian curve fitting [178]. Average particles size, d, can be calculated from the full width at half maximum according to equation (35).

$$d = \frac{w - 243.15543}{0.70197} + 50 \quad (35)$$

The constants in equation (35) are specific laser parameters determined from the calibration of the LIBD device. The smallest size of commercially available polystyrene particles for device calibration is 20 nm, therefore we cannot provide any reliable information for particles below this size limit. The relationship between the BDP and the particles concentration C (particles per ml) is given by equation (36).

$$\mathrm{C} = \frac{1}{\mathrm{V_{particle}}} * [1 - (1 - \mathrm{BDP})^{\frac{\mathrm{V_{particle}}}{\mathrm{V_{eff}}}}] \quad (36)$$

with $\mathrm{V_{eff}}$ as the effective focus volume of the laser beam and $\mathrm{V_{particle}}$ as the volume of a spherical particle. The effective focal volume ($\mathrm{V_{eff}}$) is a function of the particle diameter and of the laser energy. The smaller the particles, the higher the energy required for a plasma induction, and hence the smaller the effective focal volume. For particles with diameter of 20 – 1000 nm, the effective focal volume is comprised between $2 \cdot 10^{-15}$ – $1 \cdot 10^{-13}$ m^3 [177]. The laser used for the experiments in this thesis was a continuum minilite (Continuum GmbH) Nd:YAG solid state laser with a maximum repetition rate of 15 Hz. The used wavelength of 532 nm was generated by a second harmonic generator (SHG) frequency doubling crystal.

The advantage of the LIBD over other quantification methods is shown in Figure 12. Single particle counting (SPC) can be applied at very low particles number concentrations, but the average minimum particle size of ~ 70 nm limits its application to relatively large colloidal particles only. Light scattering and surface analysis methods can indeed be used to detect small particles, but high particles number concentrations are required. The LIBD is a very powerful tool because it can be used for low particle number concentrations (10^3 particles/ml < [Conc] < 10^9 particles/ml) as well as for a wide range of particle sizes (20 nm < d < 1 µm). In this thesis, supersaturated solutions of strontium sulfate or strontium carbonate were prepared as described above (chapter 3.2.2) and kept in a thermostat at constant temperature, ranging from 278 to 338 K. The solution was continuously pumped into the measurement cuvette and the increase of its colloid concentration as response to the occurrence of nucleation in the solution was measured as a function of time.

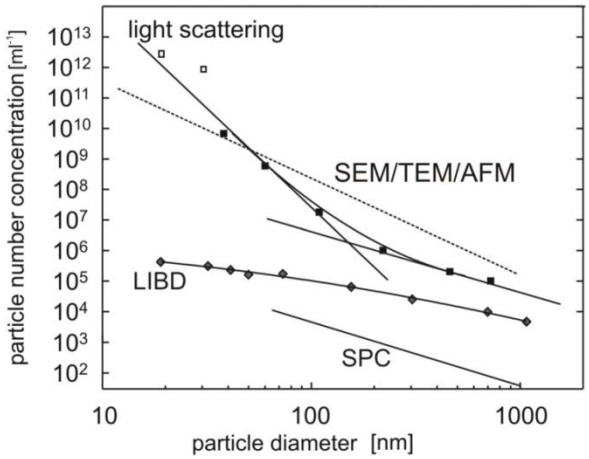

Figure 12: Sensibility of different analytical methods for the quantification of colloids, adapted from Bitea [171]

3.2.4 Mixed flow reactor (MFR) experiments

The kinetics of nucleation and growth of celestite and strontianite, as well as curium and europium co-precipitation with these mineral phases were studied in mixed flow reactors (MFR) experiments. In a MFR, also known as continuously stirred tank reactor [179, 180], seed crystals of the mineral to precipitate are placed into the reactor of a given volume (70 ml), through which fluid is pumped continuously at a constant flow rate (0.6 ml·min^{-1} = 3* 0.2 ml·min^{-1}).

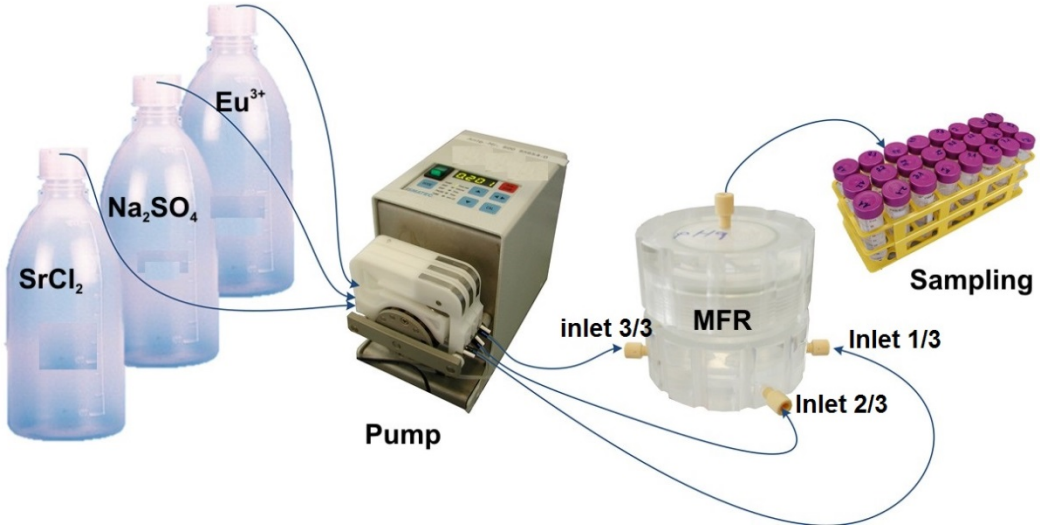

Figure 13. Setup for mixed flow reactor experiments. NaCl with a concentration of 0.1 mol·l^{-1} is used in all solutions as background electrolyte for the adjustment of the ionic strength.

Figure 13 illustrates the experimental setup of a MFR experiment, highlighting the co-precipitation of europium with celestite. Three solutions prepared according to the description in section 3.2.2. containing strontium chloride, sodium sulfate or sodium carbonate and europium or curium, were injected into the 70 ml reactor using an Ismatec® peristaltic pump with a constant flow rate of 0.2 $ml \cdot min^{-1}$ at each inlet, resulting in a total outflow of 0.6 $ml \cdot min^{-1}$. The reactor was made of Plexiglas and equipped with a floating Teflon coated magnetic stirrer operating at 800 rpm. The stirring bar is suspended on a Teflon mount, in order to avoid grinding effects. The homogeneity of concentration and temperature in the reactor are achieved by continuously stirring the reactor volume so that ideal mixing may be assumed. Stirring further keeps the seed crystals suspended in the fluid. Temperature stability is guaranteed by immersion of the reactor in a water bath kept at constant temperature (295 K, unless stated differently). The solution left the reactor through a 0.10 µm Millipore® filter. Figure 14 shows a detailed cross section (left) as well as an image (right) of the dismantled MFR. The experiments were seeded with the same mineral as the one to precipitate. The mass of seed crystals used in each run was between 50 – 250 mg.

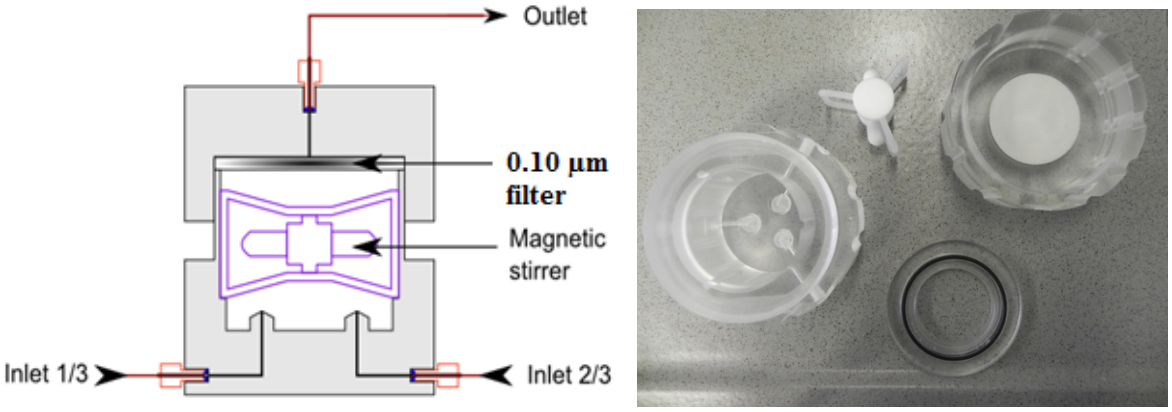

Figure 14. Detailed cross section of the MFR (Left) and picture of the dismantled, Plexiglas made MFR and Teflon coated magnetic stirrer (right)

3.2.5 Measurement of the specific surface area of seed crystals using the Brunauer-Emmett-Teller (BET) method

The determination of the specific surface area by means of the BET theory is based on physical adsorption of gases on the surface of a powder. From an adsorption isotherm measured as a function of gas pressure, the amount of adsorbed gas corresponding to a monomolecular layer at the surface can be calculated. Physisorption results from relatively weak van-der-Waals forces between the adsorbent surface of the test powder and the adsorbate gas molecules. The measurement of surface area is usually carried out at temperature of liquid nitrogen [181]. The specific surface area of

commercially available strontium sulfate and strontium carbonate powders of puratronic grade (Alfa Aesar) used as seed crystals in MFR experiments, was, however measured by Krypton-BET, since the results of N_2-BET measurements were inconsistent. Measurements were performed with a Quantachrome Autosorb Automated Gas Sorption System.

3.2.6 Scanning electron microscopy (SEM)

Sample topography and elemental composition analysis at the microscopic scale were performed using a FEI QUANTA 650 FEG environmental scanning electron microscope (ESEM), equipped with a field emission electron gun (FEG, max. electron energy 30 keV), secondary electron detectors (SED), backscattered electron detector (BSED), and a Peltier-cooled energy-dispersive X-ray detector (EDX, UltraDry silicon drift X-ray detector, Thermo Scientific NORAN System 7) for elemental analyses. Powder samples were pasted on double-sided conductive tape attached to a standard aluminum holder. Sample measurements were either performed using a low energy electron beam in high vacuum (typical. 2-5 keV) for topography analysis or at higher energy (20 - 30 keV) for elemental analysis by EDX using either conductively coated samples (chromium or carbon) or the variable pressure mode of the microscope with 70 mPa of water vapor pressure inside the analysis chamber.

3.2.7 Transmission electron microscopy (TEM)

In TEM, a material of interest is irradiated by highly accelerated electrons with up to a few hundred keV. Penetrating through the specimen, the accelerated electrons can be scattered by electrons or nuclei in the sample. Elastically scattered electrons provide mainly structural information of the material. This information is extracted by analyzing the electron diffraction pattern and the corresponding TEM image. The electron diffraction pattern further provides information about the crystal lattice of the investigated material via the intersections of the reciprocal lattice of a crystalline sample with the Ewald’s sphere. In high resolution TEM (HR-TEM), images magnification is high enough that the crystal lattice intervals can be directly determined from the lines of the lattice fringes (down to 0.2 nm at 200kV). Thus, HR-TEM is capable of imaging samples of interest at significantly higher resolutions than optical microscopes, because the wavelength of accelerated electrons is much shorter than that of light.

Figure 15 shows a scanning TEM. The picture on the left shows a TEM device, and the picture on the right highlights the main components of a TEM device, these are:

- The gun which produces electrons
- The condenser system which forms the probe

- The specimen which should be very thin to allow electrons transmission
- The objective lens on which the image is formed
- A fluorescence screen on which the image is projected (magnification).

In a TEM the electron beam is focused on the sample using the condenser lens system. This produces an image which is focused by the objective lens to a point. This image is then magnified by a series of projector lenses to vary the size of the image on a fluorescent screen. Changing the current of an electromagnetic lens alters its focal length altering magnification.

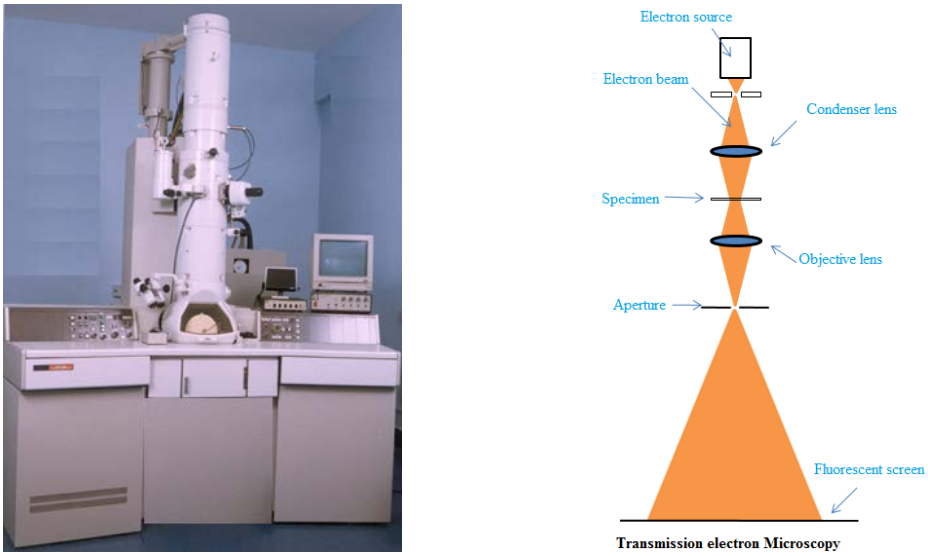

Figure 15: Overview of a TEM device (left) and the selected components necessary for the imaging of a specimen (right) [adapted from eHistory. September 21th, 2015. http://www.cma.tcd.ie/misc/tem.pptx]

For TEM experiments, supersaturated solutions of strontium sulfate (S = 12.59) and strontium carbonate (S = 19.95) were prepared as described above. At time intervals of 75 s, 30 min and 2 h respectively, an aliquot of 100 µl was transferred into lower concentration environments by mixing it with 1.9 ml NaCl (0.1 $mol \cdot l^{-1}$) in order to quench nucleation and to check the stability of formed clusters. The quenching with 0.1 $mol \cdot l^{-1}$ NaCl assumes an exclusion of modifications of ESN due to the change in ionic strength, or ionic strength dependent dissolution of ESN during this procedure. Few drops of the resulting sample were put on a carbon coated copper grid, the supernatant was removed and the thin film remaining on the grid surface was dried at room temperature. The sample was then mounted on a sample holder and transferred into the high vacuum measurement chamber of the TEM device.

3.2.8 Time resolved laser induced fluorescence spectroscopy (TRLFS)

Two different laser systems (Figure 16) were used for the TRLFS measurements in this study. The laser system I was used for measurements at room temperature, while the laser system II was equipped with a cryostat and used for low temperature (T < 10 K) measurements.

The laser system I is composed of a Nd:YAG laser (Continuum Surelite laser), a dye laser (NARROW$_{SCAN}$ D-R Dye laser) and the detection system. The Nd:YAG laser is used to pump the dye laser. The excitation of the Neodymium doted yttrium aluminum garnet is assured by a flash bulb operating with a frequency of 10 Hz. After a frequency trebling on the non-linear crystals, the laser emits light with a wavelength λ = 355 nm. The latter is used to pump the dye laser. The medium in the dye laser is a solution of the Exalite 398 dye in dioxane, allowing a maximum efficiency of 20 % (398 nm) in the wavelength range between 391 and 404 nm. The measurement cuvette is placed in a holder connected to a thermostat in order to maintain constant temperature during the measurement. A quartz fiber placed in an angle of 90° with respect to the incident beam, is used to conduct the fluorescence light to a spectrograph (Shamrock 303i, ANDOR) equipped with grids of 300, 900 or 1200 lines/mm. The latter are used for the spectral decomposition of the fluorescence spectrum. The spectral resolution increases with the increasing grating, but the active window in terms of the nm range decreases. An ICCD camera (iStar Gen III, A-DH 720 18F-63 ANDOR) equipped with a digital delay generator is used for the detection of the fluorescence signal. The spectra are recorded with a time delay of 1 µs in order to suppress short-lived fluorescence phenomena.

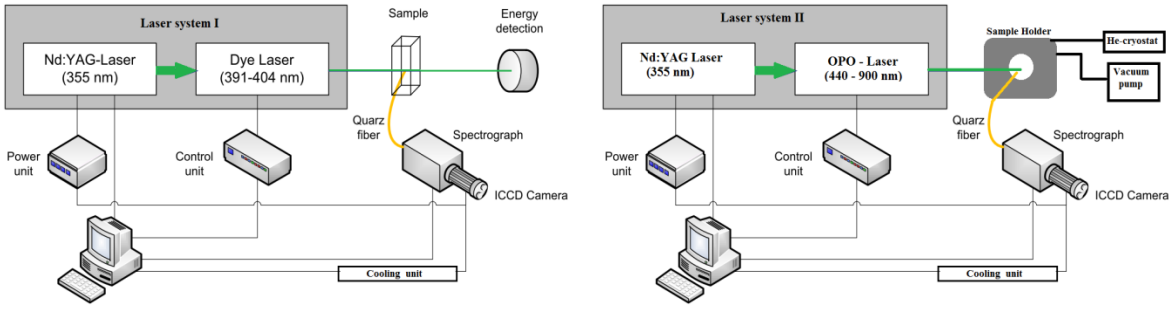

Figure 16: Scheme of the TRLFS system I (left) and system II (right) for measurements at room temperature and at low temperature (~ 6 K), respectively.

TRLFS measurements at low temperature are carried out on the laser system II, which differs from the system I mostly as follow: i) the dye laser in system I is replaced by an OPO laser system (*Optical Parametric Oscillator*, Quanta-Ray Pro Series) emitting in the wavelength range from 440 to 900

nm; ii) the angle between the sample and the incident light is 45° and the quartz fiber for coupling out the fluorescence signal is placed above the sample; iii) the sample is placed in a sample holder maintained in ultra-high vacuum and is cooled down to about 6 K using a Helium cryostat (CTI-Cryogenics).

Liquids samples for TRLFS were prepared directly in a quartz cuvette. The cuvette was then closed using a Teflon stopper in order to prevent further intrusion of air. Powder samples were also filled into a quartz cuvette (room temperature measurement), or mounted on a sample holder made of copper for low temperature measurements.

4 Results and discussion

The main results of this thesis are grouped in three main sub-chapters: The induction periods determined in LIBD experiments are summarized in sub-chapter 4.1, followed by the determination of crystal growth rates in MFR experiments (sub-chapter 4.2). The third sub-chapter summarizes the TRLFS studies on the uptake of Eu(III) and Cm(III) during the nucleation and crystal growth of celestite and strontianite.

4.1 Determination of induction times in LIBD-experiments

This part of the thesis presents the results of LIDB experiments, especially the determination of the induction period for the nucleation of celestite and strontianite as a function of different reaction variables (supersaturation, temperature, ionic strength, additives).

4.1.1 Induction times for the nucleation of $SrSO_4$ and $SrCO_3$

Prior to the appearance of crystals in a supersaturated homogeneous liquid system, i.e. an event signalizing the end of the induction period, subcritical particles must be formed and grow to detectable sizes. The determination of the induction period t_{Ind} is strongly influenced by the measurement method. Different measurement methods reported in the literature are, among others, the spectrophotometric measurement of the attenuation of light intensity [182], the pH -drift monitoring [89], the temperature-time profile variation [183], the observation of turbidity in solution [162], the change in conductivity etc. Most of the induction periods reported in the literature are a sum of nucleation time (t_n) and growth time (t_g) of nuclei to detectable sizes. The contribution of t_g to the overall induction period is assumed to be very low or even negligible in the LIBD method, thanks to the sensitivity of LIBD to detect very small particles.

4.1.2 Influence of solution impurities

LIBD is a very sensitive detection method and therefore, some experimental precautions are necessary prior to measurement to avoid a high background concentration of nanoparticles/colloids. The reduction of the amount of impurities in the solutions was achieved by processes such as triple recrystallization of salts, ageing of the stock solutions for several months, ultracentrifugation and choice of an appropriate reaction vessel. Yun et al. [66] have also reported the recrystallization of NaCl to be an effective method for the purification from colloidal impurities. The impact of these processes on the breakdown probability (BDP) is shown in Figure 17. The colloid particle number concentration was calculated from the BDP using equation (36). A solution of sodium chloride prepared from the commercial salt without further purification contains approximately $8.1 \cdot 10^7$ particles$\cdot$ml^{-1}, while this concentration can be lowered down to approx. $2.6 \cdot 10^7$ particles$\cdot$ml^{-1} by

means of recrystallization. Similarly, the colloid concentration of a solution stored in a glass vessel increases with time as response to the release of silica-nanoparticles from the vessel walls into the solution. A slight increase of the colloid concentration is observed after only 2 days of storage in the glass vessel. For this reason, solutions for LIBD were prepared and stored in high density polyethylene (HDPE) bottles, since the HDPE material seems to be inert regarding release of nanoparticles to solution. The ageing effect on the BDP decrease can be explained in two ways:

1) The impurities of the salt solutions exist as colloidal material at the moment of dissolution. Because these impurities have a great affinity for water, they will become successively hydrated concomitant with a decrease in density over time and therefore less distinguishable from water, resulting in the decrease of the BDP. The hydration tendency of substances depends upon their water affinity, controlled by the intermolecular interactions (hydrogen bonding, ion-dipole, and dipole-dipole attractions, van-der-Waals forces) which make substances dissolve in water [184].
2) The second hypothesis suggests the sorption of the existing colloids on the storage vessel walls, resulting again in a decrease of the BDP with time.

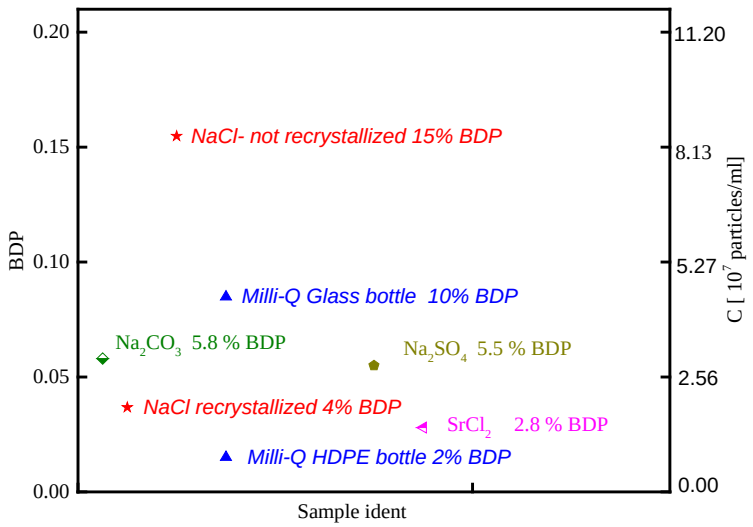

Figure 17. Dependency of the BDP on the degree of purity of reactants, and the type of storage vessel. The particle number concentration, expressed in number of particles per unit volume (Y-axis on the right), is calculated assuming the average particle size to be 20 nm, and the particles to have a spherical shape.

4.1.3 LIBD observations during nucleation of celestite and strontianite

Typical evolutions of the average particle concentration and average colloid size with time during nucleation and growth are shown for both celestite (Figure 18) and strontianite (Figure 19). The blue dashed horizontal line indicates the calibration limit of the LIBD-device concerning colloidal sizes. The smallest size of commercially available polystyrene standard particles (NanosphereTM Standards,Thermo Scientific) for size calibration is 20 nm. Therefore, we cannot provide any reliable information about the size of particles below this calibration limit.

The mixing of the respective aqueous solutions (e.g. $SrCl_2$ and Na_2SO_4 or Na_2CO_3) is always accompanied with an increase of the BDP, which occurs immediately after mixing. This indicates the formation of the first nuclei in the crystallization processes of celestite and strontianite to occur immediately after the supersaturation is established. These first nuclei formed with the creation of supersaturation will be referred to in this thesis as “early stage nuclei” (ESN).

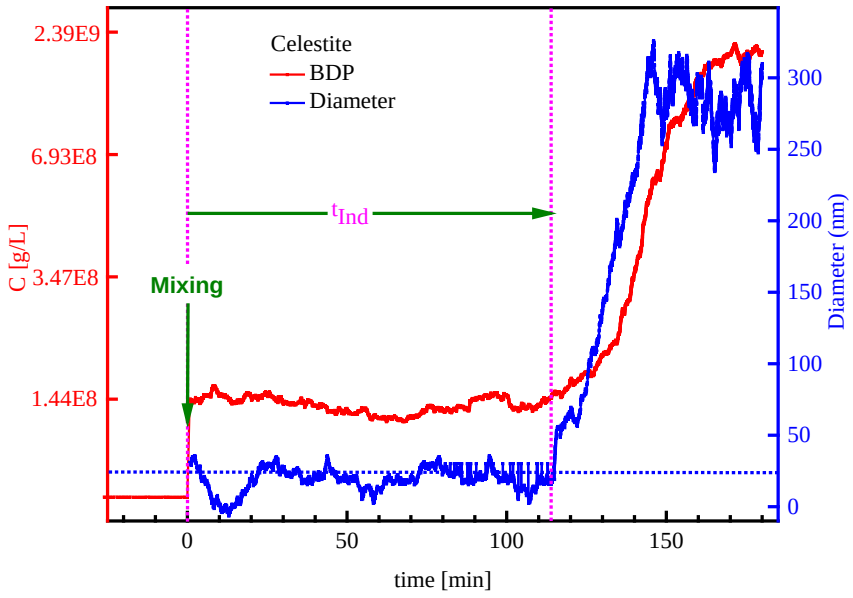

Figure 18. Evolution of the particle concentration (red line) and average particle size (blue line) during the homogeneous nucleation of celestite at an initial supersaturation ratio of S = 7. For the calculation of the particles concentration, the particles were assumed to be spherical and to have an average diameter of 20 nm. The induction time ends when the average size of the particles starts to increase considerably.

The average concentration of colloids in ultraclean water (Milli-Q, Millipore) determined by LIBD is approx. $1 \cdot 10^7$ particle/ml (0.1 ppb). The colloid concentration of the solutions used in this thesis

increased from approx. 0.3 ppb before mixing (e.g. mixing of strontium chloride and sodium sulfate solutions in order to create a solution supersaturated with respect to strontium sulfate) to approx. 4.5 ppb straight after mixing, indicating that the formation of early stage nuclei (ESN) occurs almost simultaneously with the creation of supersaturation. In the celestite system, the appearance of ESN is followed by a time frame known as induction time t_{Ind}, during which the changes in the number of nuclei as well as their particles size are negligible. As soon as the radius of the particles reaches the critical size, a considerable increase of the particle concentration towards a plateau is observed. This increase of the particles concentration occurs simultaneously with the increase of the average particle size, indicating the end of the induction time. The average celestite particle size is usually between 250 – 350 nm directly at the end of the induction period. However, storage of the solution for several days (> 10 days) allows the crystals to growth to sizes of about 10 µm ($S \leq 31$) or to much larger crystals ($S \geq 100$). At $S \leq 31$, the amount of strontium and sulfate ions remaining in solution after the nucleation is too little to sustain crystal growth to larger sizes.

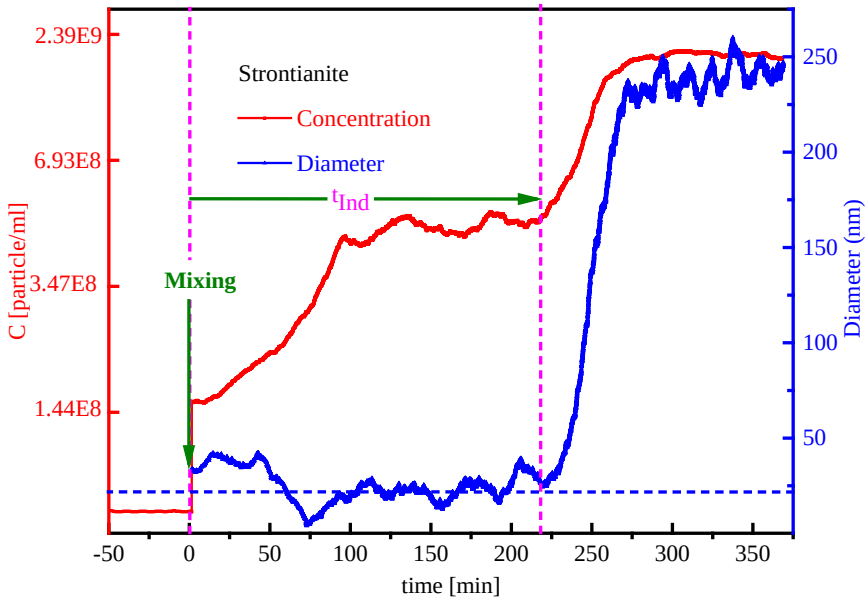

Figure 19. Evolution of the particle concentration (red line) and average particle size (blue line) during the homogeneous nucleation of strontianite at an initial supersaturation ratio of S = 12.6. The induction time ends when the particles start to growth. For the calculation of the particles concentration, the particles were assumed to be spherical and to have an average diameter of 20 nm.

The nucleation and growth of strontianite from supersaturated solutions is similar to that of celestite, with the exception that the number of early stage nuclei (particle number concentration) increases slowly with time to reach a first quasi-plateau. During this first step, the average particle size remains

almost constant. The subsequent increase of the particle concentration is accompanied with an increase of the average particles size, as in the case of celestite, thus indicating the end of the induction time. For the majority of experiments at supersaturation S < 31.6, the average strontianite particle size obtained after nucleation was around 250 nm and further growth of the crystals was not observed. An increase of the supersaturation to approx. S = 1000 was necessary to induce further crystal growth to micron sizes. To summarize, the relaxation time t_r necessary to achieve a quasi-steady-state of distribution of molecular clusters seems to be within fraction of seconds as expected for solutions with low viscosity (e.g. aqueous solutions), since early stage nuclei detected by LIBD appear simultaneously with the mixing of the solutions and hence the creation of supersaturation (t = 0 min). Let's assume that the growth of early stage nuclei to critical sizes is achieved by consumption of smaller nuclei or by agglomeration. For the case that the number of ESN remains constant over the time, the BDP will decrease (as the average particle size increases) initially as response to the decreasing number of nuclei. This behavior is not observed during the induction time, supporting either the hypothesis of growth by single attachment of solute molecules to the growth unit, or suggesting the number of newly formed ESN to be of the same order as the number of ESN consumed in the process of growth. Further, the average size of early stage nuclei lies below the calibration limit of the LIBD-system making the exact determination of the critical nuclei size impossible.

4.1.4 Transmission electron microscopy (TEM) experiments

In order to gain additional information relative to the crystallinity of the "early stage nuclei" (ESN) observed in LIBD during homogeneous nucleation experiments, solutions supersaturated with respect to celestite and strontianite were prepared and the nucleation process was followed using a TEM device. The induction time of the celestite sample with supersaturation S = 7 was predetermined in LIBD experiments to be 114 ± 1 min (Annex 6). Results of the TEM imaging are shown in Figure 20. The concentration of ESN has been estimated in chapter 4.1.3 to be approx. 4.5 ppb. As comparison, the particles concentration after the occurrence of nucleation is approx. 16 times higher. Therefore, the formation of ESN cannot be interpreted as indicating the end of the induction period. It is important to note that the images in Figure 20 do not show the evolution of the same particle with time. A different aliquot of the same sample was used for each TEM image. Therefore, the images above rather represent a statistical evolution of nuclei with time.

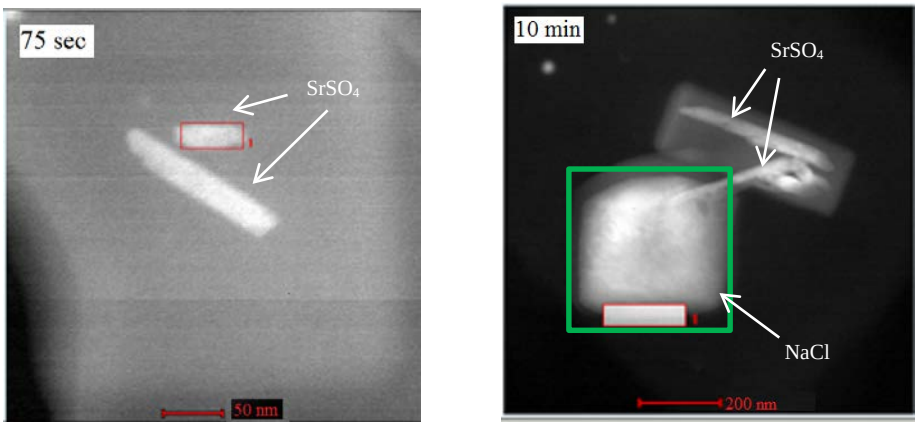

Figure 20. TEM images showing clearly that ESN formed during the nucleation of celestite are crystalline. The images are taken at 75 sec and 10 min, and thus at t << t_{Ind}. The square-like bright spot (see green square) on the TEM image after 10 min is a NaCl artefact, as confirmed by elemental analysis (Annex 5). The marked areas (red rectangles) represent the areas selected for elemental analysis. The bright shadow around the particles on the right pictures results from the sample contamination by the electron beam.

TEM results show the formation of well-shaped rod-like crystals after only 75 sec of reaction time (t_{Ind} = 114 min). The average size of these crystals varies slightly between 75 sec and 10 min of reaction time. Additional information supporting the formation of celestite is provided by the high resolution TEM and the Fast Fourier Transform (Figure 21), both showing the existence of lattice fringes and periodicity, respectively. The (001) crystallographic planes are also observed, which is typical for celestite, resulting in the needle shape. The HRTEM image taken from the two needle shaped particles show that the ESN of celestite are well crystalline. The particle width of ~ 20 nm fit very well with the LIBD observations, which predicts the average nuclei size to be 25 ± 20 nm. However, the length of the crystallites (50 – 100 nm) is twice as big as the average size assuming spherical geometry determined by LIBD. Discrepancy between TEM and LIBD might arise specifically from this assumption of LIBD, which considers a spherical shape for the nuclei based on the calibration with latex microsphere. The average radius of gyration ($\bar{R}_g$) of the particles is estimated to be 29 ± 10 nm according to the following equation[185].

$$\bar{R}_g = \left(\frac{3}{5}\right)^{1/2} \frac{D_h}{2}$$

where D_h represents the hydrodynamic diameter of the non-spherical particles. Both the average particle size determined by the LIBD-method and by the calculation of the gyration radius based on

the TEM shape analysis are in good agreement. The concentration of nanoparticles in solution at the early stage of nucleation (4.5 ppb) is approx. 16 times lower than the concentration of nanoparticles in solution after the elapse of the induction time. According to TEM observations, no amorphous intermediates are involved in the crystallization of celestite.

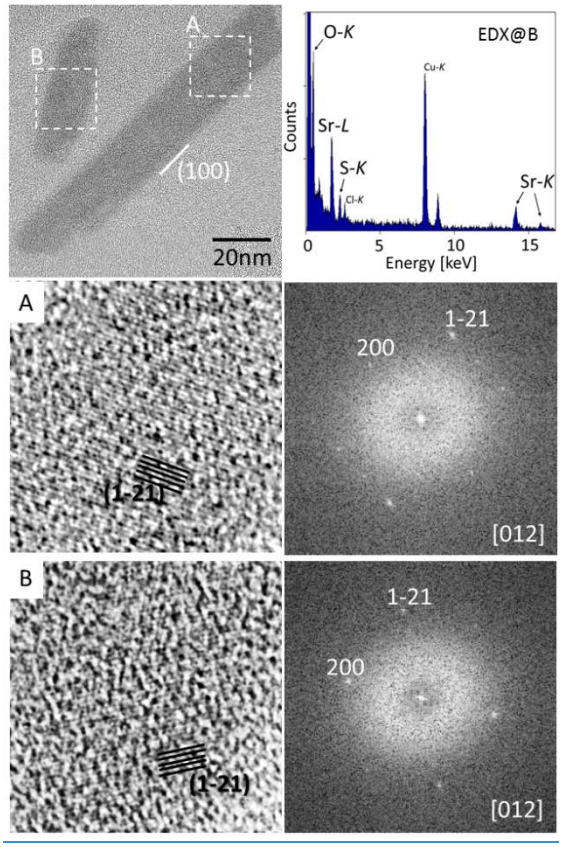

Figure 21. High resolution TEM (HRTEM) and fast Fourier transform (FFT) of the ESN of celestite after a reaction time of 75 sec. The HRTEM image shows the lattice fringes as evidence of crystallinity corresponding to celestite which is also supported by the EDX spectrum. The periodicity of the elemental cells shown by FFT supports the existence of lattice fringes.

A similar experiment was carried out for strontianite at supersaturation S = 20. In this case, all efforts to visualize ESN using TEM were unsuccessful. Therefore, we suggest that the ESN in the case of strontianite are less stable, and re-dissolve during the quenching process. In-situ TEM experiments would be a more appropriate technique to investigate the nucleation of strontianite. This was unfortunately not possible in the present study.

4.1.5 Effect of supersaturation

The induction times (t_{Ind}) for the nucleation of celestite and strontianite as a function of the supersaturation ratio was investigated at 295 K and ionic strength of 0.1 mol·kg^{-1} NaCl. The relation between ln(t_{Ind}) and (ln S)$^{-2}$ is represented in Figure 22. The corresponding numerical data (average of at least three measurements) are given in Annex 6 and Annex 7.

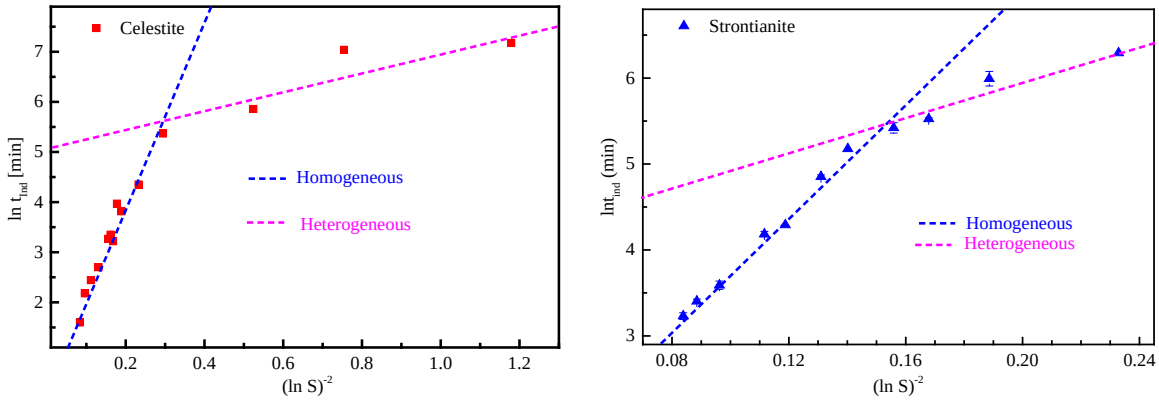

Figure 22. Plot of the logarithm of the induction time before the onset of crystallization of celestite (left) and strontianite (right) as a function of (ln S)$^{-2}$ at 297 K. The ionic strength of the solutions is set at 0.1 mol·kg^{-1} using NaCl.

As may be seen from the two plots in Figure 22, the induction time decreased with increasing supersaturation. It should be noted that the metal concentrations and the supersaturation reported here describe the system before nucleation, while the pH are calculated using the computer code PhreeqC for the precipitated mineral in equilibrium with the supernatant. The maximum recording time in LIBD experiments of 40 hours was chosen with respect to the time interval where the laser pulse energy remains stable. The critical supersaturation ratio S_{crit} for nucleation is the maximum supersaturation that a metastable supersaturated solution can endure without nucleating a detectable amount of thermodynamically more stable new phase (within the here chosen maximum observation period of 40 h). The critical saturation ratio was determined to be:

- S_{crit} = 2.0 for celestite
- S_{crit} = 6.3 for strontianite

The value of S_{crit} is of both academic and technological interest because experimental data for it contain information about important parameters of the nucleation kinetics, and because it quantifies the metastable zone width, which is often used as a criterion in designing industrial processes [186]. Of course, the critical supersaturation ratio depends on temperature, and tends to increase with

decreasing temperature for exothermic reactions [187]. Two linear regression lines with different slopes can be fitted through the experimental data determined for the crystallization of celestite and strontianite (Figure 22). The change of slope corresponds to the crossover between homogeneous and heterogeneous nucleation [188]. The slope of the fitting lines in the lower $\ln(S)^{-2}$ regions, where homogeneous nucleation prevails, gives values of ~ 17 and ~ 32 for celestite and strontianite, respectively, which correspond to interfacial tensions of $\gamma_{celestite} = 22.6 \pm 0.4$ mJ·m^{-2} ($R^2 = 0.97$) and $\gamma_{strontianite} = 31.5 \pm 0.5$ mJ·m^{-2} ($R^2 = 0.98$), according to equation (16). Previously published experimental data for the homogeneous nucleation of celestite from supersaturated solutions show that the interfacial tension decreases with decreasing supersaturation. Compilation of some values reported in the literature for celestite is depicted in Table 6 and Figure 23.

Table 6. Comparison of the estimated interfacial tensions of celestite at 298 K as a function of the supersaturation ratio range.

Log S	γ [mJ · m^{-2}]	IS [mol·kg^{-1}]	Reference
3.4 – 3.9	85	< 0.15	[189]
2.2 – 2.7	76	< 0.15	[161]
1.3 – 2.1	43	< 0.15	[161]
0.8 – 1.5	26	= 0.10	This thesis

Extrapolation of the data determined in this study to higher supersaturation ranges yields reasonable agreement (Figure 23). Furthermore, the data obtained in this thesis on celestite expands those found in the literature to significantly lower supersaturations. The interfacial tensions reported here are usually almost constant for those supersaturation ranges showing a linear dependence of $\ln(S)^{-2}$ versus $\ln(t_{ind})$. The differences observed may be related to the different crystal morphologies, or they may be related to the supersaturation range (different supersaturation ranges in different studies) where homogeneous nucleation prevails. The LIBD method suggests that homogeneous nucleation occurs at a much lower supersaturation range as those reported in the literature (Table 6).

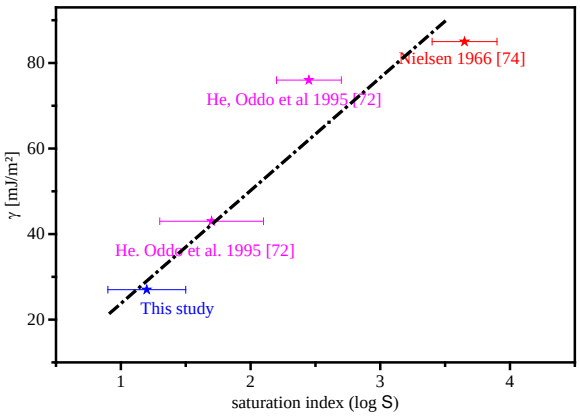

Figure 23. Interfacial tension for the homogeneous nucleation of celestite at 298 K as a function of supersaturation.

The SEM pictures of celestite (Figure 24) show a strong dependence on the supersaturation. The initial supersaturation ratio of the samples on Figure 24 was 12.6 and 100 for the left and right pictures, respectively.

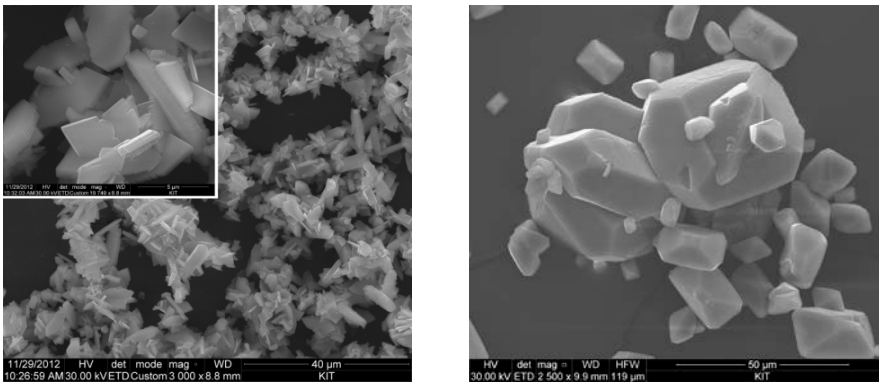

Figure 24. Morphology of the celestite crystals as a function of the supersaturation ratio at ionic strength of 0.1 mol·kg^{-1} NaCl. S = 12.6 (left) and S = 100 (right). The precipitates were kept for 3 days at 298 K in order to allow crystals to growth to a larger size. NB: the scale bar on the pictures are 40 µm (left) and 50 µm (right)

At S = 12.6, the crystals have a plate-like morphology (see the zoom in on the upper left corner of the SEM image), with the average size ranging from few microns up to about 10 microns. At S = 100, the crystals show a typical orthorhombic-dipyramidal structure. It is known that nucleation is accompanied with the desupersaturation of the solution, and subsequent growth occurs via the attachment of the solute molecules remaining in the solution to the nuclei/crystallites, or via Ostwald

ripening. At S = 12.6, the amount of solute molecules remaining in the solution after nucleation is not high enough to support subsequent crystal growth, while the subsequent crystal growth is possible at S = 100 as the degree of desupersaturation due to the nucleation process is relatively low.

4.1.6 Effect of temperature

Temperature plays an important role in crystallization processes. As it affects the solubility of minerals, it has a direct impact on the supersaturation. One advantage of temperature is that it provides precise, and rapid control of relative supersaturation. The use of temperature in addition to standard crystallization variables (concentration, reagent composition, and pH) can increase the probability of producing crystals as well as uncover new crystallization conditions for a sample, since temperature can have an influence on the crystal morphology. To investigate the effect of temperature on the induction time for the crystallization of celestite and strontianite, experiments were carried out at selected temperatures keeping constant the initial solute concentrations. The experimental conditions and numerical results are reported in Annex 8 and Annex 9 for celestite and strontianite, respectively. The negative logarithms of the solubility product ($\log k$-values) of celestite and strontianite given in Annex 8 and Annex 9 were calculated based on the theory given in Reardon et al. [190] and Busenberg et al. [164].

According to the law of mass action, the $\log k$ value (with k being the solubility product) of each mineral depends on temperature. The log k-values for the celestite solutions show that the solubility of celestite varies only slightly within the investigated temperature range, showing a minimum at 295 K (lowest log k-values). Consequently, the saturation ratios with respect to celestite remain almost constant within this temperature range ($\log S_{celestite} = 1.03 \pm 0.02$). Similar observations are made for the temperature dependence of log k of strontianite. However, the pH of the strontianite solutions and thus the supersaturation ratios are strongly dependent on temperature. The variation of saturation indexes (log S) as a function of temperature is shown in Figure 25 for both celestite and strontianite.

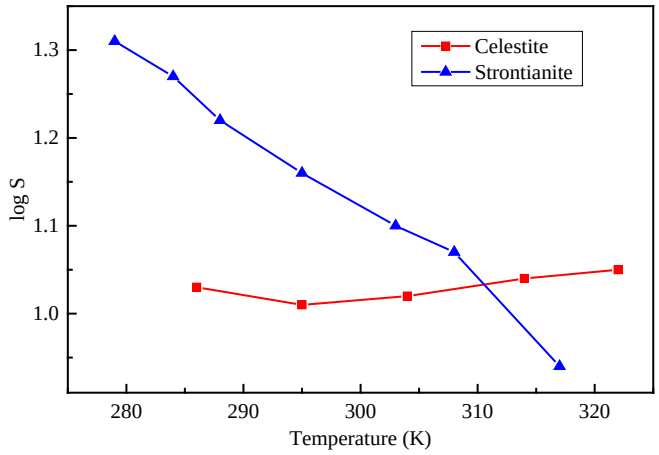

Figure 25. Temperature dependency of saturation index (Ω = log S) at constant initial concentrations of strontium and carbonate or sulfate ions.

As can be seen from Figure 25, the procedure mentioned in chapter 3.2.2 to avoid intrusion of carbon dioxide is not 100 % effective. Following CO_2 dissolution, a small portion of it reacts to form carbonic acid. The equilibrium of carbonates containing solutions can be expresses as follows:

$$H_2CO_3 \rightleftharpoons H^+ + HCO_3^- \rightleftharpoons 2H^+ + CO_3^{2-} \quad (37)$$

What in general is referred to as dissolved inorganic carbon (DIC) consist mostly of the hydrated CO_2(aq), together with carbonic acid, bicarbonate anion and carbonate [191].

In general, when the initial solute concentration is kept constant, a temperature increase substantially decreases the length of the induction period, thus increasing the nucleation rate as expected from the classical nucleation theory. An empirical relationship for the effect of temperature on nucleation kinetics, which is similar to the Arrhenius equation [192] for the temperature dependency of the rate constant was suggested:

$$\log\frac{1}{t_{Ind}} = A - \frac{E_a}{2.303 \cdot RT} \quad (38)$$

where E_a is the activation energy for nucleation and A is a constant. The linear relationship between $\log\frac{1}{t_{Ind}}$ and 1/T is shown in Figure 26 in an Arrhenius plot. The activation energy was calculated from the slopes of the fitting lines of Figure 26 to be 45.5 ± 1.8 kJ·mol^{-1} for celestite and 55.2 ± 3.6 kJ·mol^{-1} for strontianite. Activation energy of 53.7 kJ mol^{-1} has been reported for the homogeneous nucleation of celestite in 1 mol·kg^{-1} NaCl solutions [161]; this value is about 10 kJ·mol^{-1} greater than the value determined in this thesis. Dove et al. [192] have reported an activation energy of 28 ± 2 kJ·mol^{-}

[1] for the dissolution of celestite in pure water over the temperature range of 298 – 363 K. The difference in the values of the activation energy may be related to the different ionic strengths at which the experiments were carried out (0.1 mol·kg^{-1} in this thesis vs 0 or 1 mol·kg^{-1}in the literature), as well as to the method of investigation (precipitation in this study vs. dissolution in [192]).

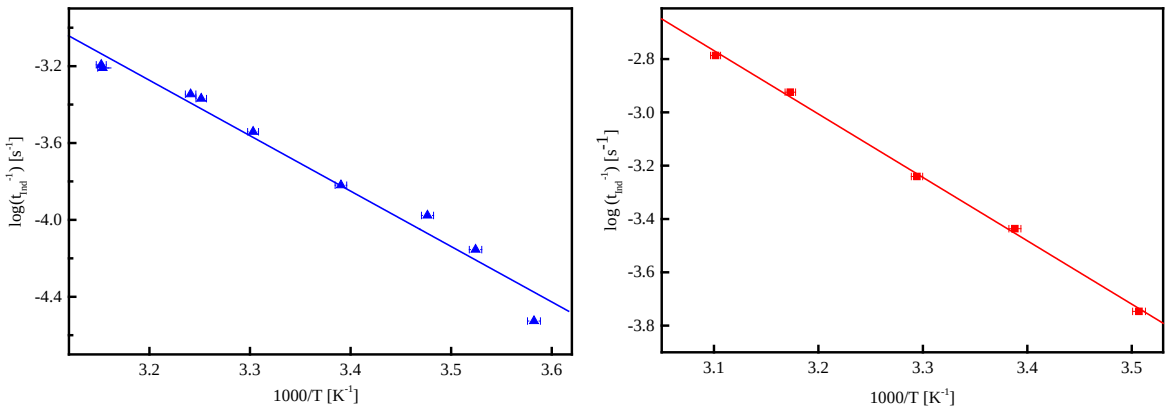

Figure 26. Induction time for nucleation of strontianite (left) and celestite (right) showed in an Arrhenius-like plot. The initial Sr^{2+} concentration is equal to the initial sulfate ($5.83 \cdot 10^{-3}$ mol·l^{-1}) or carbonate ($3.83 \cdot 10^{-4}$ mol·l^{-1}) concentrations. The activation energy can be estimated from the slope of the plotted data according to equation (38).

The impact of temperature on the morphology of the precipitates was investigated using solutions with supersaturation ratio up to 100 and 1000 (at 298 K) for celestite and strontianite, respectively. At supersaturation ratio below 31.6, no isolable precipitates were observed after the nucleation of strontianite. The individual solutions were mixed in a thermostat at the corresponding temperature and kept at the same temperature for three days, in order to avoid the impact of temperature drift on the crystal growth process. Figure 27 shows SEM images of strontianite grown at different temperatures. At 278 K, the crystals are all agglomerated and no well-defined orientation is observed. With the temperature increasing from 298 to 338 K, crystallites agglomerate to form rod-like aggregates. SEM images of celestite crystals grown at different temperatures are shown in Figure 28. The euhedral crystals show the typical orthorhombic dipyramidal morphology reported for celestite. The habit of the crystal at 278 K indicates that attachment of growth units to the crystal occurs selectively on certain crystal faces. The change of the final crystals morphology with increasing temperatures indicates that the relative growth rates of the various crystal faces vary with temperature.

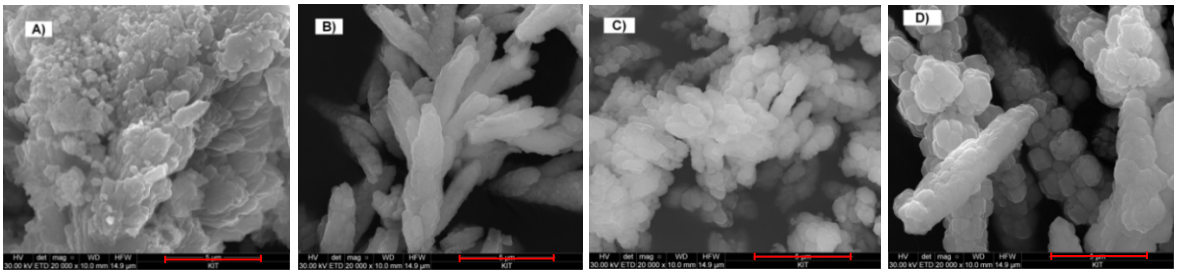

Figure 27. SEM of strontianite as a function of temperature: A) 278 K; B) 298 K; C) 318 K; D) 338. The initial solute concentration was $[Sr^{2+}] = [CO_3^{2-}]$ = 4.4 mM, corresponding to a supersaturation ratio S = 1000 at 298 K (scale bar A – D = 5 µm) (larger picture in Annex 23).

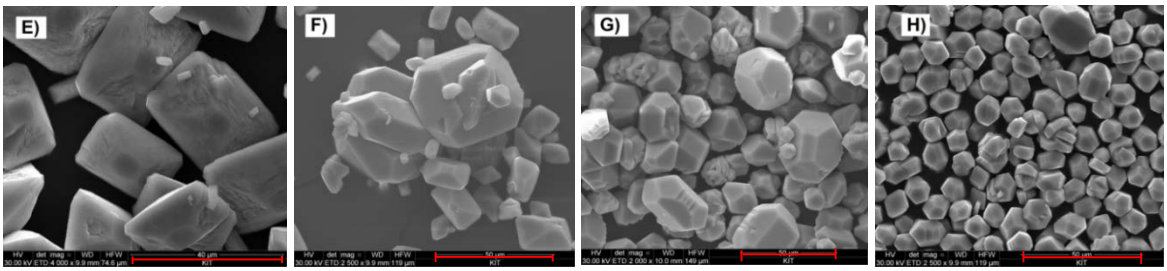

Figure 28. SEM of celestite precipitated at different temperatures: E) 278 K; F) 298 K; G) 318 K; H) 338. The initial solute concentration was $[Sr^{2+}] = [SO_4^{2-}]$ = 25.2 mM, corresponding to a supersaturation ratio S = 100 at 298 K (scale bar E = 40 µm; F – H = 50 µm) (larger pictures in Annex 24).

In sum, the observations made in this thesis suggest that nucleation is followed by agglomeration of the crystals in the case of strontianite, while the nucleation of celestite is followed by crystal growth. The average size of the celestite crystals decreases with increasing temperature, ranging from approx. 35 µm at 278 K to approx. 15 µm at 338 K. This indicates that the crystals with smaller size become more stable as the temperature increases. For the strontianite crystals, the agglomerate at 278 K is more lump-like with an average size greater than 10 µm, while more rod-like agglomerates are observed with increasing temperature, reaching an average width of ~ 3 µm and length of 10 µm at 338 K.

4.1.7 Effect of ionic strength

The effect of ionic strength (I) on the nucleation kinetics was investigated between $0.001 \leq I \leq 1$ mol·kg^{-1} in two different ways: For the celestite nucleation, the solute concentration was varied with the concentration of background electrolyte, while keeping the activity and hence the supersaturation

ratio of the solution constant. For strontianite nucleation, the solute concentration was kept constant while increasing the concentration of the background electrolytes, which resulted in a slight decrease of the supersaturation. Results are summarized in Annex 12 and Annex 13. The corresponding plots are shown in Figure 29 and Figure 31 for celestite and strontianite, respectively.

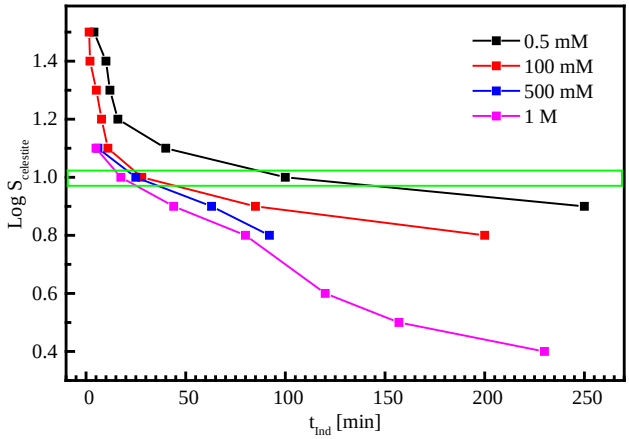

Figure 29. Induction time of celestite as a function of the ionic strength. To maintain constant supersaturation ratio, the solute concentration is increased with increasing ionic strength. The green horizontal lines on the plot highlights the effect of ionic strength at a constant supersaturation index (Log S = 1.0): the induction period decreases when the ionic strength of the solution increases.

Figure 29 shows that at constant supersaturation (green rectangle on the graph, Log S = 1.0), the induction time markedly decreases with the increasing concentration of the background electrolyte. Increasing the ionic strength while maintaining constant the solute concentration would lead to a decrease of the mean activity coefficient of the ions. For this reason, the solute concentration was increased together with the ionic strength in order to keep constant the mean activity coefficient of the aqueous Sr^{2+} and SO_4^{2-}(see Annex 11). The increase of the background electrolyte concentration directly induces an increase of the impurities in the solution. These impurities can further promote nucleation, resulting in a decrease of the induction times. He et al. [161] have found that with increasing ionic strength the interfacial energy between the solid surface and the fluid decreases. The decrease of induction time may also be related to the decreased interfacial tension. AFM studies have also shown that the presence of background electrolytes reduces the interfacial tension and also causes an increase of the kinks density on a growing surface [193]. SEM pictures (Figure 30) show that the increase of the ionic strength further seems to impact the morphology of the crystals.

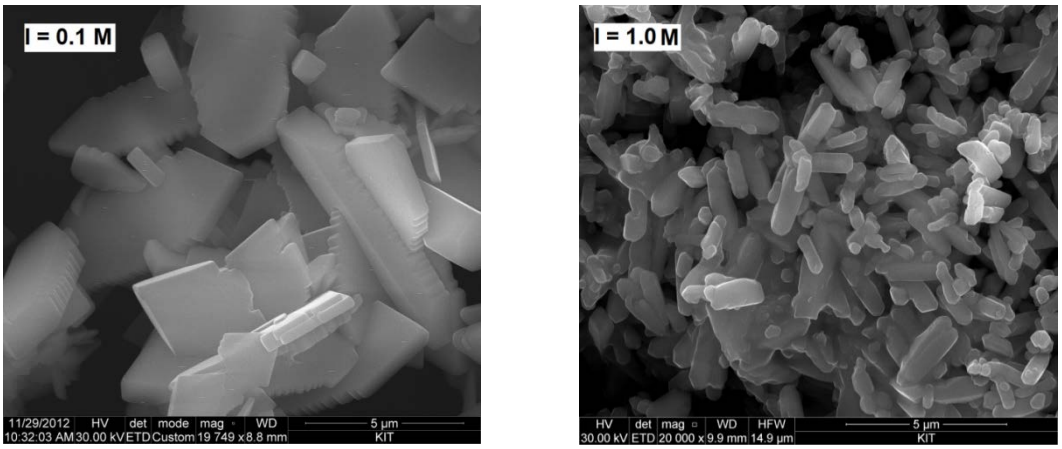

Figure 30. Scanning electron micrographs of celestite precipitated in solutions at different ionic strength, the reaction time was three days: left) 0.1 mol·kg^{-1} NaCl; right) 1.0 mol·kg^{-1} NaCl. SEM data indicate that the morphology of celestite shows a strong dependency on the ionic strength. At low ionic strength, the precipitates have a platelet-like morphology, while rod-like crystals are found at high ionic strength

The crystals formed at lower ionic strength have more a plate-like morphology and their size is relatively bigger. The particles formed at high ionic strength have a rod-like morphology, are higher in number and smaller in size, suggesting the existence of more impurities and consequently the formation of more nuclei. The different crystal morphologies may further be explained by the fact that the adsorption of background electrolytes occurs selectively on specific crystallographic edges and kink sites as found in earlier studies [193-195]. This indicates an interaction between the background electrolyte and specific sites on the mineral surface. As a consequence, surface features such as 2D-nuclei, growth spirals, and etch pits formed at high ionic strength are characteristically different from surface features which have developed in solutions with low ionic strength. When the ionic strength increases, the crystals become more elongated because of the relative increase in growth velocity in this specific direction. The changes observed in the induction times, together with the changes of the crystals morphology (Figure 30), suggest that the ionic strength (including increased impurity concentration) has an influence on the nucleation kinetics of celestite [193].

To decouple the effect of impurities (coming from the increased concentration of background electrolyte) from that of the supersaturation, additional experiments with strontianite were carried out at constant Sr^{2+} and CO_3^{2-} concentrations and variable concentration of the background electrolyte (NaCl). Here, the mean ionic activity coefficients are allowed to decrease with increasing ionic strength. The results plotted in Figure 31 show an increase of induction time with increasing

ionic strength (increasing impurities concentration) contrary to the experiments with celestite. This suggest that the observations made in Figure 29 cannot be attributed alone to the increase of the concentration of impurities. The kinetics of nucleation seem to be controlled rather by the absolute solute concentration (not the supersaturation); the amount of impurities present in the solution seems not to have a major impact on the induction period.

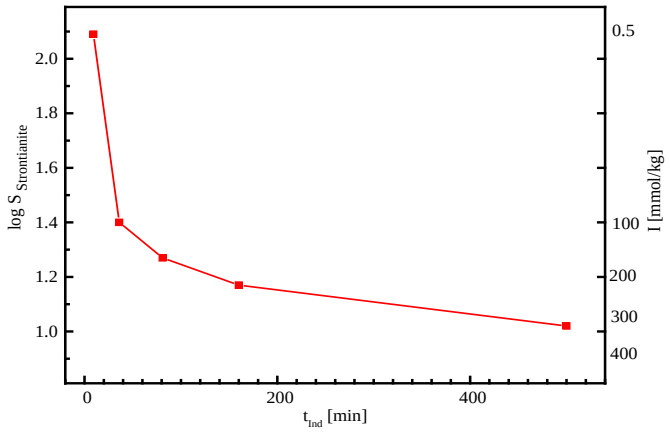

Figure 31. Induction time of strontianite as a function of the ionic strength. The solute concentration ($4.74 \cdot 10^{-4}$ mol·l^{-1}) is kept constant, causing the supersaturation (Y-axis left) to decrease with increasing ionic strength (Y-axis right). This results in a decrease of the induction time with increasing ionic strength (and hence increasing impurities in the solution).

4.1.8 Effect of dissolved silica

To investigate the impact of dissolved silica on the nucleation period for the crystallization of celestite and strontianite, the supersaturation of the solution was kept constant (S = 12.6 and 31.6 for celestite and strontianite, respectively) while varying the concentration of dissolved silica from 0 to 8 ppm. Results are summarized in Annex 10 and plotted in Figure 32.

In a series of experiments conducted at room temperature by mixing solutions of Na_2SO_4, Na_2SiO_3 and $SrCl_2$, Pina et al. [162] reported that the presence of dissolved silica led to significant changes in the nucleation kinetics within the $SrCl_2 - Na_2SO_4 - H_2O$ system. At low concentrations of dissolved silica ([Si] < 100 ppm), they observed an increase in the induction times for homogeneous nucleation. Such an increase was more pronounced for solutions with lower supersaturation with respect to celestite. Further, Pina et al. [162] found that for [Si] ≥ 100 – 150 ppm, the increase of the concentration of dissolved silica in the solutions results in a rapid reduction in the induction times and the formation of strontium sulfate hemihydrate instead of celestite. The promotion of nucleation

at higher silica concentrations was explained by the formation of polysilicates, which then provide a surface for the heterogeneous nucleation of the strontium sulfate hemihydrate.

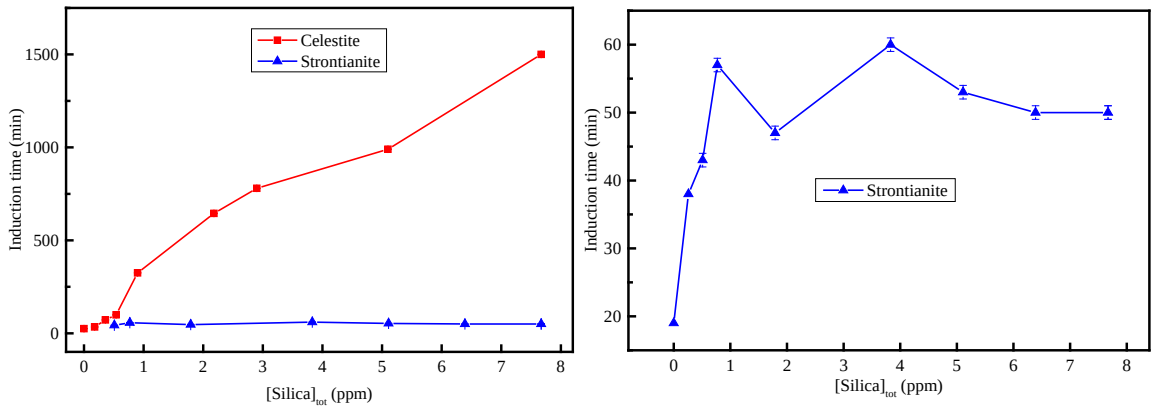

Figure 32. Effect of dissolved silica on the induction time t_{Ind} of celestite (red squares S = 12.6) and strontianite (blue triangles, S = 31.6) at constant temperature (297 K). The retardation effect increases continuously in the celestite samples, while the induction time for the strontianite samples already reaches a quasi-plateau at 1 ppm of silica. The right plot is a zoom-in of the strontianite data (blue triangles on the left plot)

In a preliminary experiment using commercially available Na_2SiO_3 (VWR), a spontaneous precipitation of a phase identified as strontianite was observed when the silica solution was mixed with a strontium chloride solution. The high carbonate content of the silica stock solution probably comes from residual dissolved CO_2 based on the industrial synthesis of Na_2SiO_3 starting from metal carbonate salts. To overcome this difficulty, the silica solution used in this thesis was synthesized from Silibeads® as described in chapter 3.1. ICP-OES analysis reveals that the filtrate was composed of 1.63% Ca^{2+}, 52,19% Si^{4+} as silicates, and 46,18% Na^{+}. The release of other constituents of Silibeads® (Al, Mg) was not observed. According to solution speciation calculations with PhreeqC, the solutions used in this study are undersaturated with respect to minerals involving Ca-ions. We assume in the following that the Ca-ions act as background electrolytes. The experimental data obtained in this thesis show an increase of induction time with increasing concentration of dissolved silica. The silica concentration used in this work covers the silica concentration range found in pore water of natural clay formations [4, 196]. Within this concentrations range, the retardation of nucleation was observed for both celestite and strontianite, as the induction time increased with increasing silica concentration. The retardation is more pronounced and increases almost linearly in the case of celestite, causing the induction time to increase from 25 min in the absence of silica to 1500 min at a silica concentration of 7.7 ppm. Surprisingly, an increase of the induction times for the nucleation

of strontianite with increasing silica concentration is observed only at [Si] < 1 ppm. At [Si] > 1 ppm, increasing the silica concentration has only minor impact on the induction times. The high impact of silica on the celestite samples may be due to the tetrahedral geometry of both silica and sulfate ions, which facilitates the exchange of sulfate by silica molecules, so increasing the inhibitory effect. Exchange of a trigonal planar carbonate ion by the tetrahedral silica is accordingly energetically less favorable, and hence the inhibitory effect is less pronounced for the strontianite samples. It is not clear so far at which stage exactly (nucleation vs. growth) this retardation effect occurs, since the experimental setup in this thesis allows only determination of the induction times and do not provide information regarding the mechanisms of the processes taking place. Nevertheless, Pina et al. [162] have suggested such retardation effect to result from an increase in the interfacial free energy between the crystal and the solution. This increase in turn is due to the modification of the crystal surface properties by the inhibitors. Such a modification can occur by adsorption of the inhibitors onto the surfaces of nuclei or on the surface of the growing crystal or both.

XRD spectra recorded for celestite precipitated at different silica concentrations, namely 4 and 10 ppm are shown in Figure 33 and compared to the spectrum recorded from precipitates grown in the absence of silica.

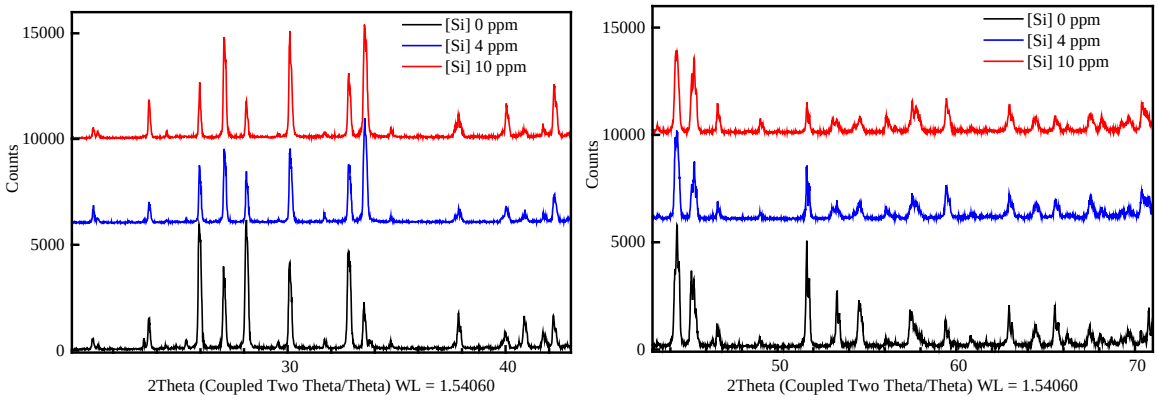

Figure 33. Diffraction patterns of the precipitates obtained from the celestite nucleation experiments at a supersaturation ratio S = 31.6 as a function of the silica concentration: black line – no silica; blue line – 4 ppm silica; red line – 10 ppm silica.

In the XRD diffraction patterns (Figure 33), the appearance of new peaks in the diffraction pattern is not observed upon addition of silica to the solution. The main change observed is related to changes in the scattering intensity. It is unclear whether the peak intensities changes due to changes in the structure factors upon incorporation of silica into the crystals or if they are an effect of preferred

orientation due to changes in in morphology. Comparison of the XRD-patterns with known strontium silica phases shows that no strontium silicates are formed in the experiments carried out in this thesis.

4.1.9 Effect of glass beads as heterogeneous seed material

In the presence of a suitable foreign body or surface, nucleation can be induced at degrees of supersaturation lower than those required for primary homogeneous nucleation, and the morphology and/or composition of the resulting precipitates can strongly differ from that formed in homogeneous nucleation processes. The foreign seeding material of interest in this chapter is quartz sand. The mixture of sand with bentonite is considered as an appropriate backfill material in geo-engineered barrier for radioactive wastes [197]. In case of water intrusion, secondary phase formation would rather occur at the surface of a potential seeding material (sand, bentonite, primary minerals surface…) via primary heterogeneous nucleation or secondary nucleation, and primary homogeneous nucleation would play a minor role, except at high supersaturations.

The induction time for the nucleation of celestite and strontianite was measured at different solution supersaturations ($6 \leq S \leq 16$) by varying the total mass of glass beads addition therefore changing the specific surface area from zero to 250 cm^2 (per liter). Stirring of the solution during the experiments kept the beads suspended in the solution. The diameter of the tube through which the solution was pumped into the measurement cuvette of the LIBD was smaller than the diameter of the beads, so that all the beads were kept into the reaction vessel during the experiment. Furthermore, only approx. one tenth of the sample volume (50 ml out of 500 ml) was removed during the experiment, assuring the variation of the ratio between solution volume to beads surface to be negligible. Results are plotted in Figure 34. In general, the decrease of induction time was observed with increasing surface area of the glass beads. Therefore, we conclude that the beads act as a catalyst of nucleation for the two mineral phases (Celestine and strontianite). This promoting effect of glass beads is more pronounced at lower supersaturations compared to higher supersaturations and can be explained by the energetics of the nucleation process. We have also noticed a decrease of the metastable stable zone width in the presence of seeding material, as predicted by the CNT.

SEM pictures of the glass beads before and after the nucleation of celestite are shown in Figure 35. Before nucleation, the surface of the beads is smooth, presenting few cavities. Formation of a nucleus in a surface cavity reduces the energy barrier, which may vanish completely if the sum of the contact angles of the nucleus on the substrate and the half angle on the wedge-shape or conical cavity is less than 90 ° [62]. After nucleation, distinct small crystallites are observed at the glass surface. The glass beads may facilitate the nucleation, but once a nucleus is formed, further growth to larger crystals takes place preferably on the celestite nucleus.

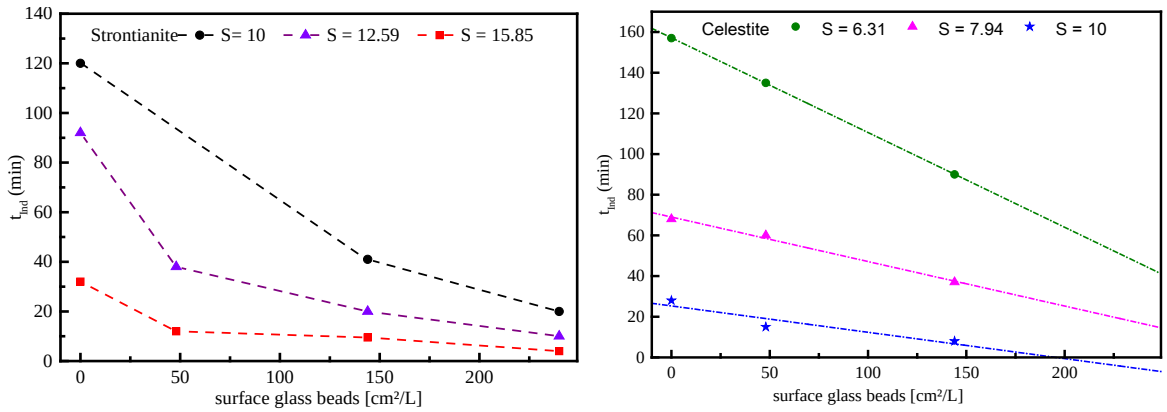

Figure 34. Induction time for the nucleation of strontianite (left) and celestite (right) as a function of the surface area of the glass beads. The dashed lines interconnect the measured data points and predict for the right plot (assuming a linear relationship) the dependence of the induction time on the surface of glass beads beyond the values assessed in this thesis.

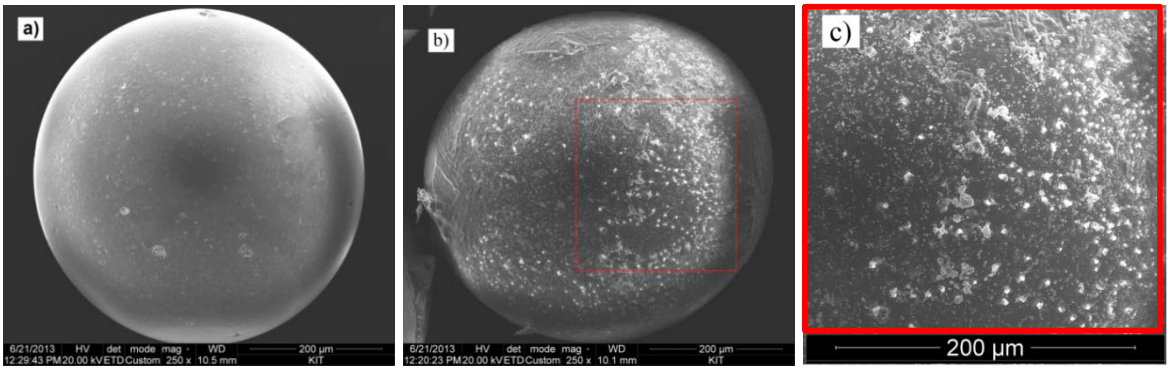

Figure 35. SEM pictures of glass beads: a) before celestite nucleation; b) after celestite nucleation; c) zoom-in of the area marked in red on b). The bright spots on the surface are crystals of celestite, NaCl is also found on the glass surface. This has been confirmed by an elemental analysis of the crystallites present on the bead surface (Annex 14).

4.2 Determination of growth rates from Mixed Flow Reactor (MFR) experiments

The kinetics of growth of celestite and strontianite from supersaturated solutions in the presence of seed crystals was studied in MFR experiments. In the majority of the experiments carried out at supersaturation ratios S < 10, the crystal yield was less than 500 mg and the specific surface area (SSA) of the crystal after the experiment could not be determined, since a minimum of 1 m² is necessary for a precise BET measurement. However, for the growth of strontianite at a

supersaturation ratio S = 3162, the SSA of the seed crystals increases from 0.64 ± 0.05 $m^2 \cdot g^{-1}$ before the experiment to 0.70 ± 0.05 $m^2 \cdot g^{-1}$ at the end of the experiment (see Annex 3 and Annex 4). For this reason, we assume the variation of the SSA during the growth experiments to be negligible, and consequently, the initial SSA of seed crystals is used in the determination of crystal growth rates. The macroscopic measurements of growth rates carried out in the present thesis cannot readily be interpreted in term of crystal growth mechanisms at the molecular level. Nevertheless, growth mechanisms that may be suggested based on relations between growth rates and supersaturation will be indicated. The influence of following factors on the growth kinetics of celestite and strontianite was studied: a) supersaturation; b) specific surface area (SSA) of the seed crystals; c) temperature and d) ionic strength. The effect of each of these variables on the growth rates will be discussed in a separate sub-chapter.

4.2.1 Effect of supersaturation

The growth rates of strontianite and celestite determined from MFR experiments, and for most normalized to the physical surface area of the seed crystals measured by BET before the growth experiment, are summarized in Annex 15. Figure 36 and Figure 37 show the plots of the growth rates against the relative supersaturation (S-1) for strontianite and celestite, respectively, according to equation (25). An increase of the growth rates with increasing supersaturation is observed.

At relative supersaturation $S - 1 \leq 30$ (celestite) and $S - 1 \leq 50$ (strontianite), the dependence between growth rate and relative supersaturation is linear. Therefore, in this supersaturation range, the growth may be controlled by the adsorption of growth units onto the crystal surface, which occurs via their diffusive transport through an interfacial stagnant water layer to the crystal surface, followed by their integration on the crystal lattice (see chapter 2.3). From a microscopic point of view, the rate limiting step of diffusion controlled growth is the dehydration of the constituent ions [198]. Due to their higher charge density, cations are more strongly hydrated than anions [199], and their incorporation in the solid should limit the rate of crystal growth. By combining the equations (25) and (28), rate constant were determined as follow:

- $1.27 \pm 0.12 \cdot 10^{-9}$ $mol \cdot m^{-2} \cdot s^{-1}$ for strontianite
  $9.24 \pm 0.75 \cdot 10^{-8}$ $mol \cdot m^{-2} \cdot s^{-1}$ celestite

These rate constants remain unvaried for the supersaturation range where the dependency of growth rates on relative supersaturation is linear. At relative supersaturation $S - 1 > 50$, the growth rates are lower than predicted by the extrapolation of the linear fitting of the data at lower supersaturations, suggesting the growth to be no longer controlled by surface reaction only, but to be influenced by

primary homogeneous nucleation in the bulk solution. The apparent reaction order in equation (25) is greater than unity, causing the rate constant to decrease with increasing supersaturation.

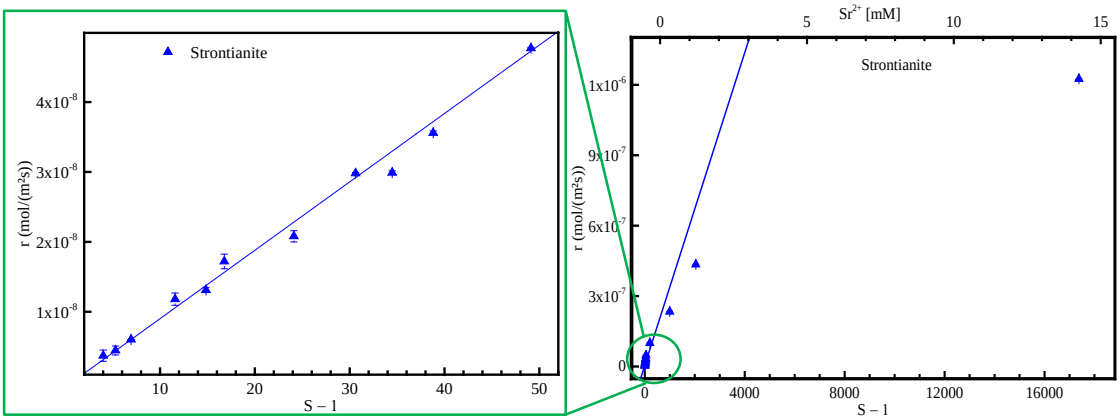

Figure 36. Growth rates of strontianite as a function of supersaturation. The plot on the left hand side is a zoom-in to the data at low (S < 10) to moderate (S <31) supersaturations. The initial strontium concentration given on the top x-axis is equal to the initial carbonate concentration.

When primary homogeneous nucleation occurs, normalizing the crystal growth rates to the surface area of the seed crystal would lead to erroneous results since the availability of the seed is no longer a prerequisite for nucleation to occur. If growth at S > 50 was controlled by homogeneous nucleation exclusively (what is not true since surface controlled growth still occurs), the relation between induction time (LIBD experiments) and nucleation rate (see equation (14) would be verified. Additional information relative to the macroscopic growth models are provided by the SEM data (Figure 38 and Figure 39).

The celestite data obtained at relative supersaturation S - 1 < 30 follow the same trend as the literature data of Hamdona et al. [160] and extend the latter to higher supersaturations. Using the formalisms of the transition state theory [101] of reaction kinetics, the empirical parameters in equation (25) are determined to be $m = 0.52 \pm 0.01$ and $n = 1.78 \pm 0.01$ for celestite. Similarly, the empirical parameters for strontianite are $m = 0.78 \pm 0.02$ and $n = 1.19 \pm 0.02$. The rate constant for the crystal growth of celestite determined in this study is 1.8 times higher than the value of $5.1 \cdot 10^{-8}$ mol·m^{-2}·s^{-1} proposed by Marty et al. [200], which have been determined assuming the empirical parameters m and n to be 0.5 and 2, respectively. The present study shows that kinetic parameters derived from dissolution experiments can differ by several orders of magnitude from the kinetic parameters determined in precipitation experiments. For example, a rate constant of $1.2 \cdot 10^{-6}$ mol·m^{-2}·s^{-1} (which is by two order of magnitude higher than the rate constant for celestite precipitation) was determined from celestite

dissolution experiments and is used in older databases for the modelling of celestite precipitation[192, 201].

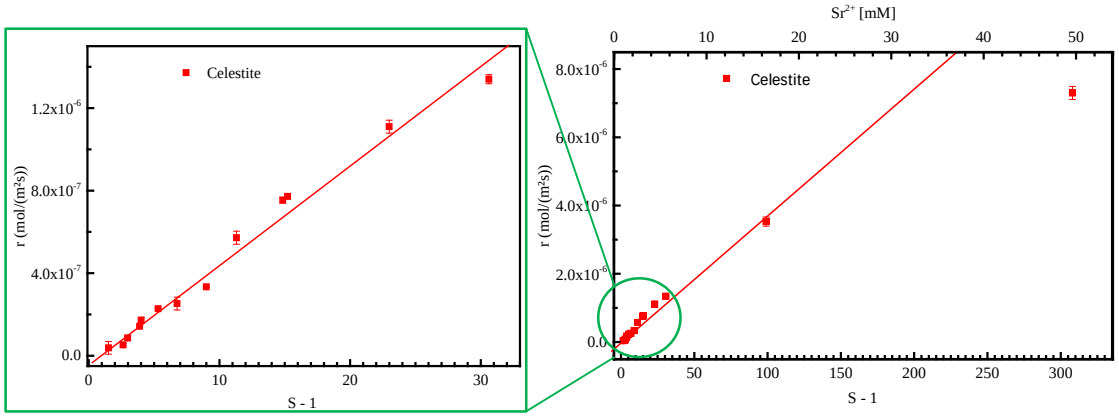

Figure 37. Growth rates of celestite as a function of supersaturation. The plot on the left hand side is a zoom-in to the data at low (S < 10) to moderate (S <31) supersaturations. The initial strontium concentration given on the top x-axis is equal to the initial sulfate concentration.

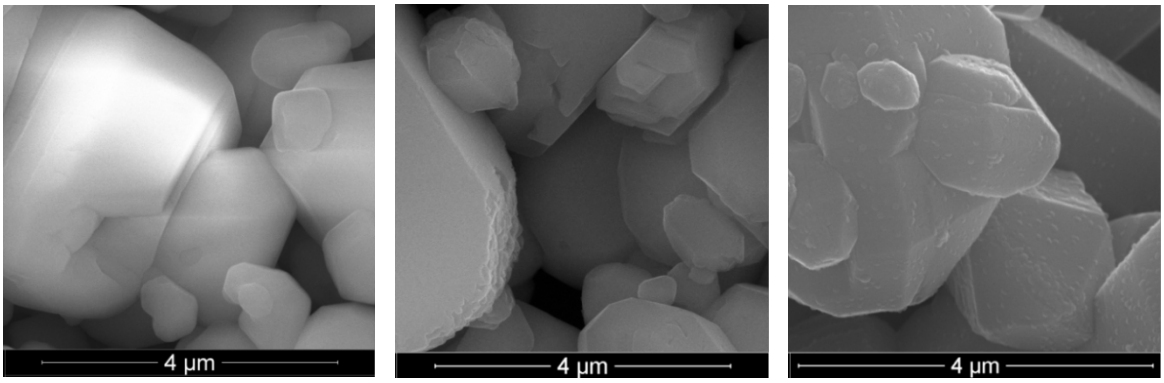

Figure 38. SEM pictures of strontianite seeds crystals: Left) before MFR; middle) after MFR at S = 2.6; right) after MFR at S = 25.7. The change of the crystal topology as a function of the supersaturation may be an indication to different mechanisms of growth.

The initial size of seed crystals was about 1 - 5µm for both strontianite and celestite as SEM images show (Figure 38 and Figure 39, respectively). For growth experiments at supersaturations S ~ 2.5, an increase of the average size of seed crystals is observed without any significant modifications regarding the morphology of their surface. This supports the theoretical expectation of growth at kinks, steps and edges at low supersaturations. However with the increasing supersaturation (S = 25.7), the surface of the strontianite crystals becomes very rough. The presence of hillocks of the

surface may be a hint for the formation of primary homogeneous nuclei in the bulk solution with their subsequent attachment to the surface of the larger crystals. Similarly, the occurrence of crystals smaller in size than the initial seed crystals is observed at a supersaturation S = 24.6 for celestite, also suggesting the occurrence of primary homogeneous nucleation.

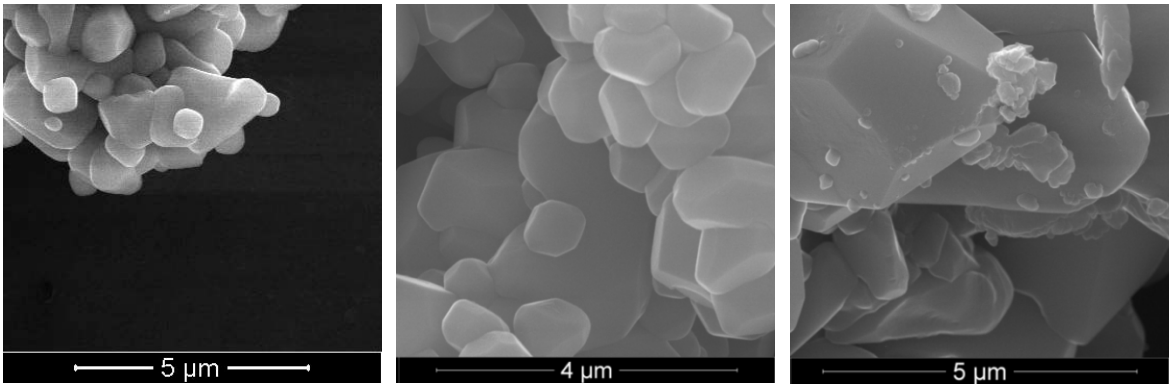

Figure 39. SEM pictures of celestite seed crystals: Left) before MFR; middle) after MFR at S = 2.5; right) after MFR at S = 24.6

4.2.2 Effect of the reactive surface area of seed crystals

To investigate how the reactive surface of seed crystals influences the growth rates, experiments were carried out at constant supersaturation while varying the amount of seed crystals. The results (absolute values) are given in Annex 16 and Annex 17.

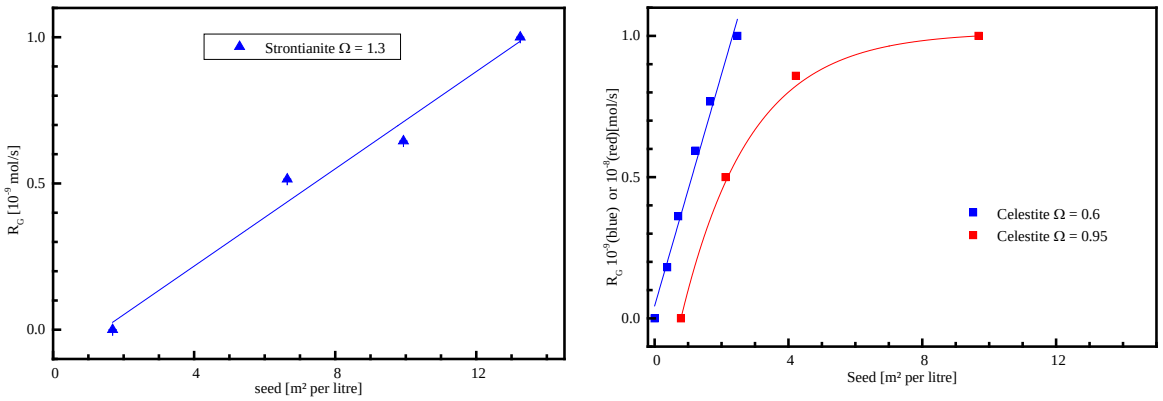

Figure 40. Growth rates of strontianite (left) and celestite (right) as a function of the surface area of the seed crystals. The rates are not normalized to the reactive area of the seed crystals, but are normalized among themselves (absolute values for growth rates are given in Annex 16 and Annex 17). The given seed surface area is related to one liter of solution.

In general, when the growth rate is not normalized to the surface area of the seed crystals, it increases with increasing amount of seed crystals (Figure 40), as one should expect for a surface reaction controlled growth. This is only valid as long as the density of reactive sites on the seed crystals surface is the rate determining step. When the density of reactive sites exceeds the amount of growth units arriving at the crystal surface per unit of time, the latter becomes the rate determining step. This explains the decrease of slope observed above 4 $m^2 \cdot l^{-1}$ (red data points in Figure 40). If a sufficient large surface area is available, a saturation effect occurs and additional increase of the reactive surface area will not result in a further increase of the growth rate. This case is nearly approached for celestite at $\Omega = 0.95$, where the increase of the growth rate is less steep for a seed surface between 4 and 10 $m^2 \cdot l^{-1}$ as for lower seed surfaces (0 – 4 $m^2 \cdot l^{-1}$). The rate obtained for the celestite growth in the absence of seed crystals is positive, suggesting either the occurrence of primary homogeneous nucleation under the experimental conditions, or showing that primary heterogeneous nucleation can occur at the reactor walls.

4.2.3 Effect of temperature

The activation energies for mineral-water reactions generally range from a few $kJ \cdot mol^{-1}$ to larger than 400 $kJ \cdot mol^{-1}$. Arrhenius proposed that the activation energy is the minimum amount of energy necessary to initiate a reaction[10, 202]. The magnitude of this activation energy usually gives a hint to reaction mechanisms taking part. For example, activation energies for mineral dissolution as low as 20 $kJ \cdot mol^{-1}$ have been attributed to reaction rates limited by diffusion of reactants to the mineral surface or reaction products away from the mineral surface. Contrary, activation energies of approximately 80 $kJ \cdot mol^{-1}$ are generally attributed to bond-breakage being the rate-limiting reaction step [203] indicating surface reaction control. Here, reaction rate constants were calculated using equation (25) and assuming the empirical parameters m and n to be unity. The slope of a plot of ln k vs the inverse of the absolute temperature (T^{-1}) yields the activation energy according to equation (26). Growth rates of celestite and strontianite have been measured systematically as a function of temperature from 278 to 338 K in 0.1 $mol \cdot kg^{-1}$ NaCl solutions. The results summarized in Annex 18 are plotted in Figure 41. The experimental data indicate that the growth rate constants are strongly temperature dependent. As the temperature increases, the growth rates of both celestite and strontianite increase. The values of activation energies of crystal growth obtained from the linear regression of the growth rate constants are:

- $E_a = 17.8 \pm 0.8$ $kJ \cdot mol^{-1}$ for celestite
- $E_a = 35.7 \pm 0.1$ $kJ \cdot mol^{-1}$ for strontianite.

Activation energy of 28 ± 2 kJ·mol^{-1} has been determined by Dove et Czank [192] from the temperature (298 – 413 K) dependence of the celestite dissolution. Studying the crystal growth kinetics of strontium sulfate in the primary heterogeneous nucleation regime (deposition of strontium sulfate crystals on a U-tube immersed in a supersaturated solution), Lee et al. [204] have determined the activation energy of 85 kJ·mol^{-1} at the temperature range 303 to 333 K.

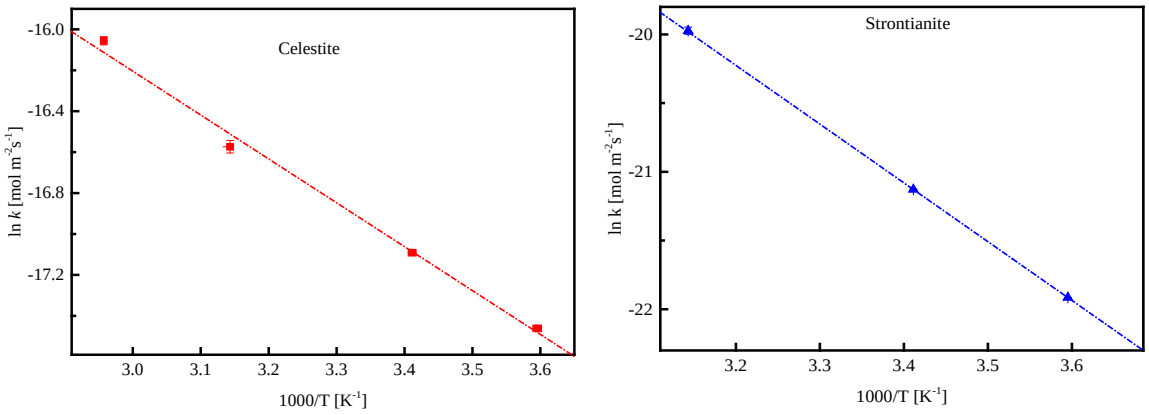

Figure 41. Arrhenius plots showing the dependency of precipitation rate upon temperature for celestite (left) and strontianite (right). The plotted rate constants are derived from precipitation rates using equation (25).

4.2.4 Effect of ionic strength

The influence of the ionic strength on the growth kinetics of celestite at 22 °C was studied at constant supersaturation ratio S = 10 with respect to celestite while varying the NaCl concentration between 0.1 and 2 mol·kg^{-1}. The strontium sulfate concentrations corresponding to a supersaturation ratio S = 10 are given in Annex 19.

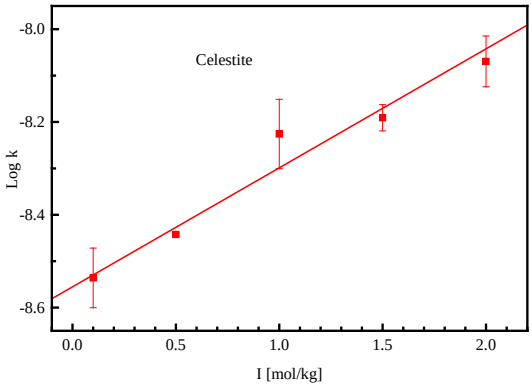

Figure 42. Log k-values for the crystal growth of celestite as a function of the ionic strength. The crystal growth rates, from which the log k-values were calculated, are summarized in Annex 19.

The measured crystal growth rates increase with increasing ionic strength (increasing NaCl concentration). The rate constants (log k) calculated from the measured growth rates using equation (25) are plotted in Figure 42 as a function of the ionic strength. Figure 42 shows a linear increase of the logarithm of the reaction rate as a function of the ionic strength. In homogeneous nucleation experiments, the increase of the ionic strength while keeping constant the supersaturation ratio was found to induce a decrease of the induction period (chapter 4.1.7). This also correlates with the increase of the rate constant observed in Figure 42. Risthaus et al. [193] have suggested that the increase of the crystal growth rates with increasing ionic strength (at constant supersaturation) may be due to an attachment of Na^+ ions to preexisting growth islands, so starting a new growth row. The formation of a new growth row, also referred to as kink site nucleation, is the rate limiting step for growth in solutions at low salinity. Similar observations made by Zuddas et al. [205] studying the influence of ionic strength on the kinetics of calcite growth were attributed to a catalysis induced by the presence of the background electrolyte. In aqueous solutions of high ionic strength, the activity of water is reduced and the number of water molecules in the hydration shell of the ions is lower. This may reduce the energy required for the dehydration and facilitate the adsorption and incorporation of the ions on the surface [205].

4.3 TRFLS investigations of Eu(III) and Cm(III) uptake by celestite and strontianite

The co-precipitation of Eu^{3+} and Cm^{3+} with celestite and strontianite in homogeneous nucleation experiments as well as in seeded growth experiments was investigated. The motivation for this investigation was to determine if the species that trivalent actinides and lanthanides form with the ESN differ from those species formed by sorption/incorporation of the trivalent dopant ions into

macroscopic crystals of celestite and strontianite. Therefore, the first series of experiments is devoted to the speciation of Cm(III) and Eu(III) in aqueous sulfate or carbonate solutions (chapter 4.3.1), followed by the interactions with early stage nuclei (chapter 4.3.2). The co-precipitation of Cm(III)/Eu(III) with celestite and strontianite in the presence of seed crystals is investigated in chapter 4.3.3.

The high fluorescence yields of Cm^{3+} enables direct speciation at the nanomolar concentration range. Therefore, Cm^{3+} ($5.30 \cdot 10^{-8}$ mol·l^{-1}) is chosen in this thesis as a representative for trivalent actinides [206]. Eu^{3+} has lower fluorescence yields than Cm^{3+}, but Eu^{3+} is an easy to handle, non-radioactive analogue for trivalent lanthanides and allows systematic studies at higher concentration ($1.30 \cdot 10^{-5}$ mol·l^{-1}), which would be difficult using the rare and radioactive Cm^{3+}. Even though the solution speciation (Thermoddem [154], PhreeqC [166]) does not suggest the formation of amorphous and crystalline complexes of europium with hydroxide- and carbonate- ions, it should be noted that the solubility limit of the latter can be exceeded due to the relatively high europium concentration ($1.30 \cdot 10^{-5}$ mol·l^{-1}). Relying on the experimental observations, which suggested a very limited intrusion of atmospheric carbon dioxide in the samples prepared on air, the speciation diagrams were calculated using the geochemical program HYDRA MEDUSA [168] and the ThermoChimie v.9 database [207] and assuming a complete exclusion of carbon dioxide. All MFR and homogeneous nucleation experiments involving curium were carried out in a glove box under an argon atmosphere. The ionic strength of all solutions is set to 0.1 mol·kg^{-1} by addition of NaCl and taking into account the contribution of all electrolytes.

4.3.1 Aqueous solution speciation

The complexation of Cm(III) and Eu(III) by sulfate and carbonate ions was investigated. The trivalent ions were added to solutions of sodium sulfate or sodium carbonate, respectively, and their fluorescence emission spectra recorded. The speciation diagrams below show the distribution of different aqueous species as a function of pH, and can be helpful for the interpretation of the fluorescence emission spectra. Previous investigations by Fanghänel et al. [208] have shown that the formation of curium chloride complex species occurs only when the chloride concentration exceeds 4 mol·kg^{-1}; this was taken into consideration for the solution speciation. Figure 43 shows the

speciation diagrams for europium and curium at those concentrations used throughout this study in $6.67 \cdot 10^{-3}$ mol·l^{-1} sulfate solutions.

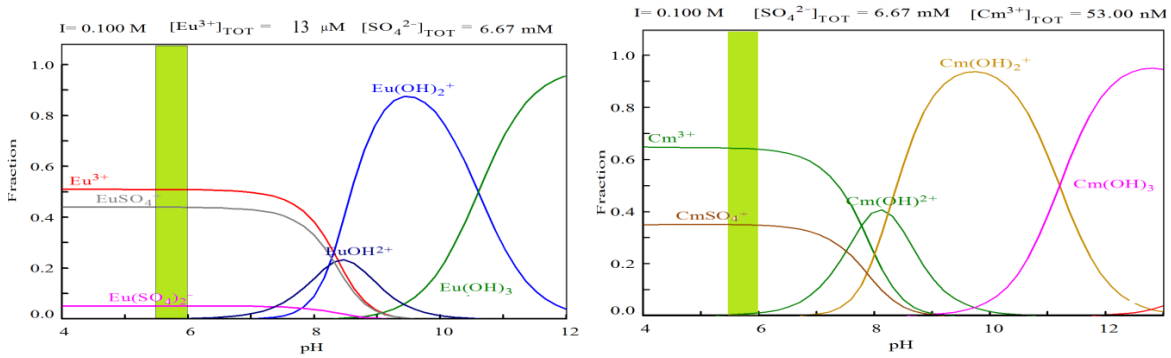

Figure 43. Speciation diagrams of Eu^{3+} (left) and Cm^{3+} (right) in sulfate solutions. $[SO_4^{2-}]_{TOT}$ = 6.67 mM; ionic strength = 0.1 mol·kg^{-1}; $[Eu(III)]_{TOT} = 1.30 \cdot 10^{-5}$ M; $[Cm(III)]_{TOT} = 5.3 \cdot 10^{-8}$ M; pH = 5.8 ± 0.2 (green bands on the diagrams).

For the sulfate solutions (ionic strength 0.10 mol·kg^{-1}; $[SO_4^{2-}] = 6.67 \cdot 10^{-3}$ mol·l^{-1}; pH ~ 5.80; $[Eu(III)] = 1.30 \cdot 10^{-5}$ mol·l^{-1}; $[Cm(III)] = 5.30 \cdot 10^{-8}$ mol·l^{-1}), the speciation diagrams predict the solution to be dominated by the corresponding aquo species, namely ~ 50 % in the Eu(III) sample and ~ 65 % in the Cm(III) sample. The formation of important amounts of the mono-sulfato complexes is also expected for both the Cm(III) and Eu(III) samples. Additionally, small amounts of the di-sulfato species (< 10 %) can be assumed to be present in the Eu(III) sample. The fluorescence emission spectrum of Eu(III) corresponding to the speciation diagram above is shown in Figure 44 (left) and compared with the spectrum of the Eu(III) aquo species. The appearance of a peak at 579 nm, corresponding to the $^5D_0 \rightarrow {}^7F_0$ transition attests of the complexation of Eu^{3+} in the sulfate solution. The formation of the Eu(III) mono- and di-sulfato species is further supported by the changes observed in the hypersensitivity peak ($^5D_0 \rightarrow {}^7F_2$). The hypersensitive peak increases when

the ligand binds Eu^{3+}, with slight differences of its shape in relation to the different splitting effects of the $^7F_2$ level [209].

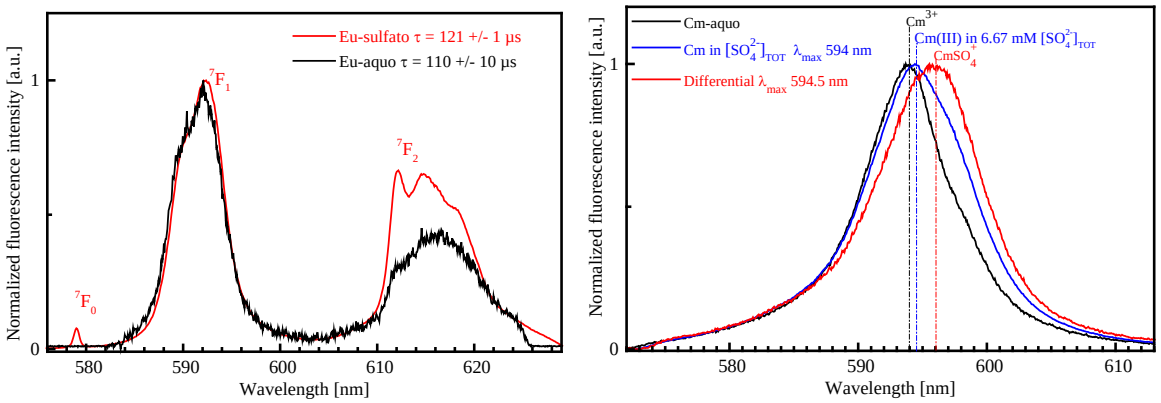

Figure 44. Fluorescence emission spectra of Eu^{3+} (left) and Cm^{3+} (right) in sulfate solutions, compared with the spectra of the aquo-ions. The differential spectrum is obtained by subtracting the fluorescence emission spectrum of the aquo ion from that obtained in the presence of sulfate ions. Experimental conditions: $[SO_4^{2-}]_{TOT}$ = 6.67 mM; T = 298 ± 2 K; I = 0.10 mol·kg^{-1}; $[Eu^{3+}]$ = 1.30·10^{-5} mol·l^{-1}; $[Cm^{3+}]$ = 5.30·10^{-8} mol·l^{-1} ; pH = 5.80 ± 0.2. Dotted vertical lines show the peak maxima of pure component species [206, 210]

The increase of the hypersensitive peak relatively to the intensity of the $^7F_1$ band correlates with the number of sulfate ions in the first coordination sphere of europium. The comparison of the intensities of the $^7F_1$ and $^7F_2$ in order to determine the number of sulfate ions in the first coordination sphere is difficult in the presence of a mixture of different sulfato species, as it is the case in the present study. The lifetime slowly increases with the formation of the mono- and di-sulfato complexes. For a solution containing a mixture of $Eu(SO_4)_2^-$ (4 %); $EuSO_4^+$ (38 %); and Eu^{3+} (58 %), Vercouter et al. [209] have determined a lifetime of 118 ± 10 µs, which indicates that 8.1 ± 0.5 water molecules remain in the first coordination sphere of the trivalent metal cation. This number of water molecules is just an average, and the sulfate species should contain less than 8 water molecules in their first coordination sphere, while the opposite would be expected for the aquo ion. The lifetime of 121 ± 10 µs determined in the present study (Figure 45) is comparable with the literature data [209], and supports together with the speciation diagram and the fluorescence emission spectra the presence of a mixture of europium- aquo and sulfato species.

The fluorescence emission spectrum of Cm(III) in the sulfate solution ($[SO_4^{2-}]_{TOT}$ = 6.67·10^{-3} mol·l^{-1}) is plotted in Figure 44 (right) and compared with the spectrum of the pure europium aquo ion. In the presence of sulfate ions, a slight red shift of the peak maximum is observed. The full width at

half maximum (FWHM) increases from 8 nm for the curium aquo species to 10 nm in the sulfate solution, suggesting the formation of additional species. A differential spectrum obtained by subtracting the fluorescence emission spectrum of the aquo ion from that obtained for the sulfate solution (red line) suggest the additional species to have an fluorescence emission maximum at ~ 596 nm. This corresponds to the peak maximum of for the $CmSO_4^+$ (596.2 nm) [206, 210], suggesting that the FWHM increase of the fluorescence emission peak observed in the presence of sulfate ions is due to the formation of $CmSO_4^+$ species, as predicted by the speciation diagram. However, the overall fluorescence is still dominated by the Cm(III) aquo ion, since the latter is the dominant species under the experimental conditions defined above. This is further supported by the measured lifetimes of 73 ± 10 µs (Figure 45).

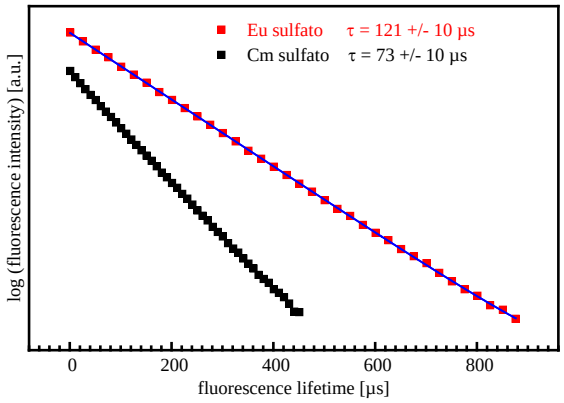

Figure 45. Lifetimes of europium and curium in sulfate solutions. The experimental conditions are depicted in the caption of Figure 44.

The carbonate complexation is one of the prominent geochemical reactions of actinides in natural aquifers. For the sake of completeness, and in order to differentiate between pure carbonate complexation and complexation by homogeneous nucleating strontium carbonate, the fluorescence spectrum of Cm(III) in carbonate solutions (I = 0.10 mol·kg^{-1}; $[CO_3^{2-}]$ = 4.30 – 87.20·10^{-4} mol·l^{-1}; pH = 10.10 – 10.80; [Cm(III)] = 5.30·10^{-8} mol·l^{-1}) was measured as a function of the total dissolved inorganic carbonate concentration $[CO_3^{2-}]_{TOT}$.(Figure 47) The corresponding speciation diagrams are shown in Figure 46.

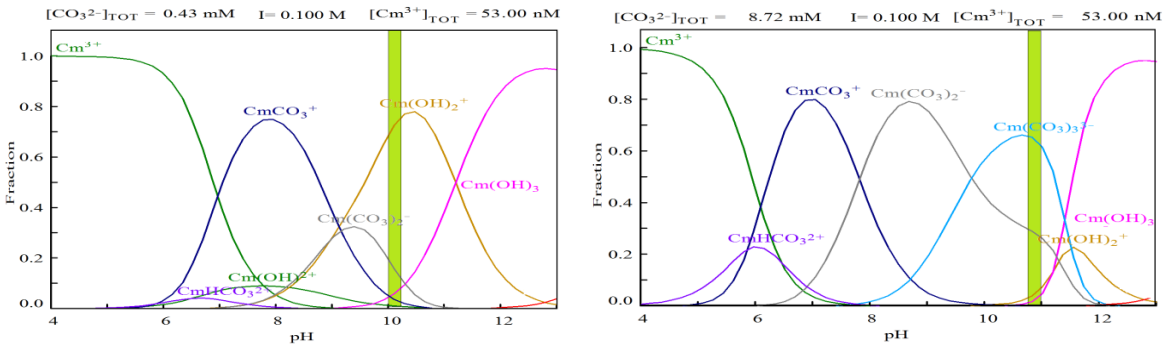

Figure 46. Speciation diagrams of Cm(III) as a function of the $[CO_3^{2-}]_{TOT}$. The vertical green bands shows the species prevailing at the respective pH-values of the solutions. The experimental conditions are as follow: I = 0.10 mol·kg^{-1}; T = 298K; $[Cm(III)]_{TOT}$ = 5.30·10^{-8} mol·l^{-1}, $[CO_3^{2-}]_{TOT}$ = 4.30·10^{-4} mol·l^{-1} (left plot); $[CO_3^{2-}]_{TOT}$ = 8.72·10^{-3} mol·l^{-1} (right plot)

The speciation diagrams clearly show that the solution speciation in the absence of strontium ions depends on the carbonate concentration. The pH of the solution increases with the increasing concentration of Na_2CO_3. At $[CO_3^{2-}]_{TOT}$ = 4.30·10^{-4} mol·l^{-1}, the solution has a pH value of 10.1 ± 0.1 and the dominant aqueous species can be summarized as follow: ~ 70 % $Cm(OH)_2^+$; 18 % $Cm(CO_3)_2^-$ and small amounts of $Cm(CO_3)^+$ and $Cm(OH)_3$. The fluorescence emission spectrum (Figure 47, red line) shows a peak maximum at 603.5 nm. This fits well with the peak maximum of the pure $Cm(OH)_2^+$ species, which has been isolated from other hydrolysis species by peak deconvolution [206]. A fluorescence lifetime of 84 ± 4µs was determined. However, the other species predicted by the speciation diagram to form under the experimental conditions of this study are also expected to contribute to the overall fluorescence emission and fluorescence lifetime.

Increasing the total carbonate concentration to 8.72·10^{-3} mol·l^{-1} (Figure 46, right) results in an increase of the pH (form 10.1 to 10.9). Here, the dominant solution species are the carbonato complexes $Cm(CO_3)_3^{3-}$ (~70 %) and $Cm(CO_3)_2^-$ (~ 30%). The peak maximum of the fluorescence emission spectrum (Figure 47, blue line) is located at 605.8 nm and overlaps with the reported peak maximum for the pure $Cm(CO_3)_3^{3-}$ species [206]. The determined lifetime of 100 ± 2 µs further supports the formation of Cm(III) carbonato species. Here again, the minor species contributes to the overall fluorescence emission and lifetimes. For this reason, the data in Figure 47 should not be seen as corresponding to pure species, but are rather a result of a mixture of different species.

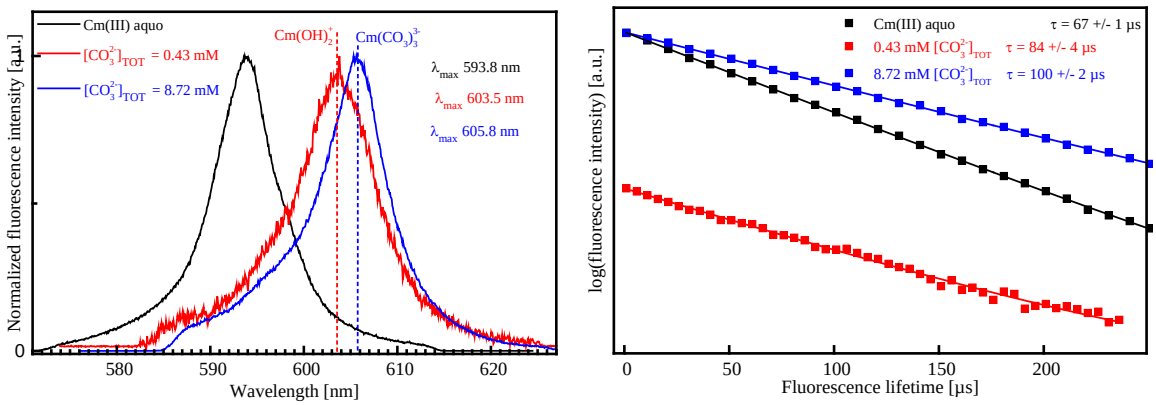

Figure 47. Fluorescence emission spectra (left) and fluorescence lifetimes (right) of Cm(III) ($5.30 \cdot 10^{-8}$ mol·l^{-1}) as a function of the $[CO_3^{2-}]_{TOT}$. The Cm(III) species in water, $4.30 \cdot 10^{-4}$ mol·l^{-1} $[CO_3^{2-}]_{TOT}$ and $8.70 \cdot 10^{-3}$ mol·l^{-1} $[CO_3^{2-}]_{TOT}$ are represented by the black (pH 5.8), red (pH 10.1) and blue (pH 10.9) lines, respectively. The ionic strength is 0.10 mol·kg^{-1} in all solutions. The vertical dashed lines show the peak maxima of pure component species [206].

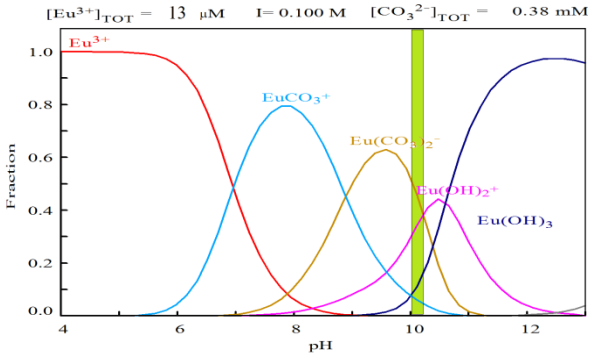

Figure 48. Speciation diagram of Eu(III) in carbonate solutions: $[CO_3^{2-}]_{TOT} = 3.80 \cdot 10^{-4}$ mol·l^{-1}; ionic strength = 0.10 mol·kg^{-1}; $[Eu(III)]_{TOT} = 1.30 \cdot 10^{-5}$ mol·l^{-1}; pH = 10.1 ± 0.1 (green area on the diagram). The species prevailing in solution under these experimental conditions are the europium di-carbonato as well as the di- and tri-hydroxo complexes.

Similar to the Cm(III) complexation, the complexation of Eu(III) in carbonate solutions is also a function of the solution pH and hence of the carbonate concentration. The speciation diagram in Figure 48 highlights the different species that will form in a solution with a total carbonate concentration of $3.80 \cdot 10^{-4}$ mol·l^{-1}. Here, the most abundant species are the di-carbonato and di-hydroxo complexes. Smalls amounts of the mono-carbonato and tri-hydroxo species are also observed. The corresponding emission spectra and lifetimes are shown in Figure 49. In the carbonate

solution, the emission peak maximum is located at the hypersensitive band (~ 615 nm) of Eu(III), contrary to the Eu(III) aquo species. Furthermore, the hypersensitive band is twofold split, suggesting the presence of at least two species, since the pure Eu(III) carbonato or hydroxo species do not show such peak splitting [211]. These two species are thought to be a mixture of $Eu(OH)_2^+$ and $Eu(CO_3)_2^-$, as suggested by the speciation diagram and the fluorescence emission band. Plancque et al. [211] have calculated the fluorescence lifetimes of the $EuCO_3^+$, $Eu(CO_3)_2^-$, $Eu(OH)_2^+$ and $Eu(OH)_3$ to be 180 ± 20, 290 ± 30, 40 and 40 µs, respectively. The measured lifetime of 183 ± 2 µs (Figure 49, right) supports the existence of a mixture of Eu(III) hydroxo and carbonato species, as additionally confirmed by the speciation calculations.

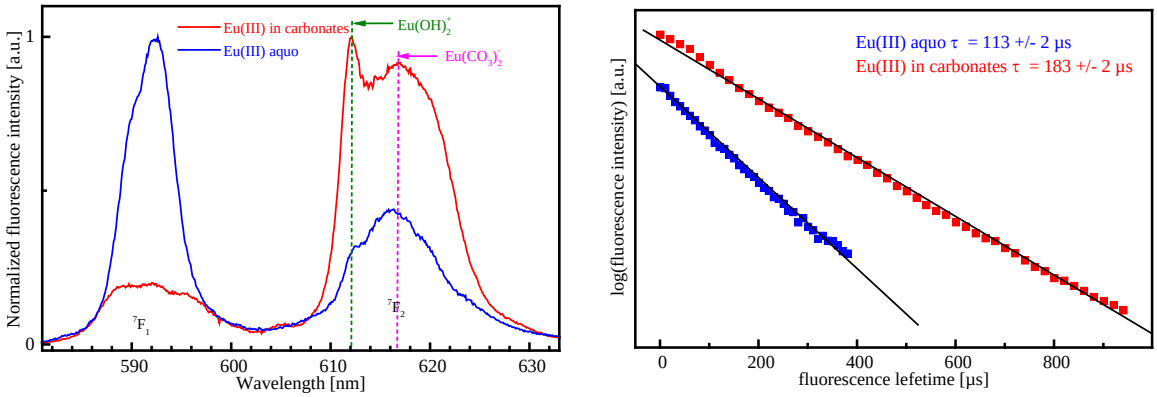

Figure 49. Fluorescence emission spectra and fluorescence lifetimes of Eu(III) in solution with a total carbonate concentration of $3.80 \cdot 10^{-4}$ mol·l^{-1} compared with the Eu(III) aquo ion. Ionic strength = 0.10 mol·kg^{-1}; pH = 10.1; $[Eu(III)]_{TOT} = 13 \cdot 10^{-6}$ M. The vertical dashed lines show the peak positions of the pure species [211].

4.3.2 Complexation by early stage nuclei (ESN)

In LIDB experiments, we have noticed that the formation of "early stage nuclei" (ESN) occurs almost simultaneously with the creation of supersaturation. The ESN was found to remain stable for few minutes up to several hours before the occurrence of quantitative nucleation (4.1). Also, TEM experiments have revealed that ESN formed during the nucleation of celestite are well crystalline (chapter 4.1.4). For the homogeneous nucleation of strontianite, TEM was not able to visualize ESN, a possible explanation for this is given in chapter 4.1.4. Relying on the results of LIBD and TEM, celestite and strontianite solutions with different supersaturation ratios were prepared as follow: trace amounts of the trivalent cations (Eu^{3+} or Cm^{3+}) were added to solutions of strontium chloride, followed by the addition of sodium carbonate or sodium sulfate solutions to achieve the desired supersaturation. The aim of these experiments was to figure out how ESN influence the speciation

of trivalent actinides and lanthanides, in comparison to macroscopic crystals (MFR-experiments). Therefore, fluorescence spectra were recorded for the condition where only ESN are present in the solution, and for the condition where quantitative nucleation has occurred.

4.3.2.1 ESN of celestite

To investigate the uptake of trivalent europium and curium by the ESN of celestite, solutions supersaturated with respect to celestite and containing trace amounts of the trivalent ions were prepared as described in 4.3.2, and the evolution of their fluorescence emission spectra with time was followed. The speciation diagrams of the supernatant after nucleation are shown in Figure 50.

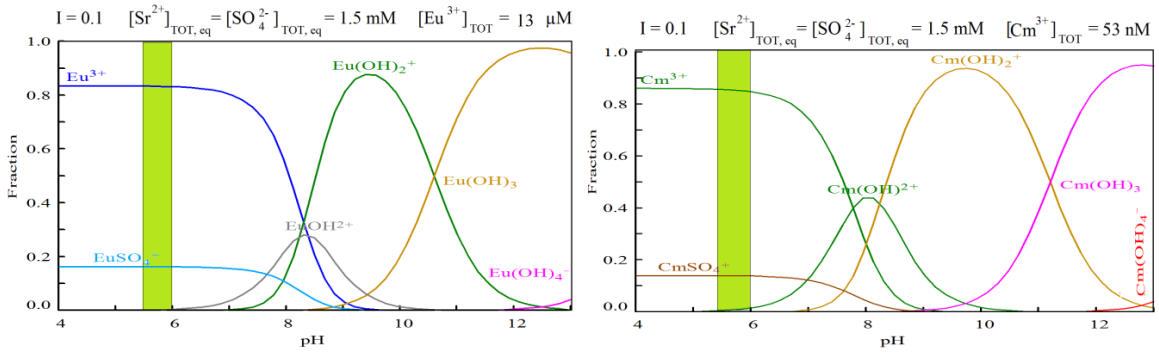

Figure 50. Speciation diagrams showing the solution species of Eu(III) (left) and Cm(III) (right) after the nucleation of celestite. The strontium ($1.50 \cdot 10^{-3}$ mol·l^{-1}) and sulfate ($1.50 \cdot 10^{-3}$ mol·l^{-1}) concentrations are predefined by the celestite solubility in 0.1 mol·l^{-1} NaCl at 298 K [190]. $[Eu^{3+}]_{TOT}$ = $1.30 \cdot 10^{-5}$ mol·l^{-1}; $[Cm^{3+}]_{TOT}$ = $5.30 \cdot 10^{-8}$ mol·l^{-1}; pH = 5.8 ± 0.2.

The solid species that can be formed when the trivalent cations are incorporated into celestite are not considered in the speciation diagrams. The sulfate concentration found in the supernatant after the nucleation of celestite from supersaturated solution is low ($1.50 \cdot 10^{-3}$ mol·l^{-1}) [190], and thus the formation of di-sulfato complexes (see Figure 43) is not observed. The supernatant is dominated by the aquo species (~ 83 %) and small amounts of the mono-sulfato species. Traces amount of the mono-hydroxo species are also found in the speciation diagram for Cm(III).

Europium- ESN celestite

Fluorescence emission spectra recorded at 1 min, 14 min, 5 h and 24 h, respectively after the start of the nucleation experiment are plotted in Figure 51 and compared with the fluorescence emission spectra of Eu(III) in a 6677 mM sulfate solution.

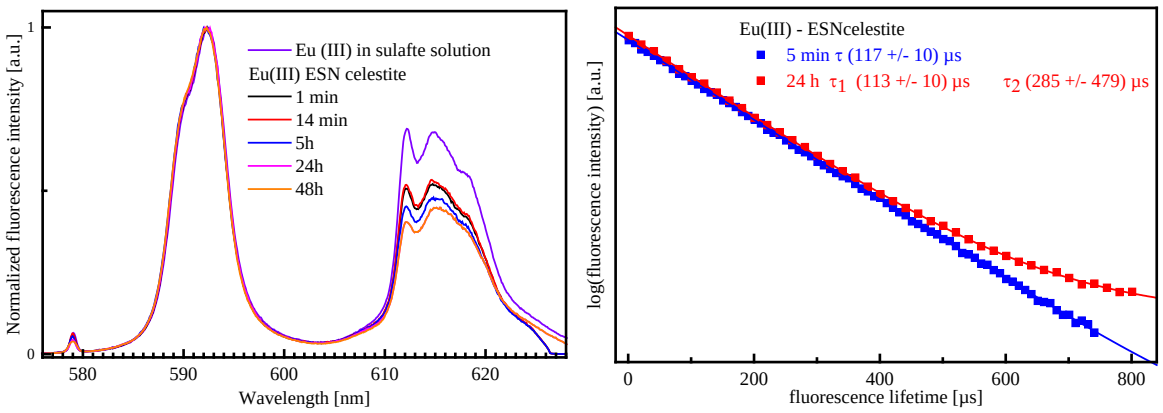

Figure 51. Fluorescence spectra (left) and fluorescence lifetimes (right) of Eu^{3+} ($1.30 \cdot 10^{-5}$ mol·l^{-1}) as a function of reaction time during homogeneous nucleation of celestite at S = 12.6 (initial sulfate concentration of $6.67 \cdot 10^{-3}$ mol·l^{-1}). The fluorescence spectra are compared with the spectra of $1.3 \cdot 10^{-5}$ mol·l^{-1} Eu(III) in a $6.67 \cdot 10^{-3}$ mol·l^{-1} sulfate solution. The lifetime measurement shows the formation of a second species after a reaction time of 24 h.

No changes are observed for the $^7F_0$ and $^7F_1$ bands within 24h. However, the hypersensitive band ($^7F_2$) of the spectrum recorded after 1 min of reaction time is much lower in comparison with the spectrum recorded in pure sulfate solution, although the initial sulfate concentration is the same for the two samples. This indicates that the sulfate concentration is much lower in the sample supersaturated with respect to celestite, supporting the observations made by LIBD that the formation of ESN occurs almost simultaneously with the creation of supersaturation. With the increasing reaction time, a slight decrease of the intensity of the hypersensitive band is observed, indicating a lowering of the "free sulfate" concentration in the samples and thereby the increase of the amount of ESN. The ESN containing Eu(III) remains a minor species during the observation period. Its formation does not considerably influence the fluorescence emission spectrum, which is dominated by the aqueous species. The distribution of the aqueous species depends also on the sulfate concentration: with the decreasing concentration of sulfate ions, the amount of Eu(III) mono-sulfato species decreases and the Eu(III) aquo species increases. The fluorescence lifetime change from a mono-exponential decay at the beginning of the experiment to a bi-exponential decay after 24 h. The appearance of a species with longer lifetime, together with the fluorescence emission spectra recorded at different delay after the excitation (Figure 52) further support the formation of the Eu-ESN species. The lifetime of the latter could not be determined precisely. The given value (285 ± 479 µs) should not be considered as a specific lifetime corresponding to the Eu(III)-ESN species.

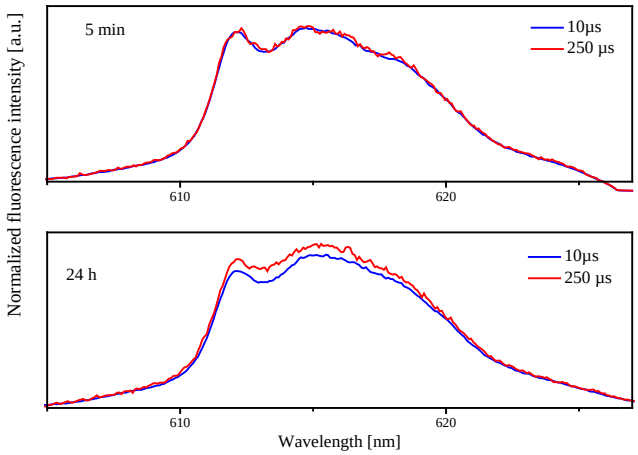

Figure 52. Hypersensitive bands of the fluorescence emission spectra of Eu(III) during the homogeneous nucleation of celestite recorded with different delay after the excitation as a function of the reaction time. $[Eu(III)]_{TOT}$ = $1.30 \cdot 10^{-5}$ mol·l^{-1}; $S_{celestte,\ initial}$ = 12.6; pH = 5.8; ionic strength = 0.10 mol·kg^{-1}.

Figure 52 shows the minor changes in the fluorescence emission spectra of Eu(III) in the presence of ESN of celestite. The upper spectra are recorded after 5 min and suggest the existence of species with similar lifetimes. The lower spectra recorded after 24 h of reaction time suggest the existence of an additional species with longer lifetime, supporting the sorption of Eu(III) onto celestite. Unfortunately, attempts to isolate the ESN of celestite containing Eu(III) by ultracentrifugation were unsuccessful. For this reason, the fluorescence lifetime and thus of the number of water remaining in their first coordination could not be determined accurately.

Curium-ESN celestite

The fluorescence emission spectra of Cm(III) as a function of reaction time during homogeneous nucleation of celestite from a solution with supersaturation S = 6.3 (with respect to celestite) is shown in Figure 53. The induction time corresponding to this supersaturation was determined in LIBD experiments to be t_{Ind} = 209 min. According to the speciation diagram (Figure 50, right), the predominant aqueous species of Cm(III) are the aquo- and the mono-sulfato complexes under our experimental conditions (see caption of Figure 53). The fluorescence emission spectra are identic to those measured for pure sulfate solutions (see Figure 44, right). Similarly to the observations made for Eu(III), the fluorescence emission spectrum recorded after a reaction time of 5 min readily shows a slight sulfate complexation, indicated by the a slight increase of the FWHM and a shoulder on the right side of the spectrum. With increasing reaction time, no further changes are observed in the spectra. The difference spectrum obtained by subtracting the spectrum of the Cm(III) aquo ion from

the spectrum of Cm(III) in the presence of ESN of celestite shows a second peak at 596 nm, clearly confirming the formation of the Cm(III) mono-sulfato species [206] (Figure 53, right).

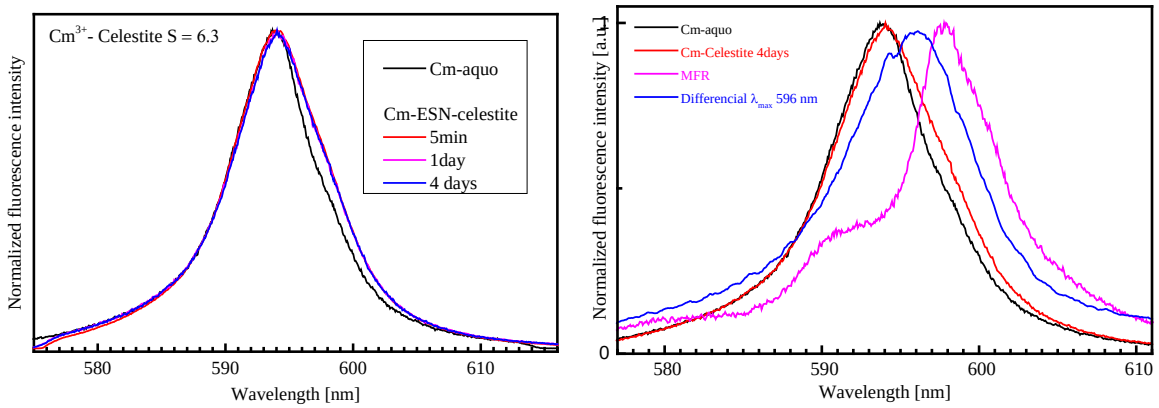

Figure 53. Fluorescence emission spectra of Cm(III) during the homogeneous nucleation of celestite at initial supersaturation S = 6.3, in comparison with the fluorescence emission spectra of Cm(III)-aquo ion. $[Cm(III)]_{TOT} = 5.3 \cdot 10^{-8}$ mol·l^{-1}; $[SO_4^{2-}]_{TOT} = 4.5 \cdot 10^{-3}$ mol·l^{-1}; ionic strength = 0.1 mol·kg^{-1}; pH = 5.8;. Left) spectra as a function of the reaction time. Right) Difference spectrum showing the presence of Cm(III) mono-sulfato species.

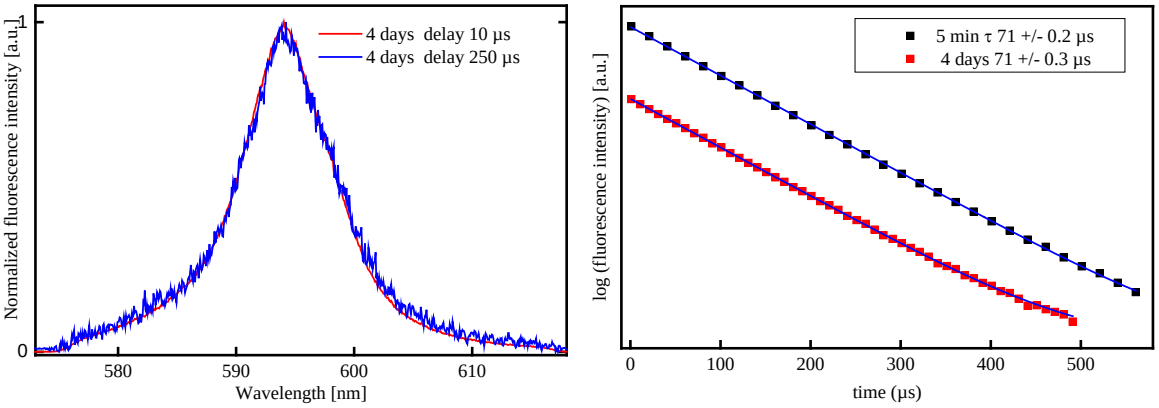

Figure 54. Left: Fluorescence emission spectra measured with different delay times. Right: fluorescence lifetimes for Cm(III) in a solution with supersaturation S = 6.3 with respect to celestite. Experimental conditions are given in the caption of Figure 53.

The measurement of the fluorescence lifetimes is shown in Figure 54. The emission spectra measured as a function of the delay time after excitation (Figure 54, left) do not show any sign of Cm(III)-ESN species formation at supersaturation S = 6.3 with respect to celestite. The mono-exponential decay

of the fluorescence lifetimes at 5 min and 4 days is an additional evidence for the non-formation of a species with longer lifetime. The measured lifetime of 71 µs results most probably from a mixture of the aquo ion (τ = 65 ± 2 µs) and the mono-sulfato species (τ = 88 ± 2 µs) [206]. The fact that no evidence is found for the formation of Cm(III)-ESN under the experimental conditions of Figure 54 is not in agreement with the observations made for the experiment with Eu(III) (see Figure 51). The discrepancies may be related to the different saturation ratios at which the experiments were carried out (S = 6.3 vs. S = 12.6 for Cm(III) and Eu(III), respectively). Therefore, additional experiments with Cm(III) were carried out at increased supersaturations with respect to celestite (S = 12.6 and 100). The corresponding fluorescence emission spectra are shown in Figure 55 (S = 12.6) and Annex 21 (S = 100). The induction time for the homogeneous nucleation of celestite at a supersaturation ratio S = 12.6 was determined in previous LIBD experiments to be 25 min.

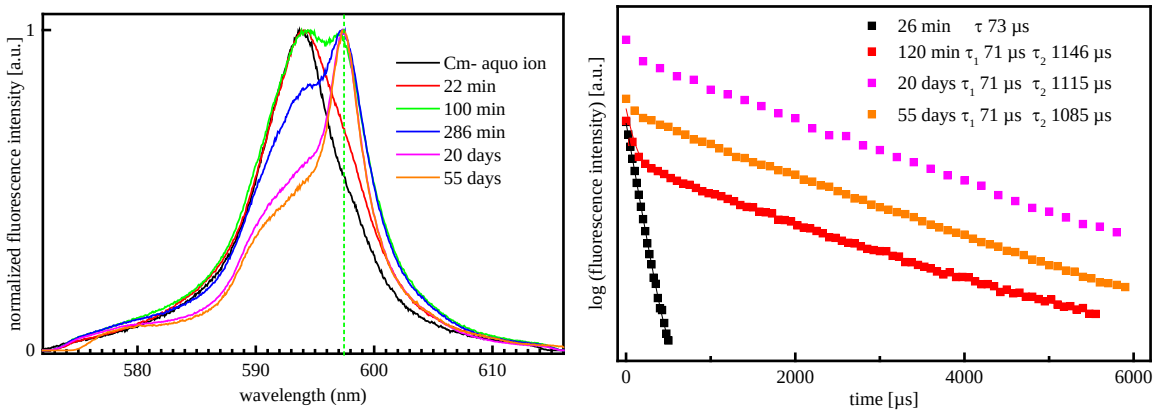

Figure 55. Left: fluorescence emission spectra of Cm(III) as a function of the reaction time during the homogeneous nucleation of celestite. Right: fluorescence lifetimes as a function of the reaction time. Initial supersaturation S = 12.6; $[Cm^{3+}]_{TOT}$ = 53·10^{-9} mol·l^{-1}; I = 0.1 mol·l^{-1} NaCl; ionic strength = 0.1 mol·kg^{-1}; $[SO_4^{2-}]_{TOT}$ = 6.67·10^{-3} mol·l^{-1}

The experiment at supersaturation S = 12.6 allows a more systematically investigation of the interactions between Cm(III) and celestite, from the ESN up to crystalline celestite, since massive crystalline precipitates are formed due to the relatively high solute concentrations. The spectrum recorded after 22 min of reaction time are similar to those observed at S = 6.3, indicating the fluorescence emission to be dominated by the Cm(III) aquo and mono-sulfato species. However, the shoulder indicating the speciation change of Cm(III) and potential sorption/incorporation into celestite becomes more pronounced as the reaction time increases, showing a peak maximum at 597.5 nm. This indicates the disappearance of the aqueous species with time, and thus the formation of Cm(III) solid species. The fluorescence emission maxima for the di- and tri-sulfato complexes of

Cm(III) are located at 599.5 and 602.1 nm, respectively [206]. Therefore, the red shift of the peak maximum cannot result from the formation of Cm(III) sulfato species. Fluorescence lifetimes measurements confirm the existence of the Cm(III) aqueous species (τ = 71 µs) and a Cm(III)-celestite species with a lifetime of τ = 1115 ± 31 µs, indicating total loss of water in the first coordination sphere.

The fluorescence data for Eu(III) shown in Figure 51 are at the same supersaturation ratio with respect to celestite as the fluorescence data for Cm(III) shown in Figure 55. Contrary to the Cm(III) sample, there was not clear evidence, but only a hint (Figure 52) for the incorporation of Eu(III) into celestite after an observation period of 24 h. The most probable reason for this is the difference in the concentrations of the trivalent cations ($5.3 \cdot 10^{-8}$ mol·l^{-1} Cm(III) vs. $1.3 \cdot 10^{-5}$ mol·l^{-1} Eu(III)), which is 25 times higher for Eu(III) than for Cm(III). Making use of equation (36) and assuming a 5% BDP for the supersaturation S = 6.3, the concentration of ESN is estimated to be $2.3 \cdot 10^{-6}$ mol·l^{-1}. The corresponding Eu(III) to ESN ratio is 5.6. This may cause the major part of Eu(III) to remain in solution in form of aqueous species and to dominate the overall fluorescence of the sample.

4.3.2.2 ESN of strontianite

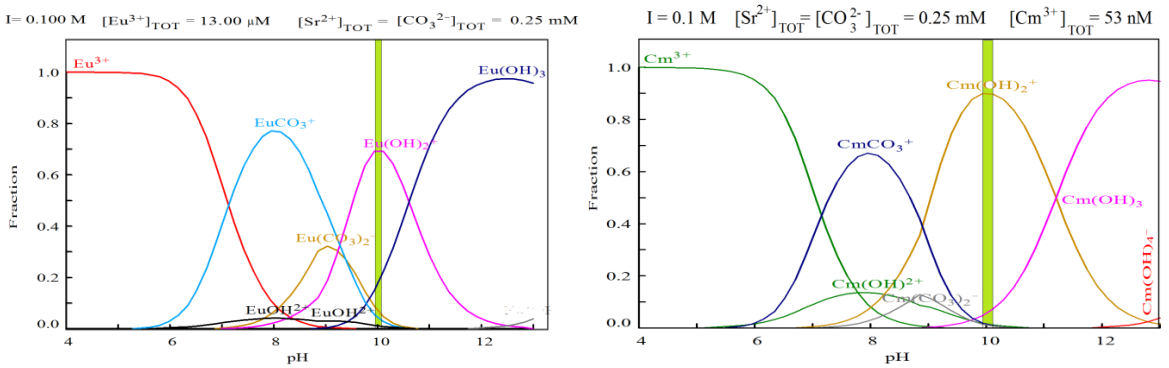

Figure 56. Speciation diagrams of Eu(III) and Cm(III) in strontianite. The solid Eu(III) and Cm(III) species are not considered, and the diagrams reflect the speciation of the supernatant at equilibrium with the mineral phase. Experimental conditions: ionic strength = 0.1 mol·kg^{-1}; $[CO_3^{2-}]_{TOT}$ = $2.50 \cdot 10^{-4}$ mol·l^{-1}. The green bands on the diagrams show the pH range (10 ± 0.1) of the solutions. left) $[Eu(III)]_{TOT}$ = $1.3 \cdot 10^{-5}$ mol·l^{-1}; right) $[Cm(III)]_{TOT}$ = $5.3 \cdot 10^{-8}$ mol·l^{-1}.

Additionally to the uptake experiments of trivalent europium and curium by celestite, curium and europium uptake experiments were carried out during the homogeneous nucleation of strontianite. The speciation diagrams (Figure 56) are calculated assuming the solution to be at equilibrium with

the precipitated strontianite. The equilibrium total carbonate concentration after the nucleation of strontianite has been determined to be $[CO_3^{2-}]_{TOT} = 1.0 \pm 0.1 \cdot 10^{-4}$ mol·l^{-1} [169]. The speciation diagrams show only the aqueous species, and the complexes formed by sorption or incorporation of the trivalent ions in strontianite are not considered. The aqueous speciation is determined by the total carbonate concentration in solution at equilibrium ($[CO_3^{2-}]_{TOT,\ Equilibrium} = 9.20 \pm 0.1 \cdot 10^{-5}$·mol·l^{-1}; HYDRA MEDUSA [168]; ThermoChimie v.9 database [169]), which in turn is defined by strontianite solubility under the experimental conditions. $Eu(OH)_2^+$ and $Cm(OH)_2^+$ are the most abundant aqueous species. Small amounts of the tri-hydroxo- and mono-carbonato complexes also form for both curium and europium.

Curium- ESN strontianite

For the Cm(III) uptake, experiments were carried out at supersaturation ratio of 6.3 and 1000 with respect to strontianite. The corresponding fluorescence emission spectra are shown in Figure 57.

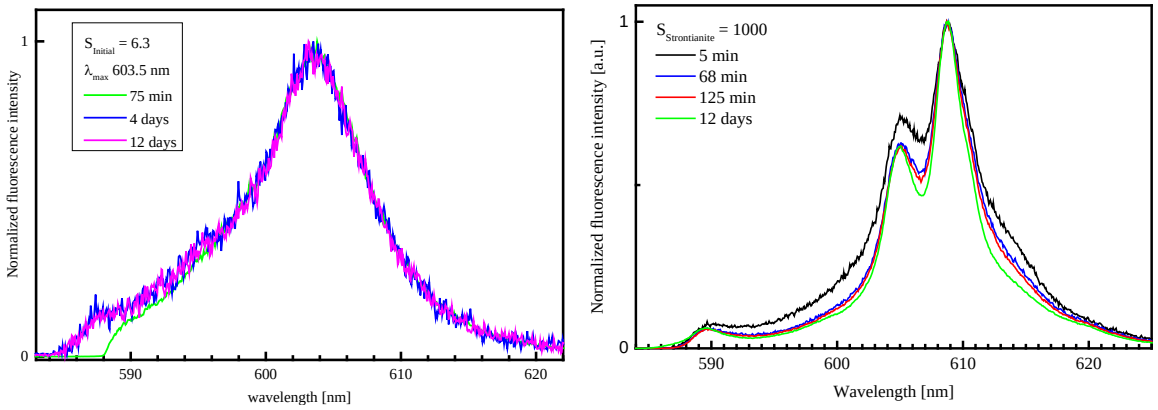

Figure 57. Evolution with time of the fluorescence emission spectra of Cm(III) in solutions supersaturated with respect to strontianite. S = 6.1 (left); S = 1000 (right). The experimental conditions are given in the caption of Figure 56. The fluorescence is dominated by the aqueous species at S = 6.3 and by the Eu-strontianite species at S = 1000.

For the supersaturation S = 6.3, LIBD investigations have shown that a small amount of ESN form directly after the creation of supersaturation, but quantitative nucleation does not occur within 48 h. The fluorescence emission spectra are dominated by the $Cm(OH)_2^+$ as predicted by the speciation diagrams, and no change in the spectrum occurs during the observation period of 12 days. However, lifetimes measurement (Figure 58) clearly confirms the existence of a minor species with a lifetime of 377 ± 89 µs. The number of water molecules in its first coordination sphere is estimated to be 0.9

± 0.5 using the Kimura equation (equation (29), suggesting a coordination according to the inner sphere mechanism.

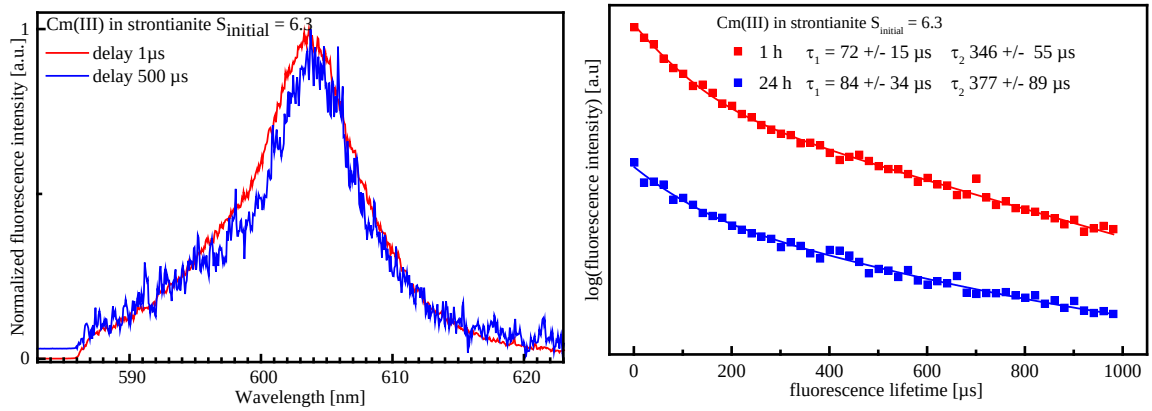

Figure 58. Fluorescence of Cm(III) in strontianite ($S_{initial}$ = 6.3). Left plot: fluorescence spectra at a reaction time of 24 h recorded with different delay after the excitation (1 µs and 500 µs). Right plot: fluorescence lifetimes recorded after a reaction time of 1h and 24 h. $[CO_3^{2-}]_{TOT}$ = 2.50·10^{-4} M; pH = 10 ± 0.1; ionic strength = 0.1 mol·kg^{-1}. No change is observed in the spectra within the observation time of 24 h.

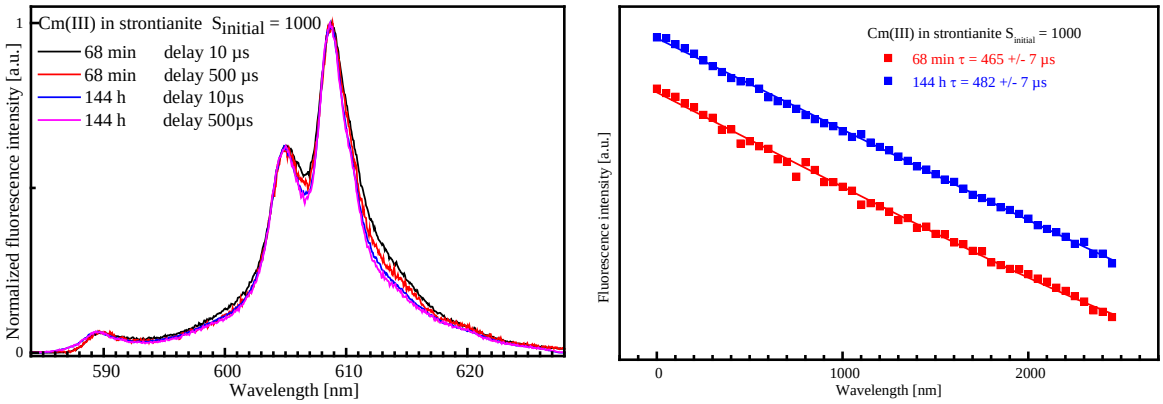

Figure 59. Fluorescence of Cm(III) in strontianite ($S_{initial}$ = 1000). Left plot: fluorescence spectra at a reaction time of 68 min and 144 h recorded with different delay (10 and 500 µs) after the excitation. Right plot: fluorescence lifetimes recorded after a reaction time of 68 min and 144 h. $[CO_3^{2-}]_{TOT}$ = 2.50·10^{-4} M; pH = 10 ± 0.1; ionic strength = 0.1 mol·kg^{-1}.

When the supersaturation is high enough to induce quantitative nucleation (S = 1000, induction time < 1 min), the fluorescence spectra shows the formation of Cm(III)-strontianite species (Figure 57

right). We should notice here that the fluorescence spectrum at S = 1000 cannot be explained by the speciation diagram for the simple reason that the aqueous complexes become the minor species when supersaturation is high enough, contrary to low supersaturation (S = 6.3) where the aqueous species are dominant. The peak width of the spectrum becomes narrower with increasing reaction time, indicating the progress of curium incorporation and the diminution of the contribution of aqueous species to the overall fluorescence spectrum. Different charge compensation mechanisms occurring when Cm(III) is incorporated in strontianite during homogeneous nucleation may also explain the decrease of the peak width with time. In fact, during the subsequent recrystallization of the precipitates, some charge compensation mechanisms may be suppressed and only one compensation mechanism favored, leading to the same coordination environment for all incorporated Cm(III) atoms and subsequently to the reduction of the peak width. This is further supported by the spectra recorded with different delay after the excitation (Figure 59), where small differences are observed in the peak width for a reaction time of 68 min, whereas the spectra recorded with different delays are totally identical after a reaction time of 144 h. The measured lifetime of 482 ± 7 µs (144h - 12 days of reaction time) correspond to 0.5 ± 0.1 water molecules in the first coordination sphere of Cm(III).

Eu-ESN-strontianite

Interactions of Eu(III) with the ESN of strontianite was carried out at supersaturations S = 6.3 and S = 1000, respectively. The corresponding speciation diagram is shown in Figure 56. At S = 6.3, no changes are observed in the fluorescence emission spectra over the observation period of 36 hours (Figure 60, left). The spectra recorded with different delays (1 and 250 µs) after the excitation suggest the existence of a single species within the first 6 h of reaction time. The amount of Eu- ESN formed is insignificant compared to the Eu(III) aqueous species, for this reason, both the emission spectra and the fluorescence lifetime are dominated by the aqueous Eu(III) species. However, after a reaction time of 36 hours, the spectrum recorded with different delays (1 µs vs. 250 µs) clearly indicates the formation of an additional species (Figure 61, left), which is thought to be the Eu(III) incorporation into strontianite.

For the experiment at S = 1000, the formation of Eu(III) strontianite species is observed already after a reaction time of 5 min (Figure 60, right). With the reaction time increasing, the spectrum becomes well defined, indicating the increase of Eu(III)-strontianite species at the expense of Eu(III)-aqueous species. The spectra recorded with different delays after excitation, and the lifetime measurement (Figure 61, right) clearly show the formation of a second species with longer lifetime (615 ± 56 µs). Using the Horrock's equation (30), the number of water molecules in the first coordination sphere of

this species is estimated to be 1.1 ± 0.2, suggesting the presence of an inner sphere complex. The lifetime of 145 ± 6 µs corresponds to the aqueous europium species.

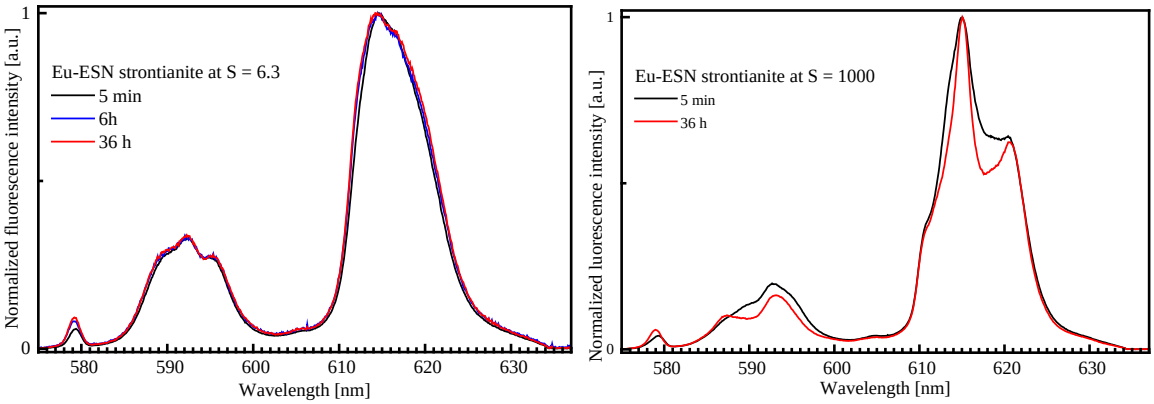

Figure 60. Fluorescence emission spectra of Eu(III) in solutions supersaturated with respect to strontianite. The spectra are plotted as a function of time. Experimental conditions: ionic strength = 0.1 mol·kg^{-1}; pH = 10; Left: S = 6.3; $[CO_3^{2-}]_{TOT}$ = 2.5·10^{-4} M; Right: $[CO_3^{2-}]_{TOT}$ = 2.5·10^{-4} M.

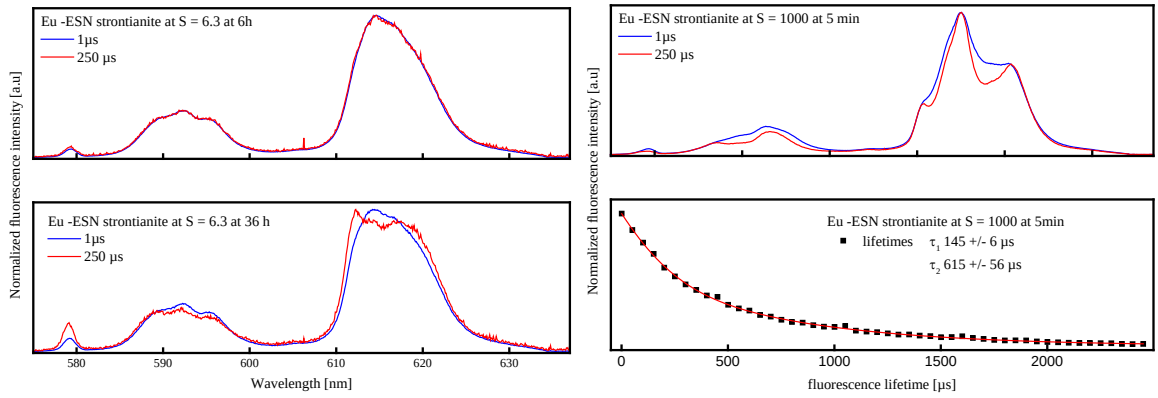

Figure 61. Fluorescence emission spectra recorded with different delays (1 µs vs. 250 µs) after the excitation. Left: S = 6.3. Right: S = 1000. Experimental conditions are given in the caption of Figure 60.

4.3.3 Uptake of trivalent curium and europium in MFR experiments

Cm^{3+} and Eu^{3+} uptake during the growth of celestite or strontianite was carried out in MFR according to the procedure described in chapter 3.2.4.

4.3.3.1 Uptake by celestite

Europium-celestite

The uptake of Eu(III) in celestite was investigated at an initial supersaturation ratio S = 8.9, corresponding to a crystal growth rate of $2.97 \pm 0.4 \cdot 10^{-7}$ mol·m^{2}·s^{-1}. The europium concentration was $1.26 \cdot 10^{-7}$ mol·l^{-1} and the amount of europium uptake was quantified to be 36 ± 5 %. As comparison, using a $4.5 \cdot 10^{-7}$ mol·l^{-1} europium solution, Holliday et al. [6] have reported that less than 5 % of europium is associated with celestite at a supersaturation ratio S = 6 with respect to celestite. Contrary to the previous study by Holliday et al. [6], a quantification of the europium uptake by celestite was possible in the present study due to the lower initial europium concentration used (see Table 7). TRLFS measurements on the sample at the end of MFR-experiments are shown in Figure 62.

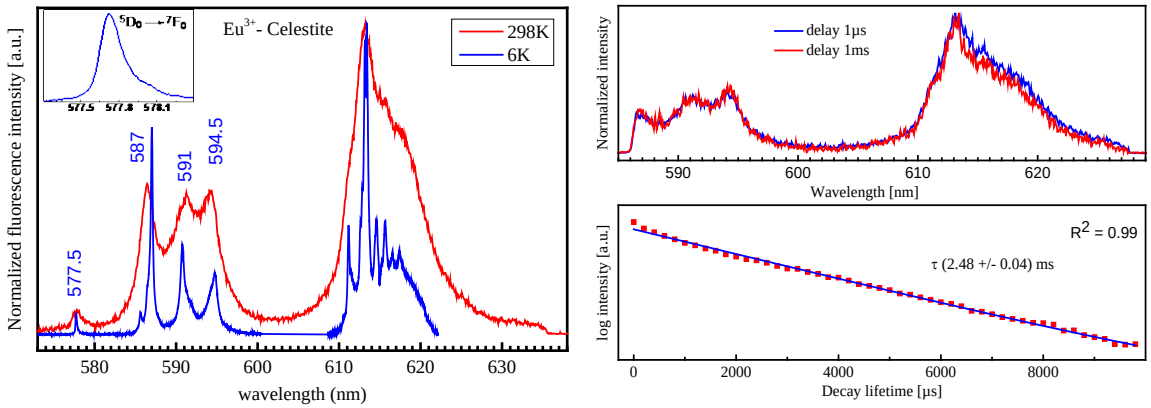

Figure 62. TRLFS measurements of a Eu^{3+}-celestite sample. Left: fluorescence emission spectra recorded at two different temperatures using a 1200 l/mm grating. The number of peaks in the $^{5}D_0 \rightarrow {}^{7}F_0$ transition (zoom-in) correlate with the total number of species present in a sample. Right: The upper spectrum shows the fluorescence emission recorded at two different delay times at room temperature; the lower spectrum shows the fluorescence decay measured at room temperature.

The fluorescence emission spectrum taken at 6 K is highly resolved (due to the suppression of vibronic transitions at low temperature), as compared to the spectrum at room temperature. Contrary to the lifetime of 285 ± 479 µs determined for the Eu-ESN sample, which only indicated the hypothetical presence of a species with longer lifetime, the fluorescence lifetime of 2.4 ms determined for the Eu-celestite in MFR experiments indicates an incorporation of Eu(III) into the crystal lattice. The fluorescence lifetime increased slightly to 2.9 ms upon cooling the sample at 6 K. The $^{5}D_0 \rightarrow {}^{7}F_0$ transition (577.5 nm) is not split suggesting the existence of a single species. This hypothesis of a single species is further supported by the spectra recorded at different delay times

after excitation as well as by the mono-exponential decay of the fluorescence lifetime. Contrary, the multiplets of the $^5D_0 \rightarrow {}^7F_1$ (587 – 595 nm) and $^5D_0 \rightarrow {}^7F_2$ (611-618 nm) transitions seem to be split more than threefold and fivefold, respectively, as expected for a single species. Also the non-symmetric shape of the $^7F_0$ band may be a hint to the existence of an additional species, or a slight variation in the near-field of incorporated Eu(III). This "additional" species may be a minor component with similar emission spectrum and lifetime as the "major" species. This can play an important role when charge compensation processes occur in the system: Substitution of matrix ions by foreign ions of different charge (in the present case substitution of Sr^{2+} by Eu^{3+}) requires compensation of the excess charge. The fundamental mechanisms providing local charge compensation have been discussed in chapter 2.5.

Curium-celestite

The uptake of Cm(III) by celestite was carried out under the same conditions as the Eu(III) uptake ($S_{initial}$ = 8.9; R_G = 2.97 ± 0.4·10^{-7} mol·m^{-2}·s^{-1}). However, the Cm(III) concentration was set to be 6.42·10^{-10} M. Results of the TRLFS measurements at the end of the experiment by using seed crystals are shown in Figure 63.

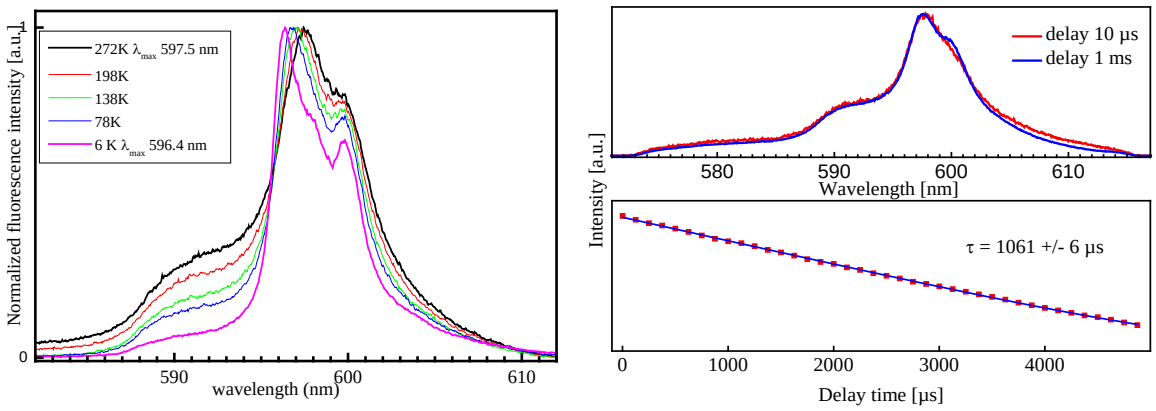

Figure 63. Fluorescence emission spectrum of Cm(III)-celestite at different temperatures (left) and the corresponding fluorescence lifetime after excitation at 396.6 nm (right). The spectra at different delay times as well as the fluorescence lifetime measurement were carried out at 298 K. All spectra were recorded using a 1200 l/mm grating.

The emission spectrum of Cm(III) incorporated in celestite shows peaks at 596.3 (maximum) and 600 nm. In comparison with the Cm(III) aquo ion (593.8 nm), the small bathochromic shift indicates weak interactions of Cm(III) with sulfate. The band at ~ 591 nm is a hot band, since the fluorescence intensity of this transition decreases when the temperature of the sample decreases. During the

cooling of the sample, a blue shift of the peak maximum is observed. Such a blue-shift was not observed during the cooling of the Eu(III)-celestite sample, although Cm^{3+} (111 pm) and Eu^{3+} (108.7 pm) are comparable ionic radii. It is thought that some structural changes occurs during the cooling of the Cm(III)-celestite sample, leading to a weakening of the crystal field, what gives rise to the shifting of the emission spectrum towards lower wavelengths. The fluorescence spectra at different delay time perfectly overlap (Figure 63, right), suggesting the presence of a single Cm(III) species. The fluorescence lifetime show a mono-exponential decay proving the presence of only a single Cm(III) species. The lifetime of 1.1 ms clearly indicates a loss of the hydration sphere and proves that Cm(III) is incorporated into the bulk of the crystals. This is consistent with the data obtained from the interactions of Cm(III) with the ESN of celestite (Figure 55) as well as with the investigations of Holliday et al. [6].

4.3.3.2 Uptake by strontianite

Europium strontianite

The uptake of europium by strontianite in mixed flow reactor experiments was carried out at supersaturation ratios of 8.9 and 1000, corresponding to crystal growth rates $R_G = 8.7 \pm 0.4 \cdot 10^{-9}$ and $2.3 \pm 0.3 \cdot 10^{-7}$ $mol \cdot m^{-2} \cdot s^{-1}$, respectively. The Eu(III) concentration in the inlet solution was $1.26 \cdot 10^{-7}$ $mol \cdot l^{-1}$. For both supersaturation ratios, more than 99.9 % of europium uptake was observed. The fluorescence spectrum and lifetime are shown in Figure 64.

The data from fluorescence spectroscopy at room temperature suggest the existence of two Eu(III)-strontianite species with lifetimes of 580 ± 22 µs (667 ± 48 µs at S =1000) and 1720 ± 23 µs (1592 ± 33 µs at S = 1000). The number of coordinated water molecules calculated using the Horrock's equation are 1.1 ± 0.1 for the species with shorter lifetime, indicating a sorption of europium onto the surface of the seed crystal via an inner sphere complex, losing part of his hydration sphere. For the second species with a longer lifetime, europium incorporation in the crystal structure of strontianite with a complete loss of its hydration sphere could explain the spectroscopic observations. The $^7F_0$ band at low temperature and different delays also confirms the existence of two species (

Annex 20). In the experiment with ESN of strontianite, only the inner-sphere complexation was observed, and the incorporation of Eu(III) into the bulk crystal with total loss of the hydration sphere was not observed.

Previous studies by Holliday et al.[6] were carried out at a supersaturation ratio S = 3311 with respect to strontianite and an Eu(III) concentration of $4.5 \cdot 10^{-7}$ $mol \cdot l^{-1}$. The authors have reported the formation of only one species with a fluorescence lifetime of 1.6 ms, which is comparable to the species with the longer lifetime observed in the present study. The species with the shorter lifetime

reported here was not observed. Also for the isostructural aragonite, only one Eu(III) species (europium concentration $6 \cdot 10^{-7}$ mol·l^{-1}) with a lifetime of 1.16 ms was identified to form from co-precipitation experiments in MFR [212]. From the data determined in this thesis for the precipitation of strontianite in MFR-experiments, a precipitation rate of 94pprox.. $3.8 \cdot 10^{-7}$ mol·m^{-2}·s^{-1} is estimated for the experimental conditions of Holliday et al. [6] at S = 3311. As comparison, the precipitation rates at S = 8.9 and S = 1000 are $8.7 \cdot 10^{-9}$ mol·m^{-2}·s^{-1}and $2.3 \cdot 10^{-7}$ mol·m^{-2}·s^{-1}, respectively. It has been mentioned in chapter 2.5 that trace element partitioning into a host mineral may be dependent on the growth rate of the mineral. The difference observed between the literature data [6] and the data in this thesis are not well understood so far. However, they may be due to the dependency of the trace element uptake on the crystal growth kinetics: the surface reaction kinetic model might be valid for the supersaturation range investigated in this thesis, whereas the growth surface entrapment model is operative at much higher supersaturation ratio (S >> 1000), as it is the case for the literature data.

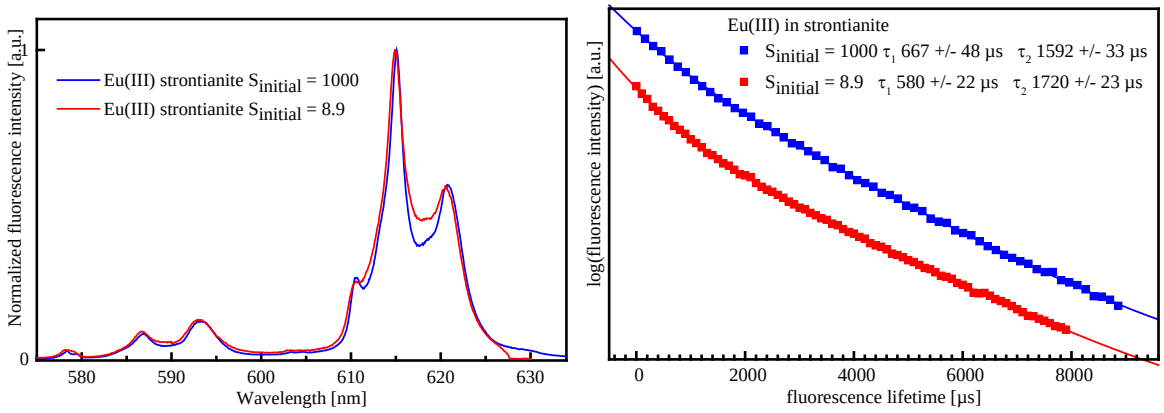

Figure 64. Left: Fluorescence emission spectrum of Eu(III) strontianite (S = 8.9) recorded with a grating of 1200 lines·mm^{-1}. Right: fluorescence lifetimes showing a bi-exponential decay. All measurements were carried out at 298 K.

Curium-strontianite

Similarly to the case of Eu^{3+}-strontianite, the co-precipitation of Cm^{3+} with strontianite was also carried out at supersaturation ratios of 10 and 1000 with respect to strontianite. The Cm(III) concentration was $8.5 \cdot 10^{-10}$ mol·l^{-1} for each of the two supersaturation ratios. Here again, the solution supersaturation was found to have no influence on the speciation of the curium complexes formed. The data for S = 10 are shown in Figure 65, and are also representative for S = 1000 (see Annex 22). The emission spectra in Figure 65 were recorded at different gratings of the spectrometer (grating left: 1200 lines·mm^{-1}, grating right: 2400 lines·mm^{-1}), explaining the better resolved peak multiplicity in the upper right plot. The emission spectrum shows a hot band at 605 nm. The intensity

of this hot band decreases with sample cooling and does not completely disappears after several hours at 6 K as expected from theoretical considerations. This might indicate the existence of a temperature gradient in the cryostat chamber with the sample being few Kelvin warmer than the thermo-element contact point with the sample holder. Emission spectra recorded with different delay times after the excitation show clearly the existence of a single species with a lifetime of 606 ± 5 µs, corresponding to 0.2 ± 0.1 molecules water in the first coordination sphere. This species can therefore be considered as incorporated into the bulk crystal. Holiday et al. have also reported only one Cm(III) strontianite species with a lifetime of 470 µs for co-precipitation experiments in MFR (Literature: S = 3311, [Cm(III)] = $2.4 \cdot 10^{-8}$ mol·l^{-1}; This study: S ≤ 1000, [Cm(III)] = $8.5 \cdot 10^{-10}$ mol·l^{-1}).

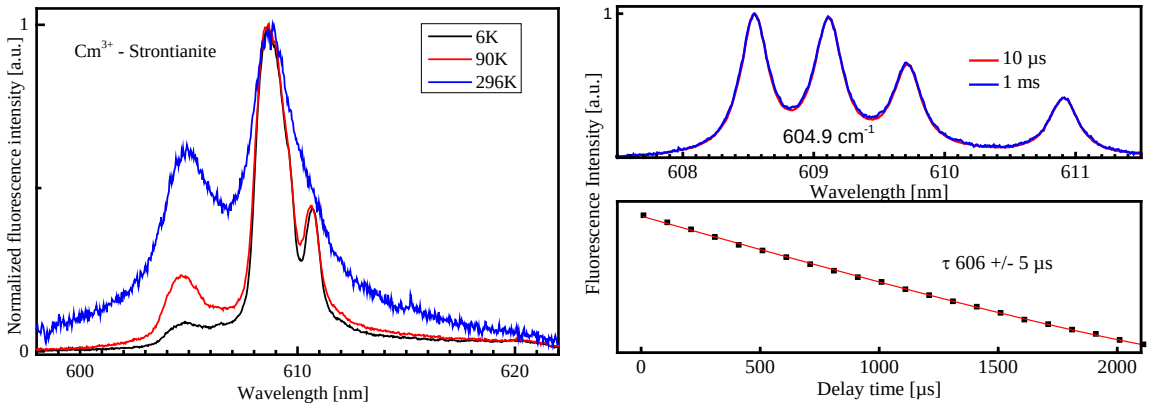

Figure 65. Left: fluorescence emission spectra of Cm(III) strontianite at three different temperatures. The spectra were recorded with a grating of 1200 lines·mm^{-1}. Upper right: fluorescence emission spectra are recorded with a grating of 2400 lines·mm^{-1}at 6 K and at different delay times after excitation. The fourfold splitting of the ground state (Kramer doublet) is highlighted. Lower right: the mono-exponential decay of the fluorescence lifetime suggests the existence of only one species. $S_{strontianite}$ = 10; [Cm(III)] = $8.5 \cdot 10^{-10}$ mol·l^{-1}; ionic strength = 0.1 mol·kg^{-1}.

The observations made in the Cm-strontianite system are not in agreement with the two species observed in the Eu-strontianite system. Even for both Cm(III) and Eu(III) experiments carried out at a supersaturation ratio S = 1000 with respect to strontianite, the results obtained are not similar. Therefore, we can assume that the solid species formation is not determined by the solution supersaturation alone. Nevertheless, the Cm(III) concentration ($8.5 \cdot 10^{-10}$ mol·l^{-1}) was much lower than the Eu(III) concentration ($1.26 \cdot 10^{-7}$ mol·l^{-1}). For this reason, the Eu(III)-celestite species with shorter lifetime may also result from concentration quenching. Energy transfer processes which are negligible in minerals with low dopant (Cm/Eu) concentration become more important above certain dopant ion density. Because of the high europium concentration, the dipole-dipole interactions

depending on the distance between the europium ions in the host mineral become significant, leading to a shortening of the lifetimes [213]. This may explain the existence of a second species (τ = 667 µs) in the Eu(III)-strontianite sample, since more than 99,9 % of the dopant ions are taken up by strontianite. Surprisingly, Holliday et al. [6] and Schmidt et al. [212] using higher europium concentrations reported only one Eu incorporation species in strontianite and aragonite, respectively. In order to verify if the occurrence of two species in the Eu(III) strontianite system is related to the relatively high concentration of the dopant ion ([Eu(III) = $1.26 \cdot 10^{-7}$ mol·l^{-1}]), an additional experiment was carried out with curium ($6 \cdot 10^{-8}$ mol·l^{-1}spiked with an additional trivalent lanthanide with no fluorescence (Gd^{3+}, $1.25 \cdot 10^{-7}$ mol·l^{-1}) resulting in the same total concentration as for the Eu (III) experiment. This solution was then used to investigate the uptake of trivalent elements in MFR experiments. Results of the TRLFS measurement are shown in Figure 66.

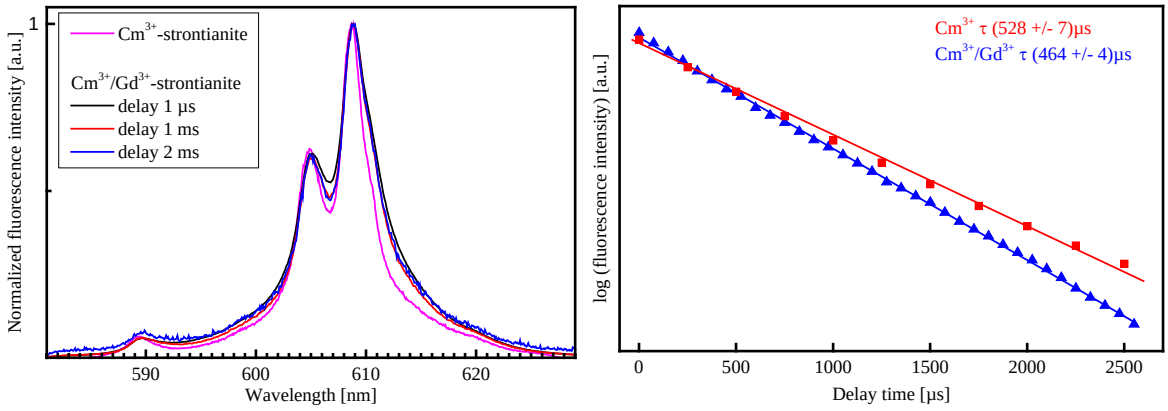

Figure 66. Comparison of the fluorescence emission spectra (left) and fluorescence lifetimes (right) for the systems Cm^{3+}-strontianite and Cm/Gd-strontianite. The supersaturation ratio of the both solutions was S = 8.9. Spectra were recorded at 298 K.

The results (Figure 66) show that even at relatively high concentration of the trivalent elements, only one species is formed. The lifetime of ~ 464 µs corresponds to 0.5 ± 0.1 molecules water in the first coordination sphere of curium and suggests its incorporation into the bulk crystal. Since gadolinium is a non-fluorescent dopant, concentration quenching cannot occur.

Table 7. Selected data relative to the uptake of Eu(III) and Cm(III) in MFR-experiments

	S	R_G [mol·m^{-2}·s^{-1}]	Eu(III) nM	Cm(III) nM	Gd(III) nM	Uptake %	τ_1 ms	τ_2 ms
$SrSO_4$	8.9	$3.0 \pm 0.4 \cdot 10^{-7}$	126	0	0	36 ± 5	2.5	-

$SrSO_4$	8.9	$3.0 \pm 0.4 \cdot 10^{-7}$	0	64	0	-[12]	1.1	-
$SrCO_3$	8.9	$8.7 \pm 0.4 \cdot 10^{-9}$	126	0	0	99.9 %	0.6	1.7
$SrCO_3$	1000	$2.3 \pm 0.3 \cdot 10^{-7}$	126	0	0	99.9 %	0.7	1.6
$SrCO_3$	10	$9.8 \pm 0.4 \cdot 10^{-9}$	0	0.85	0	-	0.5	
$SrCO_3$	1000	$2.3 \pm 0.3 \cdot 10^{-7}$	0	0.85	0	-	0.5	-
$SrCO_3$	10	$9.8 \pm 0.4 \cdot 10^{-9}$	0	0.85	125	-	0.5	-

[12] Uptake quantification was not investigated since experiments with curium were carried out mostly for fluorescence spectroscopic purposes.

5 Conclusions

In this thesis, Laser Induced Breakdown Detection (LIBD) was successfully applied for the first time for kinetics studies, precisely for the determination of induction periods for the nucleation of celestite and strontianite from supersaturation solutions. Due to the high sensitivity of the LIBD method to detect nanoparticles, it could be shown that early stage nuclei are formed immediately with the creation of supersaturation and remain in the solution throughout the induction period. Transmission electron microscopy has revealed that early stage nuclei are well crystalline in the case of celestite, whereas the early stage nuclei of strontianite seem to be unstable upon solution quenching.

In mixed flow reactor experiments, the rate constants and other empirical parameters determined for the crystal growth of celestite and strontianite are important parameters used in reactive transport modelling. For example, the simulation program TOUGHREACT [201, 214] uses a parameter that has been deduced from dissolution experiments to predict the precipitation of celestite. The data determined in this thesis are more accurate for such simulations. The different kinetic parameters determined in this thesis can further be implemented in different geochemical modelling codes to predict the porosity clogging of the host rock in deep geological repositories for nuclear wastes. The porosity clogging can cause an accumulation of gases in the repository, leading possibly to the failure of the barrier system.

TRLFS studies have shown that both europium and curium can be incorporated in the bulk crystals of celestite and strontianite. An additional species (inner-sphere sorption) was observed during the uptake of europium by strontianite. The main experimental results obtained in this thesis are listed below.

Nucleation of $SrSO_4$ and $SrCO_3$

- The formation of the first nuclei, referred to in this thesis as "*early stage nuclei*" (ESN), occurs almost simultaneously with the mixing of the reagents and thus with the creation of supersaturation. TEM observations have revealed that the ESN of celestite are well crystalline, with the average crystal size ranging from about 5 - 10 nm (width) to 50 – 100 nm (length). ESN of strontianite were observed in LIDB-experiments, but attempts to visualize them in TEM-experiments were unsuccessful, most probably due to their instability during the sample preparation for TEM.
- After the formation of the ESN and often for a considerable time afterwards, no significant changes may be detected in the solution until, at a point referred to as the induction time

(t_{Ind}), particles growth starts. The induction time for the nucleation of celestite and strontianite was determined using the highly sensitive LIBD method. Results are summarized below:

- *Effect of supersaturation on the induction time:* the induction time decreases as the supersaturation increases. For solutions with 0.1 $mol \cdot kg^{-1}$ NaCl ionic strength at constant temperature of 295 K, the induction time for the nucleation of celestite varies from 5 min at S = 31.6 to approx. 1305 min at S = 2.5. Accordingly, the induction time for the nucleation of strontianite varies from 25 min at S = 31.6 to 540 min at S = 7.9.
- *Critical supersaturation:* the critical supersaturation ratio S_{crit} for the nucleation is the maximum supersaturation that a metastable supersaturated solution can endure without nucleating a detectable amount of a new phase. Within the chosen maximum observation period of 40 h for LIDB-experiments in this thesis, critical supersaturation ratios S_{crit} of 2 and 6.3 were determined for celestite and strontianite, respectively.
- *Interfacial tension:* for the supersaturation range where homogeneous nucleation prevails, interfacial tension between the surface of the nucleus and the bulk solution was determined to be 22.6 and 31.5 $mJ \cdot m^{-2}$ for celestite and strontianite, respectively.
- *Effect of temperature on the induction time*: the induction time for the nucleation of $SrSO_4$ and $SrCO_3$ decreases with increasing temperature. Activation energies of 45.5 (celestite) and 55.2 $kJ \cdot mol^{-1}$ (strontianite) were determined from an Arrhenius-like plot.
- *Effect of ionic strength:* the ionic strength of the solutions was adjusted between 0.1 and 2.0 $mol \cdot kg^{-1}$ using NaCl. With the increasing ionic strength, the amount of impurities in the solution increases. Primary heterogeneous nucleation is known to be favored in the presence of impurities. In the present thesis, the effect of the ionic strength on the induction time for the nucleation were investigated in two different ways:
  a) For the celestite samples, the solute concentration was increased with increasing ionic strength to maintain a constant supersaturation. A decrease of the induction time with the increasing ionic strength was observed.
  b) For the strontianite samples, the solute concentration was kept constant. With the increasing ionic strength, the supersaturation of the solution decreased and thus the induction time increased.

- *Effect of dissolved silica and glass beads:* additives can act as nucleation inhibitor (dissolved silica) or as catalyst (glass beads). In the present thesis, the addition of dissolved silica to supersaturated solutions ($S_{celestite}$ = 12.6, $S_{strontianite}$ = 31.6) was found to cause an increase of the induction time for both celestite and strontianite. For the silica concentration up to 8 ppm, the induction time for the nucleation of celestite increased continuously (from 25 min in the absence of silica to 1500 min at a silica concentration of 7.7 ppm). The increase of the induction time for the nucleation of strontianite was less pronounced (from 19 min in the absence of silica to ~ 57 min at a silica concentration of 0.8 ppm). It was observed only at a silica concentration up to 0.8 ppm; further increase of the silica concentration (up to 8 ppm) had a negligible impact on the induction time. In the presence of glass beads as heterogeneous seeding material, the induction time decreases with the increasing amount of glass beads.

Determination of crystal growth rates from MFR experiments

The influence of supersaturation, reactive surface area, temperature and ionic strength on the kinetics of crystal growth of celestite and strontianite was investigated in MFR experiments.

- The rate of crystal growth increases with increasing supersaturation and increasing surface area of the seed crystals. At relative supersaturations S - 1 ≤ 30 for celestite and S - 1 ≤ 50 for strontianite, crystal growth seems to be controlled by surface reactions. With increasing supersaturation, the contribution of primary homogeneous nucleation to the overall rate of crystal growth becomes more and more important. Following rate constants and empirical parameters were determined for the supersaturation range where the growth by surface reactions prevails:
  - Strontianite: $k = 1.27 \pm 0.12 \cdot 10^{-9}$ mol·m^{-2}·s^{-1}; $m = 0.78$; $n = 1.19$
  - Celestite: $k = 9.24 \pm 0.75 \cdot 10^{-8}$ mol·m^{-2}·s^{-1}; $m = 0.52$; $n = 1.78$
- The temperature dependence of the crystal growth kinetics was investigated at temperatures from 278 to 338 K. In general, the rates of crystal growth increase with increasing temperature. From the Arrhenius plot of the growth rate constants as a function of the temperature, activation energies (E_a) for the crystal growth of celestite and strontianite were determined:
  - $E_a = 17.8 \pm 0.8$ kJ·mol^{-1} for celestite
  - $E_a = 35.7 \pm 0.1$ kJ·mol^{-1} for strontianite

- The effect of the ionic strength: the solute concentration was increased with increasing ionic strength in order to maintain a constant supersaturation ratio with respect to celestite. This resulted in an increase of the crystal growth rates by a factor of ~ 3 when the ionic strength was increased from 0.1 to 2.0 $mol \cdot kg^{-1}$.

TRLFS experiments

The co-precipitation of Eu^{3+} and Cm^{3+} with celestite and strontianite in primary homogeneous- and secondary nucleation experiments was investigated.

- The growth rates of celestite and strontianite were not influenced by the presence of europium and curium in the solution.
- For the uptake of trivalent europium and curium during the growth of celestite and strontianite in MFR-experiments, the following species are observed:
    - Eu-Celestite: one incorporated species with a lifetime τ = 2.5 ms
    - Cm-Celestite: one incorporated species with a lifetime τ = 1.1 ms
    - Eu-Strontianite: two species with τ = 0.6 ms and 1.7 ms, respectively
    - Cm-Strontianite: one species with a lifetime τ = 0.6 ms
- In primary homogeneous nucleation experiments, the complexation of the trivalent cations by the ESN of celestite and strontianite was studied. Results of the TRLFS measurements suggest that ESN form the same europium and curium species as the crystalline minerals. However, the fluorescence spectra at low supersaturations are dominated by the aqueous species, thus making difficult the observation of the Eu-ESN and Cm-ESN species. With increasing supersaturation, the quantity of ESN formed increases and the fluorescence emission spectra is dominated by the Eu-ESN and Cm-ESN species.

The experimental data determined in this work can be used as input parameters in reactive transport models, especially for the case where the migration of radionuclides through the geological formation can be impacted by the formation of secondary mineral phases.

6 References

(1) Dobrev, D.; Polivka, P.; Vecernik, P.; Vokal, A., Generation and migration of hydrogen in nuclear waste repositories. 2012.

(2) Ojovan, M. I., *Handbook of Advanced Radioactive Waste Conditioning Technologies*. ed.; Elsevier Science: 2011.

(3) Moyce, E. B. A.; Rochelle, C.; Morris, K.; Milodowski, A. E.; Chen, X.; Thornton, S.; Small, J. S.; Shaw, S., Rock alteration in alkaline cement waters over 15 years and its relevance to the geological disposal of nuclear waste. *Applied Geochemistry* 2014, 50, (0), 91-105.

(4) Gaucher, E. C.; Tournassat, C.; Pearson, F. J.; Blanc, P.; Crouzet, C.; Lerouge, C.; Altmann, S., A robust model for pore-water chemistry of clayrock. *Geochimica Et Cosmochimica Acta* 2009, 73, (21), 6470-6487.

(5) Chagneau, A.; Tournassat, C.; Steefel, C. I.; Bourg, I. C.; Gaboreau, S.; Esteve, I.; Kupcik, T.; Claret, F.; Schäfer, T., Complete Restriction of 36Cl– Diffusion by Celestite Precipitation in Densely Compacted Illite. *Environmental Science & Technology Letters* 2015, 2, (5), 139-143.

(6) Holliday, K.; Chagneau, A.; Schmidt, M.; Claret, F.; Schaefer, T.; Stumpf, T., Discriminating factors affecting incorporation: comparison of the fate of Eu3+-Cm3+ in the Sr carbonate-sulfate system. *Dalton Transactions* 2012, 41, (13), 3642-3647.

(7) Xu, T.; Senger, R.; Finsterle, S., Corrosion-induced gas generation in a nuclear waste repository: Reactive geochemistry and multiphase flow effects. *Applied Geochemistry* 2008, 23, (12), 3423-3433.

(8) Mobbs, S. F.; Charles, C. E.; Delow, *Performance Assessment of Geological Isolation Systems for Radioactive Waste: Disposal into the Sub-Seabed EUR 11779*. ed.; 1988.

(9) Sjoeblom, K. L.; Linsley, G. S., Sea disposal of radioactive wastes: the London Dumping Convention 1972. *International Atomic Energy Agency* 1994, Bulletin 2.

(10) Miller, W.; Alexander, R.; Chapman, N.; McKinley, J. C.; Smellie, J., *Geological disposal of radioactive wastes and natural analogues*. ed.; Elsevier: 2000; Vol. 2.

(11) Nagra, Kristallin-1, Safety assessment report. *Kristallin-1, Safety assessment report. Nagra technical report series NTB* 1994, 93-22.

(12) Mazurek, M.; Alt-Epping, P.; Bath, A.; Gimmi, T.; Niklaus Waber, H.; Buschaert, S.; Cannière, P. D.; Craen, M. D.; Gautschi, A.; Savoye, S.; Vinsot, A.; Wemaere, I.; Wouters, L., Natural tracer profiles across argillaceous formations. *Applied Geochemistry* 2011, 26, (7), 1035-1064.

(13) Veres, Á., Chapter 10.2 Environmental problems. *Interface Science and Technology* 2004, Volume 3, 359-404.

(14) OECD/NEA, *Considering Timescales in the Post-closure Safety of Geological Disposal of Radioactive Waste*. ed.; OECD Publishing.

(15) Leite, E. R.; Ribeiro, C., *Crystallization and growth of colloidal nanocrystals*. ed.; Springer Science & Business Media: 2011.

(16) IAEA, *(2001) The Use of Scientific and Technical Results from Underground Research Laboratory Investigations for the Geological Disposal of Radioactive Waste* 2001, IAEA-TECDOC-1243

(17) Altmann, S., *Fundamental Processes of Radionuclide Migration, FUNMIG Workshop Proceedings, (Ed. Buckau G et al.) Forschungszentrum Karlsruhe. Wissenschaftliche Berichte FZKA 7461, 45 – 82* 2009.

(18) Lázár, K.; Máthé, Z., *Claystone as a Potential Host Rock for Nuclear Waste Storage*. ed.; 2012.

(19) Sammartino, S.; Bouchet, A.; Prêt, D.; Parneix, J. C.; Tevissen, E., Spatial distribution of porosity and minerals in clay rocks from the Callovo-Oxfordian formation (Meuse/Haute-Marne, Eastern France)—implications on ionic species diffusion and rock sorption capability. *Applied Clay Science* 2003, 23, (1–4), 157-166.

(20) Leroy, P.; Revil, A.; Altmann, S.; Tournassat, C., Modeling the composition of the pore water in a clay-rock geological formation (Callovo-Oxfordian, France). *Geochimica Et Cosmochimica Acta* 2007, 71, (5), 1087-1097.

(21) Grangeon, S.; Vinsot, A.; Tournassat, C.; Lerouge, C.; Giffaut, E.; Heck, S.; Groschopf, N.; Denecke, M. A.; Wechner, S.; Schäfer, T., The influence of natural trace element distribution on the mobility of radionuclides. The exemple of nickel in a clay-rock. *Applied Geochemistry* 2015, 52, 155-173.

(22) Tournassat, C.; Steefel, C. I.; Bourg, I. C.; Bergaya, F., *Natural and Engineered Clay Barriers*. ed.; Elsevier Science: 2015.

(23) Booth, H. S.; Pollard, E. F., Reactions in Inert Fused Substances: Conversion of Celestile to Strontium Carbonate. *Industrial & Engineering Chemistry* 1948, 40, (10), 1986-1988.

(24) Kobe, K. A.; Deiglmeier, N. J., Strontium Carbonate : conversion from strontium sulfate by metathesis with alkali carbonate solution. *Industrial & Engineering Chemistry* 1943, 35, (3), 323-325.

(25) Lerouge, C.; Gaucher, E. C.; Tournassat, C.; Negrel, P.; Crouzet, C.; Guerrot, C.; Gautier, A.; Michel, P.; Vinsot, A.; Buschaert, S., Strontium distribution and origins in a natural clayey formation (Callovian-Oxfordian, Paris Basin, France): A new sequential extraction procedure. *Geochimica Et Cosmochimica Acta* 2010, 74, (10), 2926-2942.

(26) Gaucher, E.; Robelin, C.; Matray, J. M.; Négrel, G.; Gros, Y.; Heitz, J. F.; Vinsot, A.; Rebours, H.; Cassagnabère, A.; Bouchet, A., ANDRA underground research laboratory: interpretation of the mineralogical and geochemical data acquired in the Callovian–Oxfordian formation by investigative drilling. *Physics and Chemistry of the Earth, Parts A/B/C* 2004, 29, (1), 55-77.

(27) Savage, D.; Walker, C.; Arthur, R.; Rochelle, C.; Chie, O., Alteration of bentonite by hyper alkaline fluids: the role of secondary minerals. 2005.

(28) Adam, C., On the medicinal properties of the muriated barytes. *Medical Communications (London)* 1790, 2, 60.

(29) Murray, T., Elementary Scots. The discovery of Strontium. *Scott Med J* 1993, 38, (6), 188-9.

(30) Hope, T. C., I. Account of a Mineral from Strontian, and of a peculiar Species of Earth which it contains. *Earth and Environmental Science Transactions of the Royal Society of Edinburgh* 1798, 4, (02), 3-39.

(31) Davy, H., Electro-Chemical Researches, on the Decomposition of the Earths; With Observations on the Metals Obtained from the Alkaline Earths, and on the Amalgam Procured from Ammonia. *Philosophical Transactions of the Royal Society of London* 1808, 98, (ArticleType: research-article / Full publication date: 1808 /), 333-370.

(32) Weeks, M. E., The discovery of the elements. X. The alkaline earth metals and magnesium and cadmium. *Journal of Chemical Education* 1932, 9, (6), 1046.

(33) Partington, J. R., The early history of strontium. *Annals of Science* 1942, 5, (2), 157-166.

(34) MacMillan, J. P.; Park, J. W.; Gerstenberg, R.; Wagner, H.; Köhler, K.; Wallbrecht, P., Strontium and Strontium Compounds. *Ullmann's Encyclopedia of Industrial Chemistry* 2000.

(35) Driessens, F. C. M.; Verbeeck, R. M. H., *Biominerals*. ed.; CRC Press: Boca Raton, 1990.

(36) West, I., Vanished Evaporites- Significance of strontium minerals. *Journal of Sedimentary Petrology* 1973, 43, (1), 2.

(37) Luttge, A.; Arvidson, R. S.; Fischer, C., A Stochastic Treatment of Crystal Dissolution Kinetics. *Elements* 2013, 9, (3), 183-188.

(38) Daval D; Pollet-Villard M; Ackerer P; Fritz B; Rémusat L; Guyot F; Bernard S; G, S.; K, K., Microstructural Modifications of Dissolving Silicate Minerals: Why Should We Bother? *Goldschmidt* 2015.

(39) Fogler, H. S., *Elements of chemical reaction engineering*. ed.; Prentice-Hall: 1986.

(40) Ben Simon, R.; Thiry, M.; Schmitt, J.-M.; Lagneau, V.; Langlais, V.; Bélières, M., Kinetic reactive transport modelling of column tests for uranium In Situ Recovery (ISR) mining. *Applied Geochemistry* 2014, 51, (0), 116-129.

(41) Johnson, J. W.; Nitao, J. J.; Knauss, K. G., Reactive transport modeling of CO2 storage in saline aquifers to elucidate fundamental processes, trapping mechanisms and sequestration partitioning. *Geological storage of carbon dioxide* 2004, 233, 107-128.

(42) Chagneau, A.; Claret, F.; Enzmann, F.; Kersten, M.; Heck, S.; Madé, B.; Schäfer, T., Mineral Precipitation-induced porosity reduction and its Effect on Transport Parameters in Diffusion-controlled Porous Media *Geochemical Transactions* 2015, In Press.

(43) Mullin, J. W., Crystallization *Crystallization (Fourth Edition)* 2001, 181-215.

(44) Becker, R.; Döring, W., Kinetische Behandlung der Keimbildung in übersättigten Dämpfen. *Annalen der Physik* 1935, 416, (8), 719-752.

(45) Gibbs, J. W., Yale University Press, New haven. *Thermodynamics, Collected Works* 1948, Vol I.

(46) Volmer, M., Kinetik der Phasenbildung. *Angewandte Chemie* 1939, 52, (30), 503-504.

(47) Benning, L. G.; Waychunas, G. A., Nucleation, Growth, and Aggregation of Mineral Phases: Mechanisms and Kinetic Controls. *Kinetics of Water-Rock Interaction* 2008, 259-333.

(48) Brantley, S. L.; Kubicki, J. D.; White, A. F., Kinetics of water-rock interaction. 2008.

(49) Ostwald, W., *Lehrbuch der allgemeinen Chemie*. ed.; Englemann: 1897; Vol. 2, p 444.

(50) Miers, H. A.; Isaac, F., The Spontaneous Crystallisation of Binary Mixtures. Experiments on Salol and Betol. *Proceedings of the Royal Society of London. Series A* 1907, 79, (531), 322-351.

(51) Miers, H. A.; Isaac, F., XLVII.-The refractive indices of crystallising solutions, with especial reference to the passage from the metastable to the labile condition. *Journal of the Chemical Society, Transactions* 1906, 89, (0), 413-454.

(52) Lasaga, A. C., *Kinetic Theory in the Earth Sciences. Princeton Series in Geochemistry*. ed.; 1998.

(53) Turnbull, D., Under what conditions can a glass be formed? *Contemporary Physics* 1969, 10, (5), 473-488.

(54) Podgornik, R., Book Review: Phase Transition Dynamics. Akira Onuki, 714 pp., Cambridge University Press, 2002. *Journal of Statistical Physics* 2003, 112, (1-2), 429-432.

(55) Debenedetti, P. G., *Metastable Liquids: Concepts and Principles.* ed.; Princeton University Press: 1996.

(56) Gibbs, J. W., *The collected works of J. Willard Gibbs* ed.; New York, 1928.

(57) Erdemir, D.; Lee, A. Y.; Myerson, A. S., Nucleation of Crystals from Solution: Classical and Two-Step Models. *Accounts of Chemical Research* 2009, 42, (5), 621-629.

(58) Teng, H. H., How Ions and Molecules Organize to Form Crystals. *Elements* 2013, 9, (3), 189-194.

(59) Volmer M.; Weber A., Keimbildung in übersättigten gebilden. *Zeitschrift für physikalische Chemie* 1925, 119, 25.

(60) Farkas L., Keimbildungsgeschwindigkeit in übersättigten Dämpfen. *Zeitschrift für physikalische Chemie* 1927, 125, 8.

(61) Zeldovich, J. B., On the theory of new phase formation, cavitation. *Acta Physicochimica URSS* 1943, 18, (1), 1-22.

(62) Christenson, H. K., Two-step crystal nucleation via capillary condensation. *CrystEngComm* 2013, 15, (11), 2030-2039.

(63) Reinhardt, A.; Doye, J. P. K., Free energy landscapes for homogeneous nucleation of ice for a monatomic water model. *Journal of Chemical Physics* 2012, 136, (5).

(64) Kretzschmar, R.; Schäfer, T., Metal retention and transport on colloidal particles in the environment. *Elements* 2005, 1, (4), 205-210.

(65) Filella, M.; Buffle, J., Factors controlling the stability of submicron colloids in natural waters. *Colloids and Surfaces A: Physicochemical and Engineering Aspects* 1993, 73, (0), 255-273.

(66) Yun, J.-I.; Kim, M.-A.; Panak, P. J.; Kim, J.-I.; Fanghänel, T., Formation of Aquatic Th(IV) Colloids and Stabilization by Interaction with Cm(III)/Eu(III). *The Journal of Physical Chemistry B* 2006, 110, (11), 5416-5422.

(67) Schäfer, T.; Huber, F.; Seher, H.; Missana, T.; Alonso, U.; Kumke, M.; Eidner, S.; Claret, F.; Enzmann, F., Nanoparticles and their influence on radionuclide mobility in deep geological formations. *Applied Geochemistry* 2012, 27, (2), 390-403.

(68) Geckeis, H.; Rabung, T.; Schäfer, T., Actinide-nanoparticle interaction: Generation, stability and mobility. *Actinide Nanoparticle Research* 2011, 1-30.

(69) Cölfen, H.; Mann, S., Higher-order organization by mesoscale self-assembly and transformation of hybrid nanostructures. *Angewandte Chemie-International Edition* 2003, 42, (21), 2350-2365.

(70) Jongen, N.; Bowen, P.; Lemaître, J.; Valmalette, J.-C.; Hofmann, H., Precipitation of Self-Organized Copper Oxalate Polycrystalline Particles in the Presence of Hydroxypropylmethylcellulose (HPMC): Control of Morphology. *Journal of Colloid and Interface Science* 2000, 226, (2), 189-198.

(71) Penn, R. L.; Banfield, J. F., Morphology development and crystal growth in nanocrystalline aggregates under hydrothermal conditions: insights from titania. *Geochimica Et Cosmochimica Acta* 1999, 63, (10), 1549-1557.

(72) Wang, T.; Cölfen, H.; Antonietti, M., Nonclassical Crystallization: Mesocrystals and Morphology Change of CaCO3 Crystals in the Presence of a Polyelectrolyte Additive. *Journal of the American Chemical Society* 2005, 127, (10), 3246-3247.

(73) Landau, L. D.; Lifshi͡ts, E. M., *Statistical physics, Part 1: Volume 5*. ed.; Butterworth-Heinemann: Boston, 2000.

(74) Sleutel, M.; Van Driessche, A. E. S., Role of clusters in nonclassical nucleation and growth of protein crystals. *Proceedings of the National Academy of Sciences of the United States of America* 2014, 111, (5), E546-E553.

(75) Gebauer, D.; Völkel, A.; Cölfen, H., Stable Prenucleation Calcium Carbonate Clusters. *Science* 2008, 322, (5909), 1819-1822.

(76) Pouget, E. M.; Bomans, P. H. H.; Goos, J. A. C. M.; Frederik, P. M.; de With, G.; Sommerdijk, N. A. J. M., The Initial Stages of Template-Controlled CaCO3 Formation Revealed by Cryo-TEM. *Science* 2009, 323, (5920), 1455-1458.

(77) Nudelman, F.; Sonmezler, E.; Bomans, P. H. H.; de With, G.; Sommerdijk, N. A. J. M., Stabilization of amorphous calcium carbonate by controlling its particle size. *Nanoscale* 2010, 2, (11), 2436-2439.

(78) Sear, R. P., The non-classical nucleation of crystals: microscopic mechanisms and applications to molecular crystals, ice and calcium carbonate. *International Materials Reviews* 2012, 57, (6), 328-356.

(79) Penn, R. L.; Banfield, J. F., Imperfect Oriented Attachment: Dislocation Generation in Defect-Free Nanocrystals. *Science* 1998, 281, (5379), 969-971.

(80) Niederberger, M.; Cölfen, H., Oriented attachment and mesocrystals: Non-classical crystallization mechanisms based on nanoparticle assembly. *Physical Chemistry Chemical Physics* 2006, 8, (28), 3271-3287.

(81) Verdoes, D.; Kashchiev, D.; van Rosmalen, G. M., Determination of nucleation and growth rates from induction times in seeded and unseeded precipitation of calcium carbonate. *Journal of Crystal Growth* 1992, 118, (3–4), 401-413.

(82) Tai, C. Y.; Chien, W.-C., Effects of operating variables on the induction period of CaCl2–Na2CO3 system. *Journal of Crystal Growth* 2002, 237–239, Part 3, (0), 2142-2147.

(83) Pokrovsky, O. S., Precipitation of calcium and magnesium carbonates from homogeneous supersaturated solutions. *Journal of Crystal Growth* 1998, 186, (1–2), 233-239.

(84) Söhnel, O.; Mullin, J. W., A method for the determination of precipitation induction periods. *Journal of Crystal Growth* 1978, 44, (4), 377-382.

(85) Myerson, A. S., *Handbook of industrial crystallization*. ed.; Butterworth-Heinemann: Boston, 2002.

(86) Söhnel, O.; Mullin, J. W., Precipitation of calcium carbonate. *Journal of Crystal Growth* 1982, 60, (2), 239-250.

(87) Golubev, S. V.; Pokrovsky, O. S.; Savenko, V. S., Unseeded precipitation of calcium and magnesium phosphates from modified seawater solutions. *Journal of Crystal Growth* 1999, 205, (3), 354-360.

(88) Golubev, S. V.; Pokrovsky, O. S.; Savenko, V. S., Homogeneous precipitation of magnesium phosphates from seawater solutions. *Journal of Crystal Growth* 2001, 223, (4), 550-556.

(89) Waly, T.; Kennedy, M. D.; Witkamp, G.-J.; Amy, G.; Schippers, J. C., On the induction time of CaCO3: effect of ionic strength. *Desalination and Water Treatment* 2012, 39, (1-3), 55-69.

(90) Söhnel, O.; Mullin, J. W., Interpretation of crystallization induction periods. *Journal of Colloid and Interface Science* 1988, 123, (1), 43-50.

(91) Ohara, M.; Reid, R. C., *Modeling crystal growth rates from solution*. ed.; Prentice-Hall: 1973.

(92) Söhnel, O. G. J., *Precipitation : basic principles and industrial applications*. ed.; Butterworth-Heinemann: Oxford [England]; Boston, 1992.

(93) Murphy, W. M.; Oelkers, E. H.; Lichtner, P. C., Surface reaction versus diffusion control of mineral dissolution and growth rates in geochemical processes. *Chemical Geology* 1989, 78, (3–4), 357-380.

(94) Karpinski, P. H.; Wey, J. S., 6 - Precipitation processes. *Handbook of Industrial Crystallization (Second Edition)* 2002, 141-160.

(95) Noyes, A. A.; Whitney, W. R., THE RATE OF SOLUTION OF SOLID SUBSTANCES IN THEIR OWN SOLUTIONS. *Journal of the American Chemical Society* 1897, 19, (12), 930-934.

(96) Miers, H. A., The concentration of the solution in contact with a growing crystal. *Philosophical Transactions* 1904, A202, 492-515.

(97) Nernst, W., Theorie der Reaktionsgeschwindigkeit in heterogenen Systemen. *Zeitschrift fuer physikalische Chemie* 1905, 47, (1), 52-55.

(98) Berthoud, A., Théorie de la formation des faces d'un crystal. *Journa de chimique physique* 1912, 10, 624-635.

(99) Valeton, J. J. P., Wachstum und Auflösung der Kristalle. *Zeitschrift für Kristallographie - Crystalline Materials* 1924, 60, (1), 38.

(100) Mullin, J. W., 6 - Crystal growth. *Crystallization (Fourth Edition)* 2001, 216-288.

(101) Helgeson, H. C.; Murphy, W. M.; Aagaard, P., Thermodynamic and kinetic constraints on reaction rates among minerals and aqueous solutions. II. Rate constants, effective surface area, and the hydrolysis of feldspar. *Geochimica Et Cosmochimica Acta* 1984, 48, (12), 2405-2432.

(102) Lasaga, A. C.; Kirkpatrick, R. J., *Kinetics of geochemical processes. 3 Vol. 8. Reviews in Mineralogy*. ed.; 1981; p Medium: X; Size: Pages: 408.

(103) Murphy, W. M.; Helgeson, H. C., Thermodynamic and kinetic constraints on reaction rates among minerals and aqueous solutions. III. Activated complexes and the pH-dependence of the rates of feldspar, pyroxene, wollastonite, and olivine hydrolysis. *Geochimica Et Cosmochimica Acta* 1987, 51, (12), 3137-3153.

(104) M., V.; W., S., Condensation on crystalline materials. *J. Phys. Chem.* 1931, 156, 23.

(105) Frank, F. C., The influence of dislocations on crystal growth. *Discussions of the Faraday Society* 1949, 5, (0), 48-54.

(106) Cubillas, P.; Anderson, M. W., Synthesis Mechanism: Crystal Growth and Nucleation. *Zeolites and Catalysis* 2010, 1-55.

(107) Burton, W. K.; Cabrera, N.; Frank, F. C., The Growth of Crystals and the Equilibrium Structure of their Surfaces. *Philosophical Transactions of the Royal Society of London. Series A, Mathematical and Physical Sciences* 1951, 243, (866), 299-358.

(108) Nielsen, A. E., Precipitates: formation, coprecipitation, and aging. *In Treatise on analytical chemistry* 1983, pp 269-347.

(109) Shiraki, R.; Brantley, S. L., KINETICS OF NEAR-EQUILIBRIUM CALCITE PRECIPITATION AT 100-DEGREES-C - AN EVALUATION OF ELEMENTARY REACTION-BASED AND AFFINITY-BASED RATE LAWS. *Geochimica Et Cosmochimica Acta* 1995, 59, (8), 1457-1471.

(110) Rimstidt, J. D.; Barnes, H. L., The kinetics of silica-water reactions. *Geochimica Et Cosmochimica Acta* 1980, 44, (11), 1683-1699.

(111) Saldi, G. D.; Jordan, G.; Schott, J.; Oelkers, E. H., Magnesite growth rates as a function of temperature and saturation state. *Geochimica Et Cosmochimica Acta* 2009, 73, (19), 5646-5657.

(112) Noiriel, C.; Steefel, C. I.; Yang, L.; Ajo-Franklin, J., Upscaling calcium carbonate precipitation rates from pore to continuum scale. *Chemical Geology* 2012, 318, 60-74.

(113) Pina, C. M.; Enders, M.; Putnis, A., The composition of solid solutions crystallising from aqueous solutions: the influence of supersaturation and growth mechanisms. *Chemical Geology* 2000, 168, (3-4), 195-210.

(114) Singh, G., *Chemistry Of Lanthanides And Actinides*. ed.; Discovery Publishing House Pvt. Limited: 2007.

(115) Curti, E., *Coprecipitation of radionuclides: basic concepts, literature review and first applications*. ed.; Paul Scherrer Institut Villigen: 1997.

(116) Curti, E.; Kulik, D. A.; Tits, J., Solid solutions of trace Eu(III) in calcite: Thermodynamic evaluation of experimental data over a wide range of pH and pCO2. *Geochimica Et Cosmochimica Acta* 2005, 69, (7), 1721-1737.

(117) McIntire, W. L., Trace element partition coefficients—a review of theory and applications to geology. *Geochimica Et Cosmochimica Acta* 1963, 27, (12), 1209-1264.

(118) Thien, B. M. J.; Kulik, D. A.; Curti, E., A unified approach to model uptake kinetics of trace elements in complex aqueous – solid solution systems. *Applied Geochemistry* 2014, 41, 135-150.

(119) Watson, E. B., A conceptual model for near-surface kinetic controls on the trace-element and stable isotope composition of abiogenic calcite crystals1. *Geochimica Et Cosmochimica Acta* 2004, 68, (7), 1473-1488.

(120) DePaolo, D. J., Surface kinetic model for isotopic and trace element fractionation during precipitation of calcite from aqueous solutions. *Geochimica Et Cosmochimica Acta* 2011, 75, (4), 1039-1056.

(121) Bünzli, J. C. G.; Choppin, G. R., *Lanthanide probes in life, chemical, and earth sciences: theory and practice*. ed.; Elsevier: 1989.

(122) Lakowicz, J. R., *Principles of fluorescence spectroscopy*. ed.; Springer Science & Business Media: 2013.

(123) Huittinen, N. M. Sorption of trivalent actinides onto gibbsite, gamma-alumina, and kaolinite : A spectroscopic study of An(III) interactions at the mineral-water interfaces. PhD Thesis. University of Helsinki, Faculty of Science, 2013.

(124) Wimmer, H. Laser-induzierte optische Spektroskopie zur Speziation von f-Elementen in natürlichen aquatischen Systemen. PhD Thesis. Technische Universität München, München, Germany, 1992.

(125) Carnall, W. T.; Rajnak, K., Electronic energy level and intensity correlations in the spectra of the trivalent actinide aquo ions. II. Cm3+ *The Journal of Chemical Physics* 1975, 63, (8), 3510-3514.

(126) Keenan, T. K., FIRST OBSERVATION OF AQUEOUS TETRAVALENT CURIUM1. *Journal of the American Chemical Society* 1961, 83, (17), 3719-3720.

(127) Kolbe, W.; Edelstein, N.; Finch, C.; Abraham, M., Zero-field splittings of Gd3+ and Cm3+ in CeO2 and ThO2. *The Journal of Chemical Physics* 1973, 58, (2), 2.

(128) Lindqvist-Reis, P.; Walther, C.; Klenze, R.; Eichhofer, A.; Fanghanel, T., Large ground-state and excited-state crystal field splitting of 8-fold-coordinate Cm3+ in Y(H2O)(8) Cl-3 center dot 15-crown-5. *Journal of Physical Chemistry B* 2006, 110, (11), 5279-5285.

(129) Muljadi, E. P., *Curium*. ed.; Paul Muljadi.

(130) Edelstein, N. M.; Klenze, R.; Fanghänel, T.; Hubert, S., Optical properties of Cm(III) in crystals and solutions and their application to Cm(III) speciation. *Coordination Chemistry Reviews* 2006, 250, (7–8), 948-973.

(131) Brundage, R.; Powell, R. L.; Beitz, J. V.; Liu, G., Measurement of homogeneous line widths and ground-state splittings of trivalent curium in fluoride glasses. *Journal of luminescence* 1996, 69, (3), 121-129.

(132) Carnall, W. T., A systematic analysis of the spectra of trivalent actinide chlorides in D3h site symmetry. *The Journal of Chemical Physics* 1992, 96, (12), 8713-8726.

(133) Carnall, W.; Wybourne, B., Electronic Energy Levels of the Lighter Actinides: U3+, Np3+, Pu3+, Am3+, and Cm3+. *The Journal of Chemical Physics* 1964, 40, (11), 3428-3433.

(134) Thouvenot, P.; Hubert, S.; Edelstein, N., Spectroscopic study and crystal-field analysis of Cm 3+ in the cubic-symmetry site of ThO 2. *Physical Review B* 1994, 50, (14), 9715.

(135) Lindqvist-Reis, P.; Klenze, R.; Schubert, G.; Fanghänel, T., Hydration of Cm3+ in Aqueous Solution from 20 to 200 °C. A Time-Resolved Laser Fluorescence Spectroscopy Study. *The Journal of Physical Chemistry B* 2005, 109, (7), 3077-3083.

(136) Hufner, S., *Optical Spectra of Transparent Rare Earth Compounds*. ed.; Elsevier Science: 2012.

(137) Schmidt, M. PhD Thesis: Untersuchungen zum Einbaumechanismus von Actiniden und Lanthaniden in Calcium-haltige Sekundärphasen. Naturwissenschaftlich-Mathematischen Gesamtfakultät. Ruprecht-Karls-Universität Heidelberg, 2009.

(138) Ruff, C. PhD Thesis: Spektroskopische und thermodynamische Untersuchung der Komplexierung von Cm(III) und Eu(III) mit hydrophilen Bis-Triazinylpyridinen. Fakultät für Chemie und Geowissenschaften. Ruprecht-Karls-Universität Heidelberg, 2014.

(139) Latva, M.; Kankare, J., THE 7F0→5D0 EXCITATION SPECTRA OF EUROPIUM(III) COMPLEXES OF AMINOCARBOXYLIC ACIDS. *Journal of Coordination Chemistry* 1998, 43, (2-3), 121-142.

(140) Gschneidner, K. A.; Bünzli, J. C. G.; Pecharsky, V. K., *Handbook on the Physics and Chemistry of Rare Earths: Optical Spectroscopy*. ed.; Elsevier Science: 2011.

(141) Buenzli, J. C. G.; Yersin, J. R., Fluorescence spectra and lifetime measurements of aqueous solutions of europium nitrate and perchlorate. *Inorganic Chemistry* 1979, 18, (3), 605-607.

(142) Bünzli, J.-C.; Choppin, G. R., Lanthanide probes in life, chemical and earth sciences. 1989.

(143) Carnall, W.; Goodman, G.; Rajnak, K.; Rana, R., A systematic analysis of the spectra of the lanthanides doped into single crystal LaF3. *The Journal of Chemical Physics* 1989, 90, (7), 3443-3457.

(144) Kalmykov, S. N.; Denecke, M. A., *Actinide Nanoparticle Research*. ed.; Springer Berlin Heidelberg: 2011.

(145)

(146) Stumpf, T.; Bauer, A.; Coppin, F.; Fanghänel, T.; Kim, J.-I., Inner-sphere, outer-sphere and ternary surface complexes: a TRLFS study of the sorption process of Eu (III) onto smectite and kaolinite. *Radiochimica Acta* 2002, 90, (6), 345-349.

(147) Hartmann, E.; Baeyens, B.; Bradbury, M. H.; Geckeis, H.; Stumpf, T., A spectroscopic characterization and quantification of M (III)/clay mineral outer-sphere complexes. *Environmental Science & Technology* 2008, 42, (20), 7601-7606.

(148) Kimura, T.; Choppin, G. R., Luminescence study on determination of the hydration number of Cm (III). *Journal of Alloys and Compounds* 1994, 213, 313-317.

(149) Horrocks Jr, W. D.; Sudnick, D. R., Lanthanide ion probes of structure in biology. Laser-induced luminescence decay constants provide a direct measure of the number of metal-coordinated water molecules. *Journal of the American Chemical Society* 1979, 101, (2), 334-340.

(150) Garrels, R. M.; Christ, C. L., *Solutions, minerals, and equilibria*. ed.; Harper & Row: 1965.

(151) Somasundaran, P., Zeta potential of apatite in aqueous solutions and its change during equilibration. *Journal of Colloid and Interface Science* 1968, 27, (4), 659-666.

(152) Martińez, A. L.; Uribe, A. S., Interfacial properties of celestite and strontianite in aqueous solutions. *Minerals Engineering* 1995, 8, (9), 1009-1022.

(153) López-Valdivieso, A.; Robledo-Cabrera, A.; Uribe-Salas, A., Flotation of celestite with the anionic collector sodium dodecyl sulfate. Effect of carbonate ions. *International Journal of Mineral Processing* 2000, 60, (2), 79-90.

(154) Blanc P., L. A., Piantone P. , 2007.

(155) Hummel, W.; Berner, U.; Curti, E.; Pearson, F. J.; Thoenen, T., *Nagra/PSI chemical thermodynamic data base 01/01 - Universal Publishers/uPublish.com* 2002.

(156) Campbell, J. R.; Nancollas, G. H., The crystallization and dissolution of strontium sulphate in aqueous solution. *Journal of Physical Chemistry* 1969, 73, 1735-1740.

(157) Sühnel, O.; Handlířová, M., Precipitation of Strontium Sulphate. *Crystal Research and Technology* 1984, 19, (4), 477-490.

(158) Yeboah, Y. D.; Saeed, M. R.; Lee, A. K. K., Kinetics of strontium sulfate precipitation from aqueous-electrolyte solutions. *Journal of Crystal Growth* 1994, 135, (1-2), 323-330.

(159) Malollari, I. X.; Klepetsanis, P. G.; Koutsoukos, P. G., PRECIPITATION OF STRONTIUM SULFATE IN AQUEOUS-SOLUTIONS AT 25-DEGREES-C. *Journal of Crystal Growth* 1995, 155, (3-4), 240-246.

(160) Hamdona, S. K.; Hamza, S. M.; Mangood, A. H., The influence of polyphosphonates on the precipitation of strontium sulfate (celestite) from aqueous solutions. *Desalination and Water Treatment* 2010, 24, (1-3), 55-60.

(161) He, S. L.; Oddo, J. E.; Tomson, M. B., THE NUCLEATION KINETICS OF STRONTIUM SULFATE IN NACL SOLUTIONS UP TO 6 M AND 90-DEGREES-C WITH OR WITHOUT INHIBITORS. *Journal of Colloid and Interface Science* 1995, 174, (2), 327-335.

(162) Pina, C. M.; Tamayo, Á., Crystallisation of strontium sulphates from Si-bearing aqueous solutions. *Geochimica Et Cosmochimica Acta* 2012, 92, (0), 220-232.

(163) Helz, G. R.; Holland, H. D., The solubility and geologic occurrence of strontianite. *Geochimica Et Cosmochimica Acta* 1965, 29, (12), 1303-1315.

(164) Busenberg, E.; Plummer, L. N.; Parker, V. B., The solubility of strontianite (SrCO3) in CO2-H2O solutions between 2 and 91°C, the association constants of SrHCO+3(aq) and SrCO03(aq) between 5 and 80°C, and an evaluation of the thermodynamic properties of Sr2+(aq) and SrCO3(cr) at 25°C and 1 atm total pressure. *Geochimica Et Cosmochimica Acta* 1984, 48, (10), 2021-2035.

(165) Zeppenfeld, K., Crystallization kinetics of strontianite from Sr(HCO3)2 solutions. *Chemie der Erde - Geochemistry* 2006, 66, (4), 319-323.

(166) Parkhurst, D. L. A., C. A. J., User's guide to PHREEQC (Version 2) : a computer program for speciation, batch-reaction, one-dimensional transport, and inverse geochemical calculations. *Water-Resources Investigations Report* 1999, (4259), 312.

(167) Ball, J. W.; Nordstrom, D. K.; Zachmann, D. W., *WATEQ4F - a personal computer Fortran translation of the geochemical model WATEQ2 with revised data base Open-File Report* 1987.

(168) Puigdomenech, I., HYDRA MEDUSA: Make Equilibrium Diagrams Using Sophisticated Algorithms (http://www.kemi.kth.se/medusa/), KTH (Royal Institute of Technology), Stockholm. *HYDRA MEDUSA: Make Equilibrium Diagrams Using Sophisticated Algorithms* 2001.

(169) Giffaut, E.; Grivé, M.; Blanc, P.; Vieillard, P.; Colàs, E.; Gailhanou, H.; Gaboreau, S.; Marty, N.; Madé, B.; Duro, L., Andra thermodynamic database for performance assessment: ThermoChimie. *Applied Geochemistry* 2014, 49, (0), 225-236.

(170) Dekker, M., *Laser-induced plasmas and applications*. ed.; New York, 1989.

(171) Bitea, C. PhD Thesis: Laser-induzierte breakdown detection (LIBD): Qquantifizierung der Kolloidbildung vierwertiger Actiniden und Homologen. Fakültät für Maschinenbau. Universität Karlsruhe, 2004.

(172) Walther, C.; Büchner, S.; Filella, M.; Chanudet, V., Probing particle size distributions in natural surface waters from 15 nm to 2 μm by a combination of LIBD and single-particle counting. *Journal of Colloid and Interface Science* 2006, 301, (2), 532-537.

(173) Delos, A.; Walther, C.; Schäfer, T.; Büchner, S., Size dispersion and colloid mediated radionuclide transport in a synthetic porous media. *Journal of Colloid and Interface Science* 2008, 324, (1–2), 212-215.

(174) Walther, C.; Bitea, C.; Hauser, W.; Kim, J. I.; Scherbaum, F. J., Laser induced breakdown detection for the assessment of colloid mediated radionuclide migration. *Nuclear Instruments & Methods in Physics Research Section B-Beam Interactions with Materials and Atoms* 2002, 195, (3-4), 374-388.

(175) Bundschuh, T.; Knopp, R.; Kim, J. I., Laser-induced breakdown detection (LIBD) of aquatic colloids with different laser systems. *Colloids and Surfaces A: Physicochemical and Engineering Aspects* 2001, 177, (1), 47-55.

(176) Bundschuh, T.; Hauser, W.; Kim, J. I.; Knopp, R.; Scherbaum, F. J., Determination of colloid size by 2-D optical detection of laser induced plasma. *Colloids and Surfaces a-Physicochemical and Engineering Aspects* 2001, 180, (3), 285-293.

(177) Latkoczy, C.; Kagi, R.; Fierz, M.; Ritzmann, M.; Gunther, D.; Boller, M., Development of a mobile fast-screening laser-induced breakdown detection (LIBD) system for field-based measurements of nanometre sized particles in aqueous solutions. *Journal of Environmental Monitoring* 2010, 12, (7), 1422-1429.

(178) Jung, E. C.; Cho, H. R.; Park, K. K.; Yeon, J. W.; Song, K., Nanoparticle sizing by a laser-induced breakdown detection using an optical probe beam deflection. *Applied Physics B-Lasers and Optics* 2009, 97, (4), 867-875.

(179) Rimstidt, J. D.; Dove, P. M., Mineral/solution reaction rates in a mixed flow reactor: Wollastonite hydrolysis. *Geochimica Et Cosmochimica Acta* 1986, 50, (11), 2509-2516.

(180) Hill, C. G., *An introduction to Chemical Engineering Kinetics and Reactor Design*. ed.; Wiley: New York, 1977; p 608.

(181) Fagerlund, G., Determination of specific surface by the BET method. *Matériaux et Construction* 1973, 6, (3), 239-245.

(182) Ghader, S.; Manteghian, M.; Kokabi, M.; Mamoory, R. S., Induction Time of Reaction Crystallization of Silver Nanoparticles. *Chemical Engineering & Technology* 2007, 30, (8), 1129-1133.

(183) Vavouraki, A. I.; Koutsoukos, P. G., Kinetics of crystal growth of mirabilite in aqueous supersaturated solutions. *Journal of Crystal Growth* 2012, 338, (1), 189-194.

(184) Dhar, N. R., Influence of Ageing on Inorganic Hydrophile Colloids, Cells and Colloids in the Animal Body. *The Journal of Physical Chemistry* 1929, 34, (3), 549-553.

(185) Benítez, E.; Lozano, J.; Genovese, D., Fractal dimension and mechanism of aggregation of apple juice particles. *Food Science and Technology International* 2010, 16, (2), 179-186.

(186) Kashchiev, D., Note: On the critical supersaturation for nucleation. *The Journal of Chemical Physics* 2011, 134, (19), 196102.

(187) Pound, G. M., Selected Values of Critical Supersaturation for Nucleation of Liquids from the Vapor. *Journal of Physical and Chemical Reference Data* 1972, 1, (1), 119-133.

(188) Lacmann, R., Crystallization, Third Edition. J. W. MULLIN, Butterworth-Heinemann, Oxford 1997, 527 Seiten, zahlr. Abb. und ISBN 0-7506-3759-5. *Chemie Ingenieur Technik* 1998, 70, (11), 1468-1468.

(189) Nielsen, A. E., NIELSEN AE - KINETICS OF PRECIPITATION. *American Scientist* 1966, 54, (3), A352-&.

(190) Reardon, E. J.; Armstrong, D. K., Celestite (SrSO4(s)) solubility in water, seawater and NaCl solution. *Geochimica Et Cosmochimica Acta* 1987, 51, (1), 63-72.

(191) C. Michael Hogan; A. Jorgensen; C. Cleveland, Calcium. eds. *Cleveland. Encyclopedia of Earth* 2010.

(192) Dove, P. M.; Czank, C. A., Crystal chemical controls on the dissolution kinetics of the isostructural sulfates: Celestite, anglesite, and barite. *Geochimica Et Cosmochimica Acta* 1995, 59, (10), 1907-1915.

(193) Risthaus, P.; Bosbach, D.; Becker, U.; Putnis, A., Barite scale formation and dissolution at high ionic strength studied with atomic force microscopy. *Colloids and Surfaces A: Physicochemical and Engineering Aspects* 2001, 191, (3), 201-214.

(194) Bosbach, D.; Hochella Jr, M. F., Gypsum growth in the presence of growth inhibitors: a scanning force microscopy study. *Chemical Geology* 1996, 132, (1–4), 227-236.

(195) tiller, W. A., *The Science of Crystallization. Microscopic Interfacial Phenomena*. ed.; Cambridge University Press: 1991.

(196) Pearson, F. J.; Tournassat, C.; Gaucher, E. C., Biogeochemical processes in a clay formation in situ experiment: Part E - Equilibrium controls on chemistry of pore water from the Opalinus Clay, Mont Terri Underground Research Laboratory, Switzerland. *Applied Geochemistry* 2011, 26, (6), 990-1008.

(197) Komine, H.; Ogata, N., Experimental study on swelling characteristics of compacted bentonite. *Canadian Geotechnical Journal* 1994, 31, (4), 478-490.

(198) Nielsen, A. E., Electrolyte crystal growth mechanisms. *Journal of Crystal Growth* 1984, 67, (2), 289-310.

(199) Helgeson, H. C.; Kirkham, D. H., Theoretical prediction of thermodynamic properties of aqueous electrolytes at high pressures and temperatures. III. Equation of state for aqueous species at infinite dilution. *Journal Name: Am. J. Sci.; (United States); Journal Volume: 276:2* 1976, Medium: X; Size: Pages: 97-240.

(200) Marty, N. C.; Claret, F.; Lassin, A.; Tremosa, J.; Blanc, P.; Madé, B.; Giffaut, E.; Cochepin, B.; Tournassat, C., A database of dissolution and precipitation rates for clay-rocks minerals. *Applied Geochemistry* 2015, 55, 108-118.

(201) Marty, N. C. M.; Tournassat, C.; Burnol, A.; Giffaut, E.; Gaucher, E. C., Influence of reaction kinetics and mesh refinement on the numerical modelling of concrete/clay interactions. *Journal of Hydrology* 2009, 364, (1–2), 58-72.

(202) William Miller, R. A. N. C. I. M.; John, S., Waste Management Series. *Waste Management Series* 2000, Volume 2, 311-316.

(203) Brantley, S. L.; Conrad, C. F., Analysis of Rates of Geochemical Reactions. *Kinetics of Water-Rock Interaction* 2008, 1-37.

(204) Lee, A. K. K.; Saeed, M. R.; Shalabi, M. A.; Rahman, F., Kinetics of Crystal Growth of Sparingly Soluble Sulfates. *Proc. NACE 4th Middle East Corrosion Conference* 1988, Part 1, 259.

(205) Zuddas, P.; Mucci, A., Kinetics of Calcite Precipitation from Seawater: II. The Influence of the Ionic Strength. *Geochimica Et Cosmochimica Acta* 1998, 62, (5), 757-766.

(206) Fanghanel, T.; Kim, J. I., Spectroscopic evaluation of thermodynamics of trivalent actinides in brines. *Journal of Alloys and Compounds* 1998, 271, 728-737.

(207) Giffaut, E.; Grivé, M.; Blanc, P.; Vieillard, P.; Colàs, E.; Gailhanou, H.; Gaboreau, S.; Marty, N.; Madé, B.; Duro, L., Andra thermodynamic database for performance assessment: ThermoChimie. *Applied Geochemistry* 2014, 49, 225-236.

(208) Fanghänel, T.; Kim, J. I.; Klenze, R.; Kato, Y., Formation of Cm(III) chloride complexes in CaCl2 solutions. *Journal of Alloys and Compounds* 1995, 225, (1–2), 308-311.

(209) Vercouter, T.; Amekraz, B.; Moulin, C.; Giffaut, E.; Vitorge, P., Sulfate Complexation of Trivalent Lanthanides Probed by Nanoelectrospray Mass Spectrometry and Time-Resolved Laser-Induced Luminescence. *Inorganic Chemistry* 2005, 44, (21), 7570-7581.

(210) Geipel, G., Some aspects of actinide speciation by laser-induced spectroscopy. *Coordination Chemistry Reviews* 2006, 250, (7–8), 844-854.

(211) Plancque, G.; Moulin, V.; Toulhoat, P.; Moulin, C., Europium speciation by time-resolved laser-induced fluorescence. *Analytica Chimica Acta* 2003, 478, (1), 11-22.

(212) Schmidt, M.; Stumpf, T.; Walther, C.; Geckeis, H.; Fanghanel, T., Incorporation versus adsorption: substitution of Ca2+ by Eu3+ and Cm3+ in aragonite and gypsum. *Dalton Transactions* 2009, 0, (33), 6645-6650.

(213) Shalibeik, H., *Rare-Earth-Doped Fiber Lasers and Amplifiers*. ed.; Cuvillier: 2007.

(214) Xu, T.; Sonnenthal, E.; Spycher, N.; Pruess, K., TOUGHREACT—a simulation program for non-isothermal multiphase reactive geochemical transport in variably saturated geologic media: applications to geothermal injectivity and CO 2 geological sequestration. *Computers & Geosciences* 2006, 32, (2), 145-165.

7 List of abbreviations

Symbol	units	description
Ω	[-]	saturation index
σ	[-]	relative supersaturation
β	[-]	geometrical shape factor
γ	[$J \cdot m^{-2}$]	interfacial tension (free energy per unit area of the nucleus interface)
θ	degree	contact angle
δ	m	length of the diffusion path
τ	s	fluorescence lifetime
a	$mol \cdot L^{-1}$	activity product
A		pre-exponential factor
$A_{crystal}$	m^2	surface area of a crystal
BDP		breakdown probability
c	$mol \cdot L^{-1}$	concentration
c^*	$mol \cdot L^{-1}$	equilibrium concentration
c_i	$mol \cdot L^{-1}$	solute concentration at the liquid-solid interface
d	m	particle diameter
D	$m^2 \cdot s^{-1}$	diffusion coefficient
ESN		early stage nuclei
E_a	$J \cdot mol^{-1}$	Activation energy
ϵ_C	[-]	temperature dependent constant
f(Θ)	[-]	geometrical factor related to the nucleation barrier
g	[-]	apparent order of the overall crystal growth process
ΔG	[$kJ \cdot mol^{-1}$]	free energy change
ΔG_S	[$kJ \cdot mol^{-1}$]	surface excess free energy
ΔG_V	[$kJ \cdot mol^{-1}$]	volume excess free energy
ΔG^*_{Hom}	[$kJ \cdot mol^{-1}$]	energy barrier for homogeneous nucleation
ΔG^*_{Het}	[$kJ \cdot mol^{-1}$]	energy barrier for heterogeneous nucleation
I	[$mol \cdot kg^{-1}$]	ionic strength
IAP	[-]	ionic activity product
J_S	[min^{-1}]	nucleation rate
K		equilibrium constant

List of abbreviations

k_{obs}	ms^{-1}	fluorescence decay rate
k_r	$[mol \cdot m^{-2} \cdot s^{-1}]$	rate constant of surface reaction controlled crystal growth
K_{SP}	[-]	solubility product
k_B	$J \cdot K^{-1}$	Boltzmann constant
m	g	mass of solid
Q	$L \cdot s^{-1}$	flow rate
r	[nm]	radius of a nucleus/particle
r_c	[nm]	critical radius
R	$J \cdot mol^{-1} \cdot K^{-1}$	gas constant
R_G	$mol \cdot m^{-2} \cdot s^{-1}$	rate of crystal growth
S	[-]	supersaturation ratio
SPC		single particle counting
t_{Ind}	s	induction time
t_g	s	time of nuclei growth to a detectable size
t_n	s	nucleation time
t_r	s	relaxation time
V_{eff}	$[m^3]$	effective focal volume
ϑ_m	m^3	volume of the growth unit

8 List of tables

9 List of figures

List of figures

10 Annexes

Annex 1: determination of $SrSO_4$ specific surface area - sample 1

Quantachrome Corporation

Quantachrome Autosorb Automated Gas Sorption System Report
Autosorb for Windows® Version 1.19

Sample ID **$SrSO_4$** – (a)
Description Temgoua
Comments
Sample Weight 0.1941 g
Adsorbate KRYPTON
Outgas Temp 573 K
Operator: Kisely
Cross-Sec Area 20.5 Å²/molec
Outgas Time 3.0 hrs
Analysis Time 144.0 min
NonIdeality 3.000E-05
P/Po Toler 0
End of Run 07/22/2014 19:48
Molecular Wt 83.8000 $g \cdot mol^{-1}$
Equil Time 3
File Name AS472201.RAW
Station # 1
Bath Temp. 77.35

MULTIPOINT BET

P/Po	Volume [cc/g] STP	1/(W((Po/P)-1))
1.0097e-01	0.1087	2.764E+02
1.5118e-01	0.1208	3.943E+02
2.0095e-01	0.1296	5.191E+02
2.5128e-01	0.1370	6.553E+02
2.8884e-01	0.1429	7.603E+02

Area = 5.692E-01 $m^2 \cdot g^{-1}$
Slope = 2.579E+03
Y- Intercept = 8.738E+00
Correlation Coefficient = 0.999405
C = 2.962E+02

Annex 2 : determination of $SrSO_4$ specific surface area - sample 2

Quantachrome Corporation

Quantachrome Autosorb Automated Gas Sorption System Report
Autosorb for Windows® Version 1.19

Sample ID **$SrSO_4$ –(b)**
Description Temgoua
Comments
Sample Weight 0.5119 g
Adsorbate KRYPTON
Outgas Temp 573 K
Operator Kisely
Cross-Sec Area 20.5 Å²/molec
Outgas Time 3.0 hrs
Analysis Time 188.8 min
NonIdeality 3.000E-05
P/Po Toler 0
End of Run 01/22/2015 16:37
Molecular Wt 83.8000 $g \cdot mol^{-1}$
Equil Time 3
File Name AS512201.RAW
Station # 1
Bath Temp. 77.35

MULTIPOINT BET

P/Po	Volume [cc/g] STP	1/(W((Po/P)-1))
9.9846e-02	0.1016	2.920E+02
1.4987e-01	0.1148	4.108E+02
2.0027e-01	0.1241	5.397E+02
2.4991e-01	0.1321	6.747E+02
2.9974e-01	0.1390	8.234E+02

Area = 5.514E-01 $m^2 \cdot g^{-1}$
Slope = 2.654E+03
Y - Intercept = 1.753E+01
Correlation Coefficient = 0.999030
C = 1.524E+02

Annex 3: Determination of the specific surface area for the seed crystals of $SrCO_3$

Quantachrome Corporation

Quantachrome Autosorb Automated Gas Sorption System Report
Autosorb for Windows® Version 1.19

Sample ID **$SrCO_3$**
Description Temgoua
Comments
Sample Weight 0.5907 g
Adsorbate KRYPTON
Outgas Temp 373 K
Operator Kisely
Cross-Sec Area 20.5 Å²/molec
Outgas Time 72.0 hrs
Analysis Time 189.9 min
NonIdeality 3.000E-05
P/Po Toler 0
End of Run 06/08/2015 15:49
Molecular Wt 83.8000 $g \cdot mol^{-1}$
Equil Time 3
File Name AS560801.RAW
Station # 1
Bath Temp. 77.35

MULTIPOINT BET

P/Po	Volume [cc/g] STP	1/(W((Po/P)-1))
9.9738e-02	0.1113	2.663E+02
1.5006e-01	0.1249	3.780E+02
2.0035e-01	0.1368	4.898E+02
2.5049e-01	0.1479	6.043E+02
2.9948e-01	0.1588	7.200E+02

Area = 6.390E-01 $m^2 \cdot g^{-1}$
Slope = 2.267E+03
Y - Intercept = 3.813E+01
Correlation Coefficient = 0.999915
C = 6.046E+01

Annex 4. Determination of the SSA of strontianite at the end of MFR experiment at S = 3162

Quantachrome Corporation

Quantachrome Autosorb Automated Gas Sorption System Report
Autosorb for Windows® Version 1.19

Sample ID **MFR50 ($SrCO_3$)**
Description Temgoua
Comments
Sample Weight 0.6669 g
Adsorbate NITROGEN
Outgas Temp 300 K
Operator Kisely
Cross-Sec Area 16.2 $Å^2$/molec
Outgas Time 5.0 hrs
Analysis Time 61.3 min
NonIdeality 6.580E-05
P/Po Toler 1
End of Run 05/28/2013 14:54
Molecular Wt 28.0134 $g \cdot mol^{-1}$
Equil Time 3
File Name AS352802.RAW
Station # 1
Bath Temp. 77.35

MULTIPOINT BET

P/Po	Volume [cc/g] STP	1/(W((Po/P)-1))
1.1354e-01	0.1066	9.616E+02
1.5532e-01	0.1278	1.151E+03
2.0532e-01	0.1494	1.384E+03
2.5523e-01	0.1714	1.600E+03
2.9542e-01	0.1875	1.789E+03

Area = 6.986E-01 $m^2 \cdot g^{-1}$
Slope = 4.538E+03
Y - Intercept = 4.469 E+02
Correlation Coefficient = 0.999939
C = 1.1166E+01

Annex 5. TEM and elemental analysis (STEM-EDX) of the ESN of celestite (S = 12.6) after 75sec (upper picture) and 10 min (lower picture) of reaction time. The induction time corresponding to the supersaturation in this experiment is 25 min. The red squares on the pictures below define the area of the sample chosen for the STEM-EDX measurements. According to the elements specific peak, the sample after 75 sec contains celestite, while the square like bright spot on the picture after 10 min is a NaCl crystal.

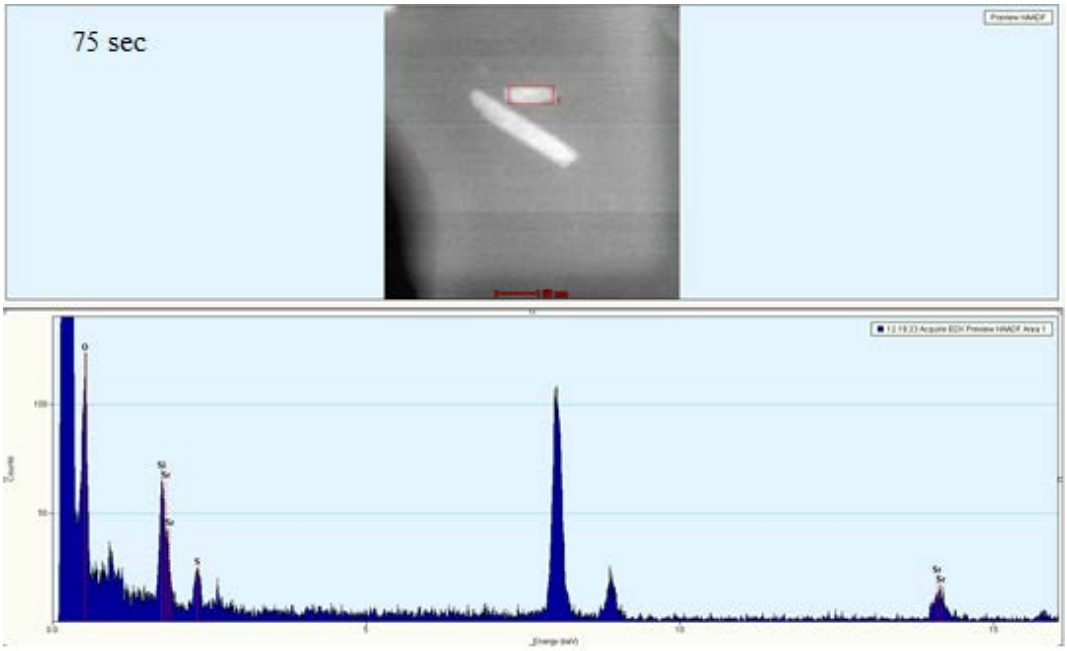

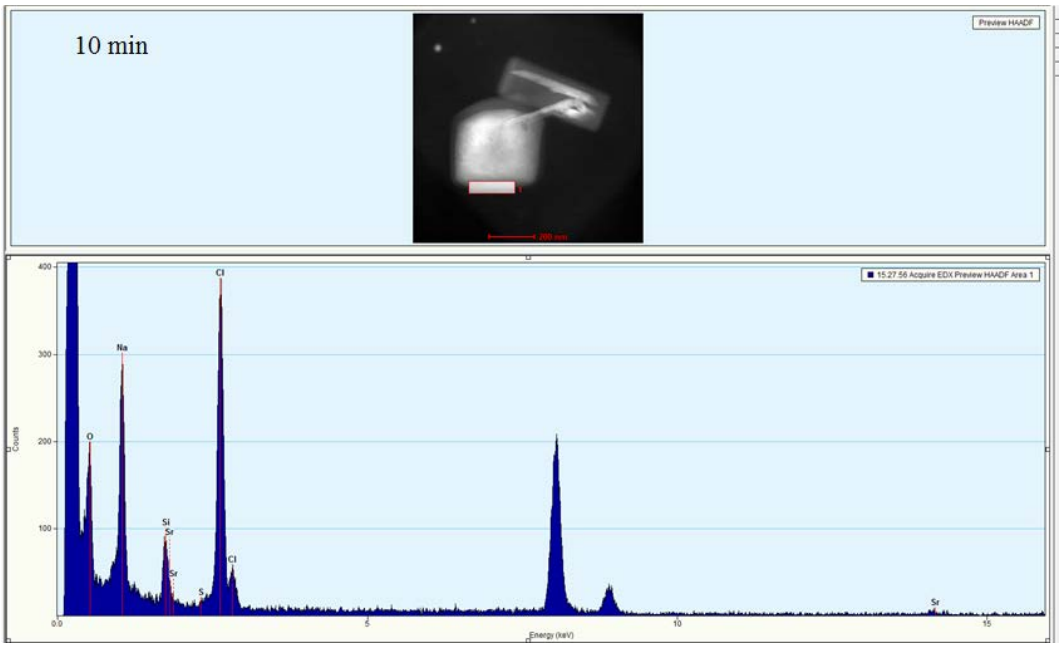

Annex 6 Induction times for the nucleation of celestite as a function of the solution supersaturation at 297 K and ionic strength of 0.1 mol·kg^{-1} NaCl; [Sr^{2+}] = [SO_4^{2-}].

[Sr^{2+}] 10^{-3} M	t_{Ind} (min)	Ln(t_{Ind})	Initial S (SrSO4)
2.37	> 2400	> 7.8	1.99
2.68	1305± 1	7.17	2.51
3.04	1140 ± 1	7.04	3.16
3.45	335 ± 1	5.86	3.98
4.47	209 ± 1	5.37	6.31
5.10	78 ± 1	4.35	7.94
5.83	46 ± 1	3.82	10.00
6.50	28 ± 1	3.35	12.02
6.67	25 ± 1	3.27	12.59
7.65	15 ± 1	2.70	15.85
8.80	12 ± 1	2.44	19.95
10.15	9 ± 1	2.18	25.12
11.73	5 ± 1	1.60	31.63

Annex 7. The induction time for the nucleation of strontianite as a function of solution supersaturation at 297 K and ionic strength of 0.1 mol·kg^{-1} NaCl; $pCO_2 = 5.5 \cdot 10^{-7}$. Speciation calculated with PhreeqC using the wateq4f database.

$[CO_3^{2-}]$ 10^{-4} M	$[Sr^{2+}]$ 10^{-4} M	[DIC][13] 10^{-4} M	t_{Ind} (min)	Ln(t_{Ind})	Initial S ($SrCO_3$)	pH (PhreeqC)
0.90	2.57	2.57	> 2400	> 7.8	6.3	9.98
1.02	2.79	2.84	540 ± 1	6.29	7.94	10.01
1.16	3.10	3.16	400 ± 1	5.99	10.00	10.04
1.24	3.27	3.33	251 ± 1	5.53	11.22	10.05
1.32	3.44	3.50	226 ± 1	5.42	12.59	10.06
1.42	3.65	3.71	177 ± 1	5.18	14.45	10.08
1.50	3.83	3.89	128 ± 1	4.85	15.85	10.09
1.61	4.05	4.12	73 ± 1	4.29	18.20	10.11
1.71	4.26	4.33	66 ± 1	4.18	19.95	10.12
1.92	4.74	4.81	36 ± 1	3.59	25.12	10.15
2.09	5.05	5.13	30 ± 1	3.40	28.84	10.16
2.20	5.28	5.36	25 ± 1	3.23	31.62	10.17

Annex 8. Effect of temperature on the induction time for the nucleation of celestite at a constant solute concentration. The given solute concentrations and thus the supersaturation ratio are referred to the initial conditions. Strontium and sulfate ions are available in equal concentrations.

T [K]	$[Sr^{2+}] \cdot 10^{-3}$ M	t_{Ind} [min]	Log (S)	Log k [190]
286 ± 0.5	5.83	93 ± 2	1.03	- 6.63
295 ± 0.5	5.83	48 ± 2	1.01	- 6.62
304 ± 0.5	5.83	29 ± 2	1.02	- 6.65
314 ± 0.5	5.83	14 ± 2	1.04	- 6.69
322 ± 0.5	5.83	10 ± 2	1.05	- 6.72

[13] DIC dissolved inorganic carbon

Annex 9. Effect of temperature on the induction time for the nucleation of strontianite at a constant initial Sr^{2+} concentration. The initial carbonate concentration is equal to the initial strontium concentration and the partial pressure of CO_2 is varied to match the measured pH-values. Given DIC and CO_3^{2-} correspond to the values after equilibration with CO_2.

T [K]	$[Sr^{2+}]$ 10^{-4} M	[DIC] 10^{-4} M	$[CO_3^{2-}]$ 10^{-4} M	t_{Ind} [min]	log (S)	log k [164]	pH (measured)	Log $p(CO_2)$
279	3.83	5.10	1.75	560 ± 3	1.31	-9.31	10.04	-5.99
284	3.83	4.96	1.66	238 ± 2	1.27	-9.29	9.98	-5.93
288	3.83	4.94	1.54	158 ± 2	1.22	-9.28	9.89	-5.82
295	3.83	4.69	1.38	110 ± 1	1.16	-9.27	9.82	-5.75
303	3.83	4.24	1.17	58 ± 1	1.10	-9.28	9.77	-5.75
308	3.83	4.07	1.02	38 ± 1	1.07	-9.29	9.70	-5.67
317	3.83	3.71	0.76	26 ± 1	0.94	-9.33	9.58	-5.55

Annex 10. Effect of dissolved silica on the induction time for the nucleation of celestite and strontianite at constant temperature (295 K) and solute concentrations. The initial concentration of Sr^{2+} and SO_4^{2-} or CO_3^{2-} are equal.

celestite			strontianite		
$[Sr^{2+}] \cdot 10^{-3}$M	[Si] ppm	t_{Ind} [min]	$[Sr^{2+}] \cdot 10^{-4}$M	[Si] ppm	t_{Ind} [min]
6.67	0	25 ± 1	5.28	0	19 ± 1
6.67	0.18	34 ± 1	5.28	0.26	38 ± 1
6.67	0.39	72 ± 1	5.28	0.51	43 ± 1
6.67	0.54	99 ± 1	5.28	0.77	57 ± 1
6.67	0.90	325 ± 1	5.28	1.79	47 ± 1
6.67	2.18	645 ± 1	5.28	3.83	60 ± 1
6.67	2.90	780 ± 1	5.28	5.11	53 ± 1
6.67	5.11	990 ± 1	5.28	6.39	50 ± 1
6.67	7.67	1500 ± 1	5.28	7.67	50 ± 1

Annex 11. Selected data highlighting the impact of the ionic strength on the supersaturation. To keep a constant supersaturation, the solute concentration must be increased as the ionic strength of the system increases.

	Initial solute concentrations $[Sr^{2+}] = [SO_4^{2-}]$ in mM			
Log $S_{celestite}$	I= 10^{-3} mol·kg^{-1}	I= 0.1 mol·kg^{-1}	I= 0.5 mol·kg^{-1}	I= 1 mol·kg^{-1}
0.8	2.24	4.47	8.58	11.69
0.9	2.65	5.10	9.76	13.19
1	3.08	5.82	10.98	14.88
1.1	3.63	6.50	12.43	16.80

Annex 12. Induction time for the nucleation of celestite at constant supersaturations as a function of the ionic strength

	Induction time (min)			
Log $S_{celestite}$	I= 10^{-3} mol·kg^{-1}	I= 0.1 mol·kg^{-1}	I= 0.5 mol·kg^{-1}	I= 1 mol·kg^{-1}
0.4	-	-	-	230
0.5	-	-	-	157
0.6	-	-	-	120
0.7	-	-	-	80
0.8	-	209	92	44
0.9	250	78	63	17.5
1	100	46	25	5
1.1	40	25	6	< 1
1.2	16	15	< 1	< 1
1.3	12	12	< 1	< 1
1.4	10	9	< 1	< 1
1.5	4	5	< 1	< 1

Annex 13. Induction time for the nucleation of strontianite at constant solute concentrations as a function of ionic strength

$[Sr^{2+}] = [CO_3^{2-}]$ mM	I [mol·kg^{-1}]	Log $S_{Strontianite}$	t_{Ind} [min]
0.474	$5 \cdot 10^{-4}$	2.09	9.2 ± 0.5
0.474	100	1.40	36 ± 0.5
0.474	150	1.27	81 ± 0.5
0.474	200	1.17	160 ± 1
0.474	300	1.02	500 ± 1
0.474	400	0.91	500 ± 10

Annex 14. Elemental analysis of the crystallites present on the surface of the glass beads after the nucleation of celestite

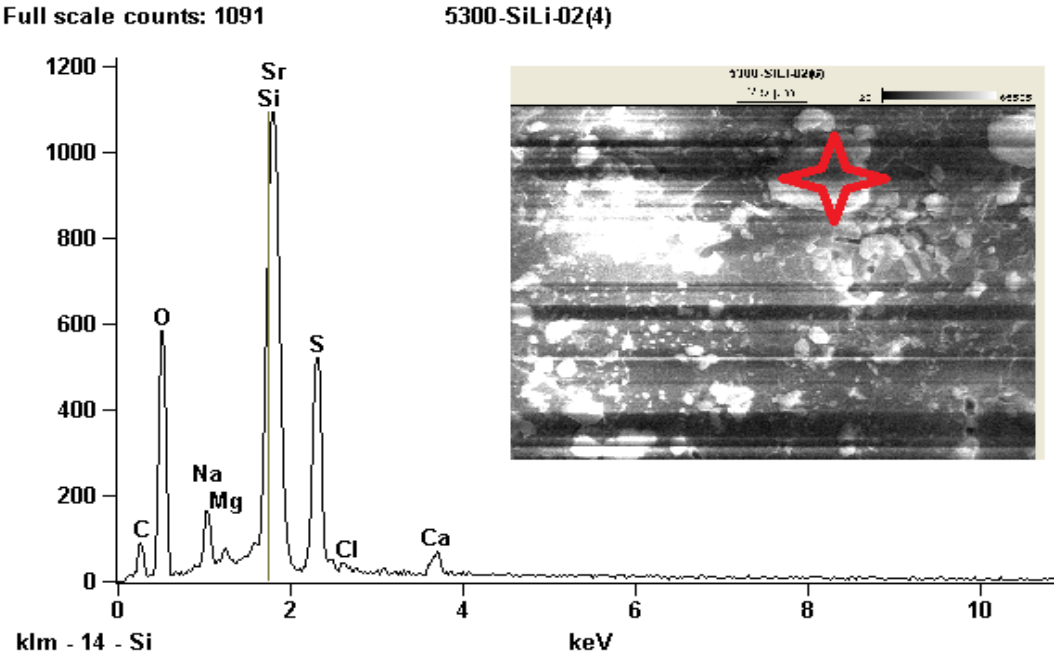

Filter Fit	Chi Squared: 1.299	Acc. voltage	20.0 kV
Errors	± 1 Sigma	Take off angle	34.9 deg
Correction method	Proza (Phi-Rho-Z)	Detector	UDD

Quantitative Results for: 5300-SiLi-02(4)

Element Line	Weight %	Atom %	Atom % Error
C K	16.83	29.56	+/- 2.22
O K	37.32	49.22	+/- 0.90
Na K	2.92	2.68	+/- 0.18
Mg K	0.38	0.33	+/- 0.05
Si K	5.87	4.41	+/- 0.16
S K	10.70	7.04	+/- 0.15
Cl K	0.38	0.23	+/- 0.04
Ca K	1.29	0.68	+/- 0.04
Sr L	24.30	5.85	+/- 0.07
Total	100.00	100.00	

Annex 15. Growth rates of strontianite and celestite as a function of the initial supersaturation

$S_{initial}$ strontianite	$10^{-9} \cdot R_G$ [mol·m^{-2}·s^{-1}]	$S_{initial}$ celestite	$10^{-8} \cdot R_G$ [mol·m^{-2}·s^{-1}]
5.0	3.7 ± 0.8	2.5	3.8 ± 3.1
6.3	4.5 ± 0.6	3.6	5.3 ± 0.7
7.9	6.0 ± 0.1	4.0	8.6 ± 0.8
8.9	8.7 ± 0.4	4.9	14.3 ± 0.4
10	9.8 ± 0.5	5.0	17.2 ± 1.5
12.6	11.8 ± 0.9	6.3	22.8 ± 0.2
15.9	13.1 ± 0.4	7.8	25.3 ± 3.1
17.8	17.2 ± 1.0	8.9	29.7 ± 4
25.1	20.8 ± 0.8	10.0	33.4 ± 0.4
31.6	29.8 ± 0.2	12.3	57.2 ± 3.2
35.5	29.9 ± 0.3	15.9	75.4 ± 1.4
39.8	35.6 ± 0.3	16.2	77.2 ± 0.7
50.1	47.7 ± 0.2	24.0	111.0 ± 3.1
204	11.6 ± 0.2[14]	31.6	134.0 ± 2.2
1000	28.0 ± 0.3[14]	100.0	353.0 ± 13.5[14]
2042	50.4 ± 0.2[14]	309.0	730.0 ± 19.1[14]
17378	142.0 ± 0.2[14]		

Annex 16. Growth rates of strontianite as a function of the surface of the seed crystals

Log S	SSA (m²·L^{-1})	R_G (10^{-9} mol·s^{-1})
1.3	1.7	1.2 ± 0.1
1.3	6.6	1.9 ± 0.1
1.3	9.9	2.0 ± 0.1
1.3	13.2	2.5 ± 0.1

[14] Rates not normalized to the surface area of the seed crystals. Homogeneous nucleation prevails at this supersaturation range. Therefore, the rate of crystal growth is not dependent on the specific surface of the seed crystals.

Annex 17. Growth rates of celestite as a function of the surface of the seed crystals. The temperature and the ionic strength are 298 K and 0.1 M, respectively.

Log S	SSA ($m^2 L^{-1}$)	R_G (10^{-9} mol·s-1)	Log S	SSA ($10^{-1} m^2 \cdot L^{-1}$)	R_G (10^{-8} mol·s-1)
0.6	0.00	2.3 ± 0.1	0.95	0.8	1.3 ± 0.2
0.6	0.4	3.9 ± 1.1	0.95	2.1	2.2 ± 0.2
0.6	0.7	5.5 ± 0.1	0.95	4.2	2.9 ± 0.2
0.6	1.2	7.6 ± 0.1	0.95	9.7	3.2 ± 0.2
0.6	1.7	9.1 ± 1.1			
0.6	2.5	11.2 ± 0.7			

Annex 18. Rate constants for the crystal growth of celestite and strontianite as a function of temperature. The given strontium concentrations are equals to the anions (sulfate, carbonate) concentrations. The ionic strength of the solutions is kept at 0.1 $mol \cdot l^{-1}$ using NaCl.

celestite			strontianite		
[Sr] 10^{-3} M	T [K]	k 10^{-8} $mol \cdot m^{-2} \cdot s^{-1}$	[Sr] 10^{-4} M	T [K]	k 10^{-10} $mol \cdot m^{-2} \cdot s^{-1}$
5.25	278	4.0 ± 0.2	5.65	278	3.0 ± 0.0
5.25	293	5.5 ± 0.2	5.65	293	6.7 ± 0.1
5.25	318	8.1 ± 0.3	5.65	318	21.2 ± 0.6
5.25	338	11.7 ± 0.3			

Annex 19. Influence of the ionic strength on the growth rates of celestite at constant supersaturation ratio S = 10. The solute concentrations corresponding the each ionic strength are given by $[Sr^{2+}] = [SO_4^{2-}]$

I [mol·kg^{-1}]	$Sr^{2+} = SO_4^{2-}$ [mM]	R_G [10^{-8} mol·s^{-1}]	Log k
0.1	5.8	2.62 ± 0.42	-8.54 ± 0.07
0.5	10.0	3.25 ± 0.03	-8.44 ± 0.01
1.0	15.0	5.35 ± 1.01	-8.23 ± 0.08
1.5	17.8	5.80 ± 0.39	-8.19 ± 0.03
2.0	21.8	7.67 ± 1.03	-8.07 ± 0.06

Annex 20. Fluorescence emission spectra for the $^7F_0$ transition of Eu(III) in strontianite

The supersaturation of the sample was S = 8.9 with respect to strontianite. The Eu(III) concentration was $1.25 \cdot 10^{-7}$ mol·l^{-1}. The spectra are recorded at 6 K with different delay time and with a grating of 2400 l/mm, allowing a better resolution. The two peaks in the $^7F_0$ correlate with the number of species in the sample. This is also supported by the bi-exponential decay of the fluorescence lifetime.

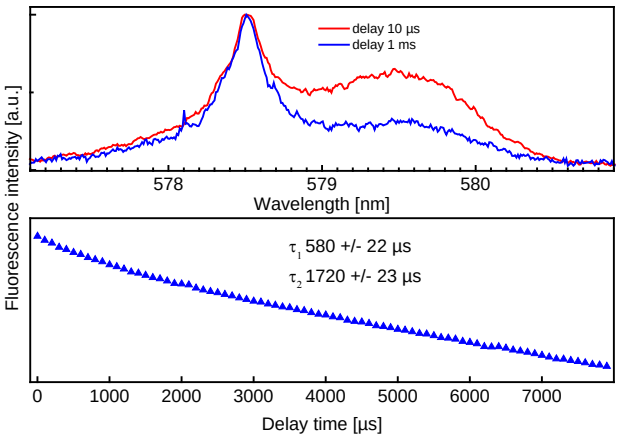

Annex 21: Emission spectra and lifetimes of Cm(III) during homogeneous nucleation of celestite at supersaturation S = 100

The induction time for the nucleation of celestite at supersaturation S = 100 is shorter than 1 min, since precipitation occurs spontaneously with the creation of supersaturation. The first fluorescence emission spectrum recorded at t = 5 min shows the incorporation of Cm(III) in celestite, as observed previously at S = 12.6. The quartz cuvette containing the sample was mistakenly not tightly closed, and CO_2 intrusion was observed after 48 h (peak at 610 nm). Spectra recorded after 5 min of reaction time with different delays clearly show the existence of several species with different fluorescence lifetimes. The latter was determined to be 80 ± 7 µs (mixture of Cm(III) aquo and mono-sulfato species) and 979 ± 50 µs (incorporated species). With the exception of the peak corresponding to the intrusion of carbon dioxide, there is no difference between the species formed at S = 12.6 and S = 100.

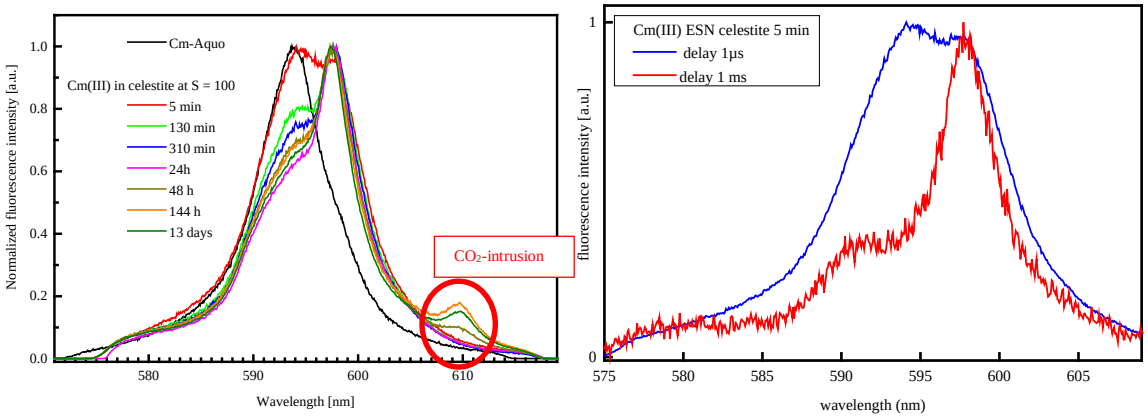

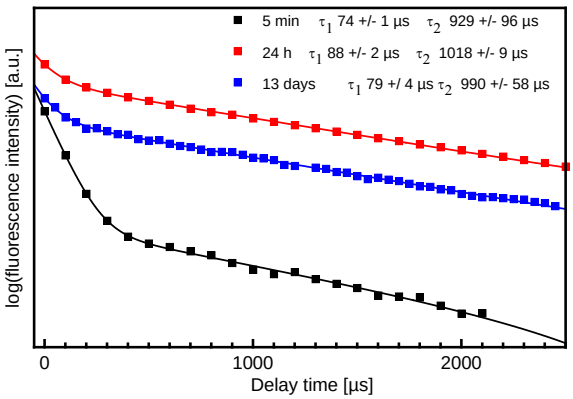

Annex 22: Emission spectra and lifetimes of Cm^{3+} during growth of strontianite in MFR experiments at supersaturation S = 1000. The spectrum in A) was recorded at 6 K and clearly shows the Cm(III) ground state splitting (Kramer-dubletts). C) The spectrum recorded at room temperature with different delays (1 µs and 250 µs) are identical, suggesting the existence of a single species, which lifetime was determined in B) to be 486 ± 5 µs.

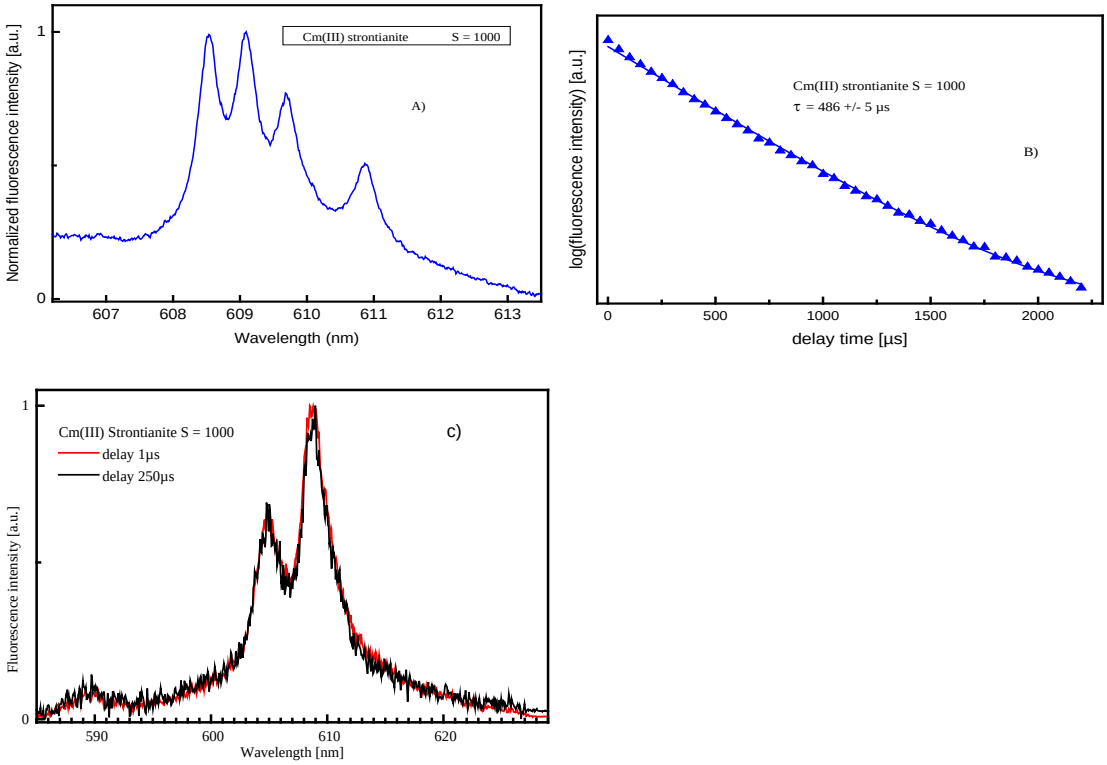

Annex 23. SEM of strontianite as a function of temperature: A) 278 K; B) 298 K; C) 318 K; D) 338. The initial solute concentration was $[Sr^{2+}] = [CO_3^{2-}]$ = 4.4 mM, corresponding to a supersaturation ratio S = 1000 at 298 K.

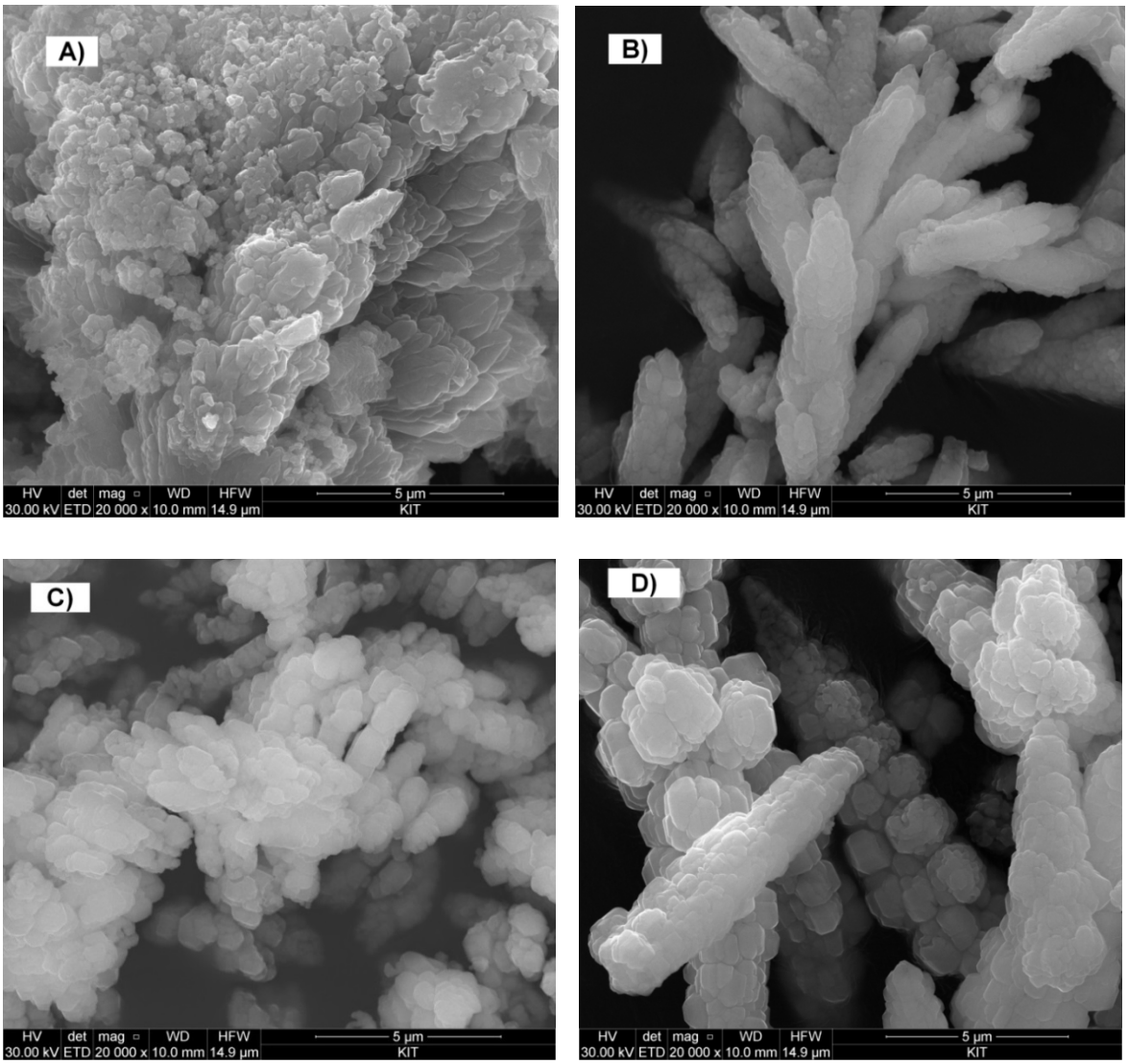

Annex 24. SEM of celestite precipitated at different temperatures: E) 278 K; F) 298 K; G) 318 K; H) 338. The initial solute concentration was $[Sr^{2+}] = [SO_4^{2-}] = 25.2$ mM, corresponding to a supersaturation ratio S = 100 at 298 K.